On the Numerical Solution of the Inverse Obstacle Scattering Problem

Marcos Aurelio Capistrán Ocampo

A dissertation submitted in partial fulfillment

of the requirements for the degree of

Doctor of Philosophy

Department of Mathematics

New York University

May 2003

Yu Chen

"With a little help from my friends", Lennon & McCartney.

Dedicated to my family

Acknowledgments

This work was partially supported under a grant from the National Council of Science and Technology (CONACyT) of Mexico. I would like to thank my advisor, Professor Yu Chen as well as Professor Leslie Greengard for making this work possible.

Abstract

The subject of this thesis is the numerical solution of the inverse obstacle scattering problem governed by the Helmholtz equation in two dimensions. The problem is to determine the shape of an obstacle from scattering measurements corresponding to time-harmonic plane incident waves. The inverse obstacle problem, as many other inverse problems, is nonlinear and ill-posed.

As it is well known, a nonlinear problem

$$F(\Gamma) = u,$$

can be effectively solved with an iterative method, such as Newton's method, provided that we start with a good initial guess. The highly nonlinear and oscillatory nature of the inverse scattering problem makes the initial guess extremely difficult to obtain.

In this work, we present a continuation method to reliably solve the inverse obstacle problem numerically without the need of a good initial guess.

The continuation method starts at the lowest wavenumber for which the scattering data is available, and at which the inverse problem is nearly linear. We first solve this nearly linear problem to obtain an approximate solution. Then, the continuation method recursively refines the approximate solution Γ

obtained at wavenumber k by solving the linearized equation

$$F'(\Gamma)\delta\Gamma = u - F(\Gamma),$$

at wavenumber $k + \delta k$. This upward march in wavenumber ends at the highest wavenumber at which the scattering measurement is available.

Our numerical experiments show that the scheme is stable and convergent for obstacles difficult to reconstruct: shapes with complex features and concavities. Various numerical and technical issues related to the implementation of the continuation method, such as regularization of ill-possedness and efficient frequency stepping have been systematically investigated and resolved in this work.

Contents

Chapter 1

Introduction

The inverse obstacle scattering problem treated in this work is to determine the shape of an scattering obstacle from measurements of the far field pattern corresponding to one or more time-harmonic acoustic waves incident upon the obstacle.

The development of methods for the numerical solution of inverse scattering problems started approximately 20 years ago, and although it currently is an area of intense activity, its mathematical theory is still being constructed. The classical problem treated here is important since the methods employed for its numerical solution can often be generalized to other inverse scattering problems.

The inverse problem is nonlinear and ill-posed. It is known that if a solution exists it is unique, but it does not depend continuously on the data in any reasonable norm, see for instance [5, 8] and [9]. For this reason, regularization is necessary for the numerical approximation of the solution. The Fréchet differentiability of the operator that models the corresponding direct problem provides the prerequisites for the development of iterative methods, such as Newton's method.

1.1 Existing Work on the Inverse Obstacle Scattering Problem

Among the most frequently studied inversion methods are schemes based on regularized Newton's iteration for the inverse obstacle problem in two dimensions; see for example Kirsch [20, 21], Kress [28, 29, 30], Kress and Rundell [31], Murch, Tan and Wall [36], Roger [39], Tobocman [43], and Wang and Chen [44]. Other closely related problems have been approached via a regularized Newton method, Monk [34] offers an implementation with a sound-hard obstacle, and in [35] addresses the problem where the scatterer is an open arc. Kress and Rundell [32] consider the problem of recovering both the shape and impedance of a two-dimensional obstacle. Researchers have worked on the analysis of convergence of regularized Newton methods; see [16, 17], Jin [19] and Potthast [38]. Apparently Newton-type methods represent a practical choice for the inverse scattering problem. Although further research is necessary to improve its efficiency.

Another class of iterative methods are derived from the Landweber iteration, for which the Fréchet derivative is approximated numerically. Implementations in 2D of the Landweber iteration have been given by Hanke, Hettlich and Scherzer [13] for sound-soft obstacles, and by Hettlich for sound-hard obstacles in [14] and the transmission problem in [15].

Kirsch and Kress introduced a numerical method to solve the inverse obstacle scattering problem called *Method of approximation of the scattered field* in the papers [23, 24, 25]. This method solves the inverse obstacle scattering problem in two stages: in the first part the far field is converted back to the scattered

field near the obstacle, the second part deals with the problem of locating the obstacle boundary as the zeroes of the total field, that is, of the sum of incident and scattered waves. Colton and Monk introduced a method of superposition of incident fields also called *Dual space method* in [10, 11, 12]. Similar to the method of approximation of the scattered field by Kirsch and Kress, the method of superposition of incident fields reconstructs the scattered field in a neighborhood of the obstacle in the first part, and determines to obstacle boundary as the zeroes of the total field in the second part.

One of the most popular methods, *the linear sampling method*, for inverse obstacle problem is introduced by Colton and Kirsch [7] in 1996. This method may be regarded as a modification of the dual space method. The following is a concise description of the method taken from [7]: *In the linear sampling method it is assumed that the far field pattern* $u_\infty(\varphi, \theta)$ *is known for all observation angles* φ *and plane waves with incident angle* θ *for all* $\varphi, \theta \in [-\pi, \pi]$. *From this information, the support of the obstacle is determined by solving the integral equation*

$$\int_{-\pi}^{\pi} u_\infty(\varphi, \theta) g(\theta) d\theta = e^{-ik\rho\cos(\varphi-\alpha)}, \quad \varphi \in [-\pi, \pi],$$

where k *is the wavenumber and* $y_0 = \rho(\cos\alpha, \sin\alpha)$ *is on a rectangular grid containing the scatterer. The support is found by noting that* $\|g\|_{L^2(pi,\pi)}$ *is unbounded as* y_0 *approached the boundary of the scattering obstacle from inside the scatterer.* An extensive description of the linear sampling method is presented in the book *Surveys of Solution Methods for Inverse Problems* by Colton et al [6].

There are recent reports with variants of the linear sampling method. Kirsch and Ritter [26] present a linear sampling method for inverse scattering from an

open arc. Cakoni, Colton and Monk [4] studied direct and inverse scattering problems for partially coated obstacles using the linear sampling method. Brandfass, Lanterman and Warnick [1] compare the linear sampling method with linearized tomographic inverse scattering algorithms. Tacchino, Coyle and Piana [42] offer a computational and numerical validation of the linear sampling method with four different regularization algorithms. Cakoni and Colton [3] give a mathematical justification of the linear sampling method.

One of the main drawbacks of the linear sampling method is its computational cost. Suppose n points are sufficient to discretize the obstacle boundary. To determine these points, we need $O(n)$ parameters from the far field data. In the linear sampling method $O(n^2)$ data parameters are used. At the same time, $O(n^2)$ points inside and outside the obstacle must be tested in the linear sampling method to determine the shape of the obstacle, with each test costing $O(n^2)$ flops in the back substitution for a linear system of equations. Clearly, the computational cost cannot be reduced below $O(n^4)$.

Santosa [40] proposed a level-set method for the numerical solution of inverse problems involving obstacles. Litman, Lesselier and Santosa [33] developed a method for the retrieval of the scattering obstacle in the inverse transmission problem. Burguer [2] proposed a level-set algorithm based on the method of asymptotic regularization.

In most methods described before the linear sampling and level-set methods, curves in the solution space are assumed to be star-shaped, that is, the presentation is restricted to cases of domains D such that its boundary ∂D can be represented in a parametric form

$$x = r(\hat{x})\hat{x}, \tag{1.1}$$

where $\hat{x}$ denotes a point in the unit circle Ω and $r \in C^1(\Omega)$ is a positive function, see [9].

1.2 Our Approach

In this work we introduce a method of continuation for the numerical solution to the inverse obstacle scattering problem. The inverse problem can be stated as a nonlinear operator equation

$$F(\Gamma; d; k) = u(d; k), \tag{1.2}$$

where Γ is the boundary of the scattering obstacle, d and k are the wavenumber and direction of the incident wave respectively, $u(d; k)$ is the scattering data. The continuation method starts at the lowest wavenumber for which the scattering data is available, and at which the inverse problem is nearly linear to obtain an approximate solution Γ_0. Then, the continuation method recursively refines the approximate solution Γ_i, obtained at wavenumber k_i, by solving the linearized equation

$$\frac{\partial F}{\partial \Gamma}(\Gamma_i; d; k_{i+1})\delta\Gamma_i = u(d; k_{i+1}) - F(\Gamma_i; d; k_{k+1}) \tag{1.3}$$

at wavenumber k_{i+1} and updating the approximate curve by $\Gamma_{i+1} = \Gamma_i + \delta\Gamma_i$. This upward march in wavenumber ends at the highest wavenumber at which the scattering measurement is available. In each iteration the relative residual of the far field pattern corresponding to approximate and exact solutions is required to become smaller than a tolerance value. If this condition is not satisfied the iteration is repeated with smaller wavenumber step-size.

There are various important technical issues related to the application of the continuation method to the inverse obstacle problem that had to be resolved in this work.

1. Ill-posedness. The linearized problem is well known to inherit the ill-posedness of the original, nonlinear problem, and thus requires regularization. An important question is whether a regularization procedure suitable for the linearized problem is also appropriate for the nonlinear problem which is successively approximated by these linearized problems.

2. Number of incident waves. For an obstacle whose boundary is not extremely convoluted, we may assume that the arclength of the boundary (in 2D) is comparable to circumference of the circumscribing circle. Therefore, we expect to recover the boundary with limited number of incident waves; as few as a single incident wave, because the number of parameters contained in a scattered wave is proportional to the arclength of that circle. For convoluted boundaries, such as those of concave obstacles, the above argument may fail. For a general obstacle, the number of incident waves and directions of these waves, sufficient for a stable inversion, need to be understood.

3. Concave obstacles. The inverse obstacle problem becomes more difficult as the boundary becomes more concave and convoluted. Very few methods succeed in reconstructing these complex shapes, partly due to the underlying physical process and partly due to numerical treatment. There seems to be no systematic, reliable inversion procedure for concave obstacles.

4. Frequency stepping. The step size in k depends strongly on the nature of

the obstacle. From the computational efficiency viewpoint, we desire to make the step size as large as possible, which conflicts with the convergence requirement. An automatic way to choose the step size to guarantee convergence and maximize efficiency is needed.

5. Tools building. One of the long existing impeding factors to the systematic study of the inverse obstacle problem is the lack of proper numerical tools. For example, to understand the behavior and difficulties involved in concave obstacles, one should have a convenient computer code to generate and process arbitrary simple closed curves.

The practicality of the continuation method is validated in this work numerically. The examples offered show that a broad class of smooth obstacles whose boundary is a simple closed curve can be retrieved with the use of the continuation method in a stable manner. To the knowledge of the author no previous research work on the solution of the inverse obstacle scattering problem reports the retrieval of non-convex obstacles with two significant digits. The technical issues mentioned above have been properly addressed.

Chapter 2

Background: Acoustic Scattering

In this chapter we summarize a few essential results of the mathematical description of acoustic scattering by an impenetrable obstacle. A more complete derivation and discussion on these results appear in [8, 9], and [22]. The direct acoustic scattering problem which determines the inverse problem treated in this work is specified in Section 2.1. Next, in Section 2.2 there is a brief discussion on the mapping defined, for a fixed incident wave, from the obstacle boundary into the *far field pattern* of the scattered wave. The inverse acoustic scattering problem treated in this work is specified in Section 2.3. Finally, the Nyström method for the numerical evaluation of integral operators with weakly singular kernels is included in Section 2.4.

2.1 The Direct Acoustic Scattering Problem

Let us consider the propagation of acoustic waves in a two dimensional homogeneous medium with speed of sound c. A linearized theory describes this wave motion in the most appropriate manner. There is a velocity potential

$U = U(x,t)$ from which the velocity field is obtained by

$$v = \operatorname{grad} U, \tag{2.1}$$

and the pressure p by

$$p - p_0 = -\frac{\partial U}{\partial t}, \tag{2.2}$$

where p_0 denotes the pressure in the undisturbed medium. The velocity potential satisfies the linear wave equation

$$\frac{\partial^2 U}{\partial t^2} = c^2 \Delta U. \tag{2.3}$$

For time-harmonic acoustic waves of the form $u(x,t) = u(x)\exp^{-i\omega t}$, with frequency $\omega > 0$, the space dependent part satisfies the Helmholtz equation

$$\Delta u + k^2 u = 0, \tag{2.4}$$

where the wavenumber is given by $k = \omega/c$. In this work setting, incident waves u^i are assumed to be plane waves of the form $u^i(x,t) = e^{i(kx\cdot d - \omega t)}$, or $u^i(x) = e^{ikx\cdot d}$, where d denotes an unit vector giving the direction of propagation of the wave. There is an obstacle D of compact support with boundary Γ. The direct scattering problem consists in determining the total field $u = u^i + u^s$ as a solution to the Helmholtz equation in the exterior domain $\mathbb{R}^2 - \bar{D}$ with boundary condition $u = 0$ on Γ, where u^s is the scattered wave (the pressure of the acoustic wave is prescribed on the obstacle boundary). In order to guarantee uniqueness of solutions the scattered wave is required to satisfy the *Sommerfeld radiation condition*

$$\lim_{r\to\infty} \sqrt{r}\left(\frac{\partial u^s}{\partial r} - iku^s\right) = 0, \quad r = \|x\|, \tag{2.5}$$

uniformly in all directions $\hat{x} = \frac{x}{\|x\|}$. This radiation condition also implies that solutions are outgoing waves. Solutions to the Helmholtz equation satisfying the radiation condition are referred to as radiating solutions. The direct scattering problem is

$$\begin{aligned}
\Delta u + k^2 u &= 0 \quad \text{in } \mathbb{R}^2 - \bar{D}, && (2.6)\\
u &= 0 \quad \text{on } \Gamma, && (2.7)\\
u(x) &= e^{ikx\cdot d} + u^s(x), && (2.8)\\
\lim_{r\to\infty} \sqrt{r}\left(\frac{\partial u^s}{\partial r} - iku^s\right) &= 0, \quad r = \|x\|. && (2.9)\\
& && (2.10)
\end{aligned}$$

For smooth boundaries, the well-posed nature of the direct problem can be proved in an elegant manner by reformulating the problem with an integral equation approach. See for instance, [8] or [9] for details on the following discussion:

For integrable functions φ the single-layer and double-layer acoustic potentials are defined as

$$u(x) = \int_\Gamma \Phi(x,y)\varphi(y)ds(y), \quad x \in \mathbb{R}^2 - \Gamma, \tag{2.11}$$

and

$$v(x) = \int_\Gamma \frac{\partial \Phi(x,y)}{\partial \nu(y)}\varphi(y)ds(y), \quad x \in \mathbb{R}^2 - \Gamma, \tag{2.12}$$

where $\Phi(x,y) = \frac{i}{4}H_0^{(1)}(k\|x-y\|),\ x \neq y$ is the fundamental solution of the Helmholtz equation (that is, the Hankel function of order zero of the first kind). Both $u(x)$ and $v(x)$ are radiating solutions of the Helmholtz equation. For continuous functions φ, the behavior of the acoustic potentials at the boundary is described by the following theorem, see [9]

Theorem 2.1.1 *Let Γ be of class C^2 and let φ be continuous. Then the single-layer potential u with density function φ is continuous throughout $\mathbb{R}^2$ and*

$$\|u\|_{\infty,\mathbb{R}^2} \leq C\|\varphi\|_{\infty,\Gamma} \tag{2.13}$$

for some constant C depending on Γ. On the boundary we have

$$u(x) = \int_\Gamma \Phi(y)\varphi(x,y)ds(y), \quad x \in \Gamma, \tag{2.14}$$

$$\frac{\partial u_\pm}{\partial \nu}(x) = \int_\Gamma \frac{\partial \Phi(x,y)}{\partial \nu(x)}\varphi(y)ds(y) \mp \frac{1}{2}\varphi(x), \quad x \in \Gamma, \tag{2.15}$$

where

$$\frac{\partial u_\pm}{\partial \nu}(x) = \lim_{h\to+0} \nu(x) \cdot \operatorname{grad} u(x \pm h\nu(x)) \tag{2.16}$$

is to be understood in the sense of uniform convergence on Γ and where the integrals exist as improper integrals. The double-layer potential v with density function φ can be continuously extended from D to $\bar{D}$ and from $\mathbb{R}^2 - \bar{D}$ to $\mathbb{R}^2 - D$ with limiting values

$$v_\pm(x) = \int_\Gamma \frac{\partial \Phi(x,y)}{\partial \nu(y)}\varphi(y)ds(y) \pm \frac{1}{2}\varphi(x), \quad x \in \Gamma, \tag{2.17}$$

where

$$v_{\pm} = \lim_{h \to +0} v(x \pm h\nu(x)) \tag{2.18}$$

and where the integral exists as an improper integral. Furthermore,

$$\|v\|_{\infty,\bar{D}} \leq C\|\varphi\|_{\infty,\Gamma}, \quad \|v\|_{\infty,\mathbb{R}^2-D} \leq C\|\varphi\|_{\infty,\Gamma}, \tag{2.19}$$

for some constant C depending on Γ and

$$\lim_{h \to +0} \left\{ \frac{\partial v}{\partial \nu}(x + h\nu(x)) - \frac{\partial v}{\partial \nu}(x - h\nu(x)) \right\} = 0, \quad x \in \Gamma, \tag{2.20}$$

uniformly on Γ.

Definition 2.1.1 *For $x \in \Gamma$ we define the linear operators S, K and K' as:*

$$S(\varphi)(x) = 2\int_{\Gamma} \Phi(x,y)\varphi(y)ds(y), \tag{2.21}$$

$$K(\varphi)(x) = 2\int_{\Gamma} \frac{\partial \Phi(x,y)}{\partial \nu(y)}\varphi(y)ds(y), \tag{2.22}$$

$$K'(\varphi)(x) = 2\int_{\Gamma} \frac{\partial \Phi(x,y)}{\partial \nu(x)}\varphi(y)ds(y), \tag{2.23}$$

From the limit values of the acoustic potentials at Γ it follows that a combined potential of the form

$$u^s(x) = \frac{1}{2}(K(\varphi)(x) - ikS(\varphi)(x)), \quad x \in \mathbb{R}^2 - \Gamma, \tag{2.24}$$

solves the exterior Dirichlet problem provided that the density function φ is a solution of the integral equation

$$\varphi - K\varphi - ikS\varphi = -2u^i \quad \text{on } \Gamma. \tag{2.25}$$

It is known that Operators S and K are compact, and using Riesz-Fredholm theory it is readily established that $I + K - ikS : C(\Gamma) \to C(\Gamma)$ is bijective and the inverse $(I + K - ikS)^{-1} : C(\Gamma) \to C(\Gamma)$ is bounded. The first part implies that a solution to the direct problem exists and is unique; the second implies that a solution depends continuously on the boundary data in the maximum norm.

2.2 The Far Field Mapping

With the use of the Sommerfeld radiating condition, it is possible to extend the Green's representation formula for radiating solutions $u^s(x)$ of the Helmholtz equation in the exterior of D

$$u^s(x) = \int_\Gamma \left\{ u^s(y) \frac{\partial \Phi(x,y)}{\partial \nu(y)} - \frac{\partial u^s(y)}{\partial \nu} \Phi(x,y) \right\} ds(y), \quad x \in \mathbb{R}^2 - \bar{D}. \tag{2.26}$$

From equation (2.26), the asymptotic of the Hankel function

$$H_n^{(1)}(z) = \sqrt{\frac{2}{\pi z}} e^{i(z - n\pi/2 - \pi/4)} \left\{ 1 + O\left(\frac{1}{z}\right) \right\}, \quad z \to \infty, \tag{2.27}$$

and the expansion

$$\|x - y\| = \sqrt{\|x\|^2 - 2x \cdot y + \|y\|^2} = \|x\| - \hat{x} \cdot y + O\left(\frac{1}{\|x\|}\right), \tag{2.28}$$

it is derived that a radiating solution u^s to the Helmholtz equation has an asymptotic behavior of the form

$$u^s(x) = \frac{e^{ik\|x\|}}{\sqrt{\|x\|}} \left\{ u_\infty(\hat{x}) + O\left(\frac{1}{\|x\|}\right) \right\}, \quad \|x\| \to \infty, \tag{2.29}$$

uniformly in all directions $\hat{x} = \frac{x}{\|x\|}$. The function $u_\infty(\hat{x})$, defined on the unit circle, is referred to as the *far field pattern* of the radiating solution $u^s(x)$. For a fixed incident wave u^i, the mapping from the boundary of the scattering obstacle into the far field pattern

$$F(\Gamma) = u_\infty(\hat{x}), \tag{2.30}$$

is called the *far field mapping*. Let us denote the unit circle by Ω. The far field mapping is known to be continuous and Fréchet differentiable from $C^1(\Omega)$ into $L^2(\Omega)$.

We like to mention the following result from Chapter 2 of [18]

Definition 2.2.1 *Let $J : X \to Y$ be a linear operator defined between to normed spaces X and Y. $J(y)$ is Fréchet differentiable at y_0, if there exists a continuous linear functional $DJ(y_0)$ such that*

$$J(y + h) = J(y_0) + DJ(y_0)h + o(\|h\|), \tag{2.31}$$

for all h in the normed space X.

Definition 2.2.1 is used in Section 3.1 to describe the continuation method to approximately solve the inverse obstacle scattering problem.

2.3 The Inverse Acoustic Scattering Problem

Given the far field pattern u_∞ corresponding to one or more incoming plane waves u^i, the inverse scattering problem is to determine the shape of the scattering obstacle. This inverse problem is difficult because it is both nonlinear and ill-posed. The obstacle boundary can be described by a function in C^0 whereas

the far field pattern is an analytic function of the direction angle. Thus, a solution of equation (2.30) does not necessarily exist for prescribed data u_∞. Furthermore, if a solution exists, it usually does not depend continuously on u_∞. In the practice of numerically solving this inverse problem, ill-posedness will give rise to instability and non-uniqueness, and nonlinearity will give rise to local solutions when equation (2.30) is tackled via standard nonlinear solvers such as the gradient method, Newton's method, and the like.

The continuity and differentiability of the far field mapping operator F provide the prerequisites to solve the inverse problem equation (2.30) iteratively. On the other hand, the ill-posed nature of the equation affects its numerical treatment. It is necessary to use a method that allows to approximate the solution in a stable manner, or a *regularized method*. We discuss our approach to regularization in the next chapter.

2.4 The Nyström Method for Boundary Integral Equations

Nyström is the most practical method for the numerical solution of integral equations of the second kind in the one dimensional case, since only one evaluation of the kernel function is required in the evaluation of each of the matrix elements of the linear system. Also, Nyström method is stable in the sense that it preserves the condition number of the discretized integral equation, see [27].

To implement the Nyström Method for the solution of the obstacle scattering problem, we begin with 2π-periodic parametric representation of the boundary

curve of the form

$$x(t) = (x_1(t), x_2(t)), \quad 0 \le t \le 2\pi \tag{2.32}$$

counterclockwise oriented and satisfying $\|x'(t)\| > 0$ for all t. Then $S(\varphi)(x)$, $K(\varphi)(x)$, $K'(\varphi)(x)$ can be written in the following form

$$\begin{aligned} S(\varphi)(x) &= \int_0^{2\pi} M(t,\tau)\varphi(\tau)d\tau, & (2.33)\\ K(\varphi)(x) &= \int_0^{2\pi} L(t,\tau)\varphi(\tau)d\tau, & (2.34)\\ K'(\varphi)(x) &= \int_0^{2\pi} L'(t,\tau)\varphi(\tau)d\tau, & (2.35) \end{aligned}$$

where we have set $\varphi(t) = \varphi(x(t))$ and the kernels are given by

$$\begin{aligned} M(t,\tau) &= \frac{i}{2}H_0^{(1)}(k\|x(t)-x(\tau)\|)\|x'(\tau)\|,\\ L(t,\tau) &= \frac{ik}{2}((x'(\tau))^{\perp}\cdot(x(\tau)-x(t))\frac{H_1^{(1)}(k\|x(t)-x(\tau)\|)}{\|x(t)-x(\tau)\|},\\ L'(t,\tau) &= -\frac{ik}{2}((x'(t))^{\perp}\cdot(x(\tau)-x(t))\frac{H_1^{(1)}(k\|x(t)-x(\tau)\|)}{\|x(t)-x(\tau)\|}\frac{\|x'(\tau)\|}{\|x'(t)\|}, \end{aligned}$$

where $(x'(t))^{\perp} = (-x_2'(t), x_1'(t))$. The kernels M, L and L' have logarithmic singularities. For their numerical treatment they are split into

$$\begin{aligned} M(t,\tau) &= M_1(t,\tau)\ln(4\sin^2\frac{t-\tau}{2}) + M_2(t,\tau)\\ L(t,\tau) &= L_1(t,\tau)\ln(4\sin^2\frac{t-\tau}{2}) + L_2(t,\tau)\\ L'(t,\tau) &= L_1'(t,\tau)\ln(4\sin^2\frac{t-\tau}{2}) + L_2'(t,\tau) \end{aligned}$$

where

$$
\begin{aligned}
M_1(t,\tau) &= -\frac{1}{2\pi} J_0(k\|x(t)-x(\tau)\|)\|x'(\tau)\|, \\
M_2(t,\tau) &= M(t,\tau) - \ln(4\sin^2\frac{t-\tau}{2}) M_1(t,\tau), \\
L_1(t,\tau) &= \frac{k}{2\pi}((x'(\tau))^{\perp}\cdot(x(t)-x(\tau))\frac{J_1(k\|x(t)-x(\tau)\|)}{\|x(t)-x(\tau)\|}, \\
L_2(t,\tau) &= L(t,\tau) - \ln(4\sin^2\frac{t-\tau}{2}) L_1(t,\tau), \\
L_1'(t,\tau) &= -\frac{k}{2\pi}((x'(t))^{\perp}\cdot(x(t)-x(\tau))\frac{J_1(k\|x(t)-x(\tau)\|)}{\|x(t)-x(\tau)\|}\frac{\|x'(\tau)\|}{\|x'(t)\|}, \\
L_2'(t,\tau) &= L'(t,\tau) - \ln(4\sin^2\frac{t-\tau}{2}) L_1'(t,\tau).
\end{aligned}
$$

The kernels $M_1,\ M_2,\ L_1,\ L_2,\ L_1'$ and L_2' are analytic. The diagonal terms are given by

$$
M_2(t,t) = \left\{\frac{i}{2} - \frac{\gamma}{\pi} - \frac{1}{2\pi}\ln(\frac{k^2}{4}\|x'(t)\|^2)\right\}\|x'(t)\|, \tag{2.36}
$$

$$
L_2(t,t) = \frac{1}{2\pi}\frac{x'(t)\cdot x''(t)}{\|x'(t)\|^2}, \tag{2.37}
$$

$$
L_2'(t,t) = L_2(t,t). \tag{2.38}
$$

The Nyström method consists of the straightforward approximation of the integrals by quadrature formulas

$$
\int_0^{2\pi} \ln(4\sin^2\frac{t-\tau}{2}) f(\tau)d\tau \approx \sum_{j=0}^{2n-1} R_j^{(n)}(t) f(t_j), \quad 0 \le t \le 2\pi \tag{2.39}
$$

at the set of equidistant knots $t_j = \pi j/n,\ j = 0, ..., 2n-1$; with the quadrature weights given by

$$
R_j^{(n)}(t) = -\frac{2\pi}{n}\sum_{m=1}^{n-1}\frac{1}{m}\cos(m(t-t_j)) - \frac{\pi}{n^2}\cos(n(t-t_j)), \quad j = 0, ..., 2n-1, \tag{2.40}
$$

and the trapezoidal rule

$$
\int_0^{2\pi} f(\tau)d\tau = \frac{\pi}{n}\sum_{j=0}^{2n-1} f(t_j) \tag{2.41}
$$

It is essential to split the logarithmic singularities in a way that the kernels $M_1, L_1, L_1', M_2, L_2, L_2'$ preserve their 2π-periodicity.

Chapter 3

Method of Continuation in the k-Space

In this chapter the continuation method and its implementation are explained. A description of the method is presented in section 3.1. In section 3.2, a representation of the domain derivative of the far field mapping $\partial F/\partial\Gamma$ in terms of the operators S, K and K' is given in equations (3.14) and (3.31); this so-called domain derivative is the core step of the perturbational calculation. The corresponding representation of $\partial F/\partial\Gamma$, using a combined potential approach, is given in the appendix. In section 3.3 is the discretization of $\partial F/\partial\Gamma$ using the Nyström method. A simple approach to regularization is offered in section 3.4, with an approximate solution to a linear system via a pseudo-inverse of a matrix with large condition number, based on its singular value decomposition.

3.1 The Continuation Method

Let us consider the far field mapping equation for a plane wave $u^i = e^{ikx\cdot d}$ with wavenumber k and incident direction d; the mapping goes from the obstacle boundary Γ into the far field pattern of the scattered wave $u_\infty(\hat{x}; d; k)$

$$F(\Gamma; d; k) = u_\infty(\hat{x}; d; k). \tag{3.1}$$

If we perturb the boundary curve Γ, represented as x, along its normal direction $\nu(x)$ by an small amount $\delta\nu(x)$ to a boundary curve $\tilde{\Gamma}$, represented as $\tilde{x} = x + \delta\nu(x)\nu(x)$, it is possible to linearize equation 3.1 around the boundary curve $\tilde{\Gamma}$ with the use of the domain derivative $\partial F/\partial\Gamma(\tilde{\Gamma}, k)$ to obtain, to the second order of $\|\delta\nu\|^2$,

$$\frac{\partial F}{\partial \Gamma}(\tilde{\Gamma}; d; k)\delta\nu = u_\infty(\hat{x}; d; k) - F(\hat{\Gamma}; d; k). \tag{3.2}$$

Assuming that scattering data is available for each wavenumber k_j, with $k_0 = \delta k_0 < k_1 = k_0 + \delta k_1 < ... < k_q = k_{q-1} + \delta k_q$, the method of continuation starts at the lowest wavenumber k_0 for which the data is available, and for which the problem is nearly linear. In this first step we determine three real or two complex parameters, obtaining an approximate solution curve Γ_0, represented as x_0 (a circle or an ellipse). This is accomplished by an optimization process. Then, an approximate solution curve Γ_j, obtained with wavenumber k_j, is recursively refined by solving the linearized equation 3.2 at wavenumber k_{j+1}, and updating the approximate solution curve Γ_j, represented as x_j, to Γ_{j+1}, represented as $x_{j+1} = x_j + \delta\nu(x_j)\nu(x_j)$.

The following is a summary of one step of the continuation method:

- For given approximate boundary curve x_j and incident field $u^i(d; k_{j+1})$, calculate the far field mapping domain derivative at a set of equidistant observation points $\hat{x}_l$,

- Solve the linearized equation (3.2) to find $\delta\nu(x_j)$, using far field pattern data produced by the target obstacle boundary Γ and incident field $u^i(d; k_{j+1})$,

- Update the approximate boundary curve $x_{j+1} = x_j + \delta\nu(x_j)\nu(x_j)$,

- Calculate the far filed pattern relative error

$$Err = \|u_\infty(d; k_{j+1}) - F(d; k_{j+1}; \Gamma_{j+1})\| / \|u_\infty(d; k_{j+1})\|, \qquad (3.3)$$

- If Err is acceptable increase wavenumber to $k_{i+2} = k_{i+1} + \delta k$, else set wavenumber equal to $k_{i+2} = k_{i+1} + \delta k/2$.

Since the curve update $\delta\nu_j$ from all incident plane waves $u^i(d; k_{j+1})$ should be consistent, it is possible to use two or more incident plane waves u^i_1, u^i_2, ..., u^i_l, with incident directions d_1, d_2, ..., d_l, to obtain the curve update. For this purpose the linear systems are stacked in the following way

$$\begin{bmatrix} \frac{\partial F}{\partial \Gamma}(d_1; k_{j+1}; \Gamma_j) \\ \frac{\partial F}{\partial \Gamma}(d_2; k_{j+1}; \Gamma_j) \\ \vdots \\ \frac{\partial F}{\partial \Gamma}(d_l; k_{j+1}; \Gamma_j) \end{bmatrix} \delta\nu = \begin{bmatrix} u_\infty(d_1; k_{j+1}) - F(d_1; k_{j+1}; \Gamma_j) \\ u_\infty(d_2; k_{j+1}) - F(d_2; k_{j+1}; \Gamma_j) \\ \vdots \\ u_\infty(d_l; k_{j+1}) - F(d_l; k_{j+1}; \Gamma_j) \end{bmatrix},$$

where $\partial F/\partial\Gamma(d_q; k_{j+1}; \Gamma_j)$ is the domain derivative of the far field mapping at the boundary curve Γ_j for an incident wave with wavenumber k_{j+1} and direction

d_q; $u_\infty(d_q; k_{j+1})$ and $F(d_q; k_{j+1}; \Gamma_j)$ are the far field pattern data and the far field mapping evaluated at Γ_j respectively.

In the method of continuation, the natural choice for the data space is the Hilbert space of square integrable functions on the unit sphere $L^2(\Omega)$. It remains an open problem to characterize the class of boundary curves that can be retrieved solving the inverse obstacle scattering problem. In our numerical experiments obstacle boundaries are simple closed curves of class $C^2(\Omega)$.

3.2 The Domain Derivative of the Far Field Mapping

Since $S(\psi)(x)$ is continuous in $\mathbb{R}^2$, $u^s(x) = \frac{1}{2}S(\psi)(x)$ is a solution of the exterior Dirichlet problem if

$$S(\psi)(x) = -2e^{ikx\cdot d}, \quad x \in \Gamma, \tag{3.4}$$

or

$$\int_\Gamma \Phi(x,y)\varphi(y)ds(y) = -e^{ikx\cdot d}, \quad x \in \Gamma. \tag{3.5}$$

Using the asymptotic (2.27) and the expansion (2.28) we find that the far field mapping can be written as

$$u_\infty(\hat{x}) = S_\infty(\varphi)(\hat{x}) = \frac{e^{ik\pi}}{\sqrt{8\pi k}} \int_\Gamma e^{-ik\hat{x}\cdot y}\varphi(y)ds(y). \tag{3.6}$$

Let $x = x(s)$ be a parameterization with respect to arc-length $s \in [0, L]$ of the smooth simple closed curve Γ in $\mathbb{R}^2$. Let $\tau(x)$ and $\nu(x)$ be its tangent and

outward normal vectors at the point $x(s)$ respectively. Perturbing Γ at each point $x \in \Gamma$ by an amount $\delta\nu(x)$ in the normal direction gives

$$\tilde{\Gamma} = \{\tilde{x} \in \mathbb{R}^2 \mid \tilde{x} = x + \delta\nu(x)\nu(x), \quad x \in \Gamma\}. \tag{3.7}$$

Suppose further that $\tilde{\Gamma}$ is a smooth simple closed curve in $\mathbb{R}^2$ parameterized by its arc-length $\tilde{s} \in [0, \tilde{L}]$; consequently, there is a mapping $\eta : \Gamma \to \tilde{\Gamma}$ defined by the formula

$$\eta(x) = \tilde{x} + \delta\nu(x)\nu(x). \tag{3.8}$$

For an element ds on Γ with endpoints $x(s)$ and $x(s+\delta s)$, the corresponding element $d\tilde{s}$ in $\tilde{\Gamma}$ is defined as the element with endpoints $\eta(x(s))$ and $\eta(x(s+\delta s))$.

Lemma 3.2.1 *Suppose Γ and $\tilde{\Gamma}$ are two smooth simple closed curves, and $\kappa(x)$ is the curvature of Γ at $x(s)$ defined by $\kappa(x) = \nu(x(s))^{\perp} \cdot \tau(x(s))$. Suppose further that $\tilde{\Gamma}$ is close to and nearly parallel to Γ; namely*

$$\kappa(x)\delta\nu(x) \ll 1, \quad \frac{d(\delta\nu)}{ds}(x) \ll 1, \tag{3.9}$$

then, to the second order of $\kappa(x)\delta\nu(x)$, $\delta\nu'(x)$

$$d\tilde{s} = (1 + \kappa(x)\delta\nu(x))ds \tag{3.10}$$

Now, let us assume that each point $x(s)$ on the boundary Γ is perturbed along the normal direction to the point $\tilde{x} = \eta(x)$. Assume further that the perturbation is small enough to satisfy the conditions from equation (3.9), and denote by $\tilde{\varphi}$ the solution to the integral equation on $\tilde{\Gamma}$

$$\int_{\tilde{\Gamma}} \Phi(\tilde{x},\tilde{y})\tilde{\varphi}(\tilde{y})d\tilde{s}(\tilde{y}) = -e^{ik\tilde{x}\cdot d}. \tag{3.11}$$

Lemma 3.2.2 *Suppose under the conditions of lemma (3.2.1) that for* $x \in \Gamma$

$$\delta(x) = \max\{\mid \kappa(x)\delta\nu(x) \mid, \mid \frac{d(\delta\nu)}{ds}(x)\mid\} \tag{3.12}$$

then

$$\delta\varphi(x) = \tilde{\varphi}(\tilde{x}) - \varphi(x) \tag{3.13}$$

is of the order $\delta(x)$*. Furthermore, to the second order of* $\delta(x)$*,* $\delta\varphi(x)$ *satisfies the equation*

$$S(\delta\varphi+\kappa\delta\nu\varphi)(x)+K(\delta\nu\varphi)(x)+\delta\nu(x)K'(\varphi)(x) = -2ik\nu(x)\cdot de^{ikx\cdot d}\delta\nu(x) \tag{3.14}$$

Proof

For points $x,\ y \in \Gamma$, $\tilde{x} = \eta(x)$ and $\tilde{y} = \eta(y)$ denote the corresponding points on $\tilde{\Gamma}$. To the second order of $\delta(x)$, $S(\tilde{\varphi})(\tilde{x})$ can be rewritten as

$$\begin{aligned} S(\tilde{\varphi})(\tilde{x}) &= \int_{\tilde{\Gamma}} \Phi(\tilde{x},\tilde{y})\tilde{\varphi}(\tilde{y})d\tilde{s}(\tilde{y}) && (3.15)\\ &= \int_{\Gamma} \Phi(\eta(x),\eta(y))[\varphi(y)+\delta\varphi(y)][1+\kappa(y)\delta\nu(y)]ds(y) && (3.16) \end{aligned}$$

Subtracting $S(\varphi)(x)$ from $S(\tilde{\varphi})(\tilde{x})$ leads to

$$
\begin{aligned}
& S(\tilde{\varphi})(\tilde{x}) - S(\varphi)(x) \\
= & \int_\Gamma \Phi(\eta(x),\eta(y))[\varphi(y)+\delta\varphi(y)+\kappa(y)\delta\nu(y)\varphi(y)]ds(y) - \\
& \int_\Gamma \Phi(x,y)\varphi(y)ds(y) \qquad (3.17)\\
= & \int_\Gamma \Phi(\eta(x),\eta(y))[\delta\varphi(y)+\kappa(y)\delta\nu(y)\varphi(y)]ds(y) + \\
& \int_\Gamma [\Phi(\eta(x),\eta(y)) - \Phi(x,y)]\varphi(y)ds(y) \qquad (3.18)\\
= & I_1 + I_2. \qquad (3.19)
\end{aligned}
$$

Here, given that $\Phi(\eta(x),\eta(y)) = \Phi(x,y) + O(|\delta\nu|)$, it follows that I_1 can be written to the second order of $\delta(x)$ as

$$
\begin{aligned}
I_1 &= \int_\Gamma \Phi(x,y)[\delta\varphi(y)+\kappa(y)\delta\nu(y)\varphi(y)+]ds(y) \qquad (3.20)\\
&= \frac{1}{2}S(\delta\varphi+\kappa\delta\nu\varphi)(x). \qquad (3.21)
\end{aligned}
$$

On the other hand,

$$
\begin{aligned}
I_2 &= \int_\Gamma [\Phi(\eta(x),\eta(y)) - \Phi(x,y)]\varphi(y)ds(y) \qquad (3.22)\\
&= \int_\Gamma [\Phi(\eta(x),\eta(y)) - \Phi(\eta(x),y)]\varphi(y)ds(y) + \\
& \quad \int_\Gamma [\Phi(\eta(x),y) - \Phi(x,y)]\varphi(y)ds(y) \qquad (3.23)\\
&= J_1 + J_2. \qquad (3.24)
\end{aligned}
$$

Using theorem (2.1.1), it follows that to the second order of $\delta(x)$

$$J_1 = \int_\Gamma [\Phi(\eta(x), \eta(y)) - \Phi(\eta(x), y)]\varphi(y) ds(y) \tag{3.25}$$

$$= \frac{1}{2}(K - I)(\delta\nu\varphi)(x), \tag{3.26}$$

and

$$J_2 = \int_\Gamma [\Phi(\eta(x), y) - \Phi(x, y)]\varphi(y) ds(y) \tag{3.27}$$

$$= \frac{1}{2}\delta\nu(x)(K' + I)(\varphi)(x). \tag{3.28}$$

The lemma follows immediately. ■

The same perturbation analysis can be applied to the far field pattern. Let $\tilde{u}_\infty(\hat{x})$ be the far field pattern generated by the density function $\tilde{\varphi}$ on $\tilde{\Gamma}$ so that

$$\tilde{u}_\infty(\hat{x}) = \int_{\tilde{\Gamma}} \Phi_\infty(\hat{x}, \tilde{y})\tilde{\varphi}(\tilde{y}) d\tilde{s}(\tilde{y}), \tag{3.29}$$

where $\Phi_\infty(\hat{x}, \tilde{y}) = \frac{e^{ik\pi}}{\sqrt{8\pi k}} e^{-ik\hat{x}\cdot y}$.

Lemma 3.2.3 *Under the conditions of lemma (3.2.1), suppose the density functions $\varphi \in C(\Gamma)$ and $\tilde{\varphi} \in C(\tilde{\Gamma})$ are solutions of the integral equations (3.5) and (3.11) respectively. Suppose further that u_∞, $\tilde{u}_\infty \in C^\infty(\Omega)$, are the corresponding far field patterns. Then*

$$\delta u_\infty(\hat{x}) = \tilde{u}_\infty(\hat{x}) - u_\infty(\hat{x}) \tag{3.30}$$

is of the order $\delta(x)$, and to the second order of $\delta(x)$

$$\delta u_\infty(\hat{x}) = S_\infty(-ik\hat{x} \cdot \nu\delta\nu\varphi + \delta\varphi + \kappa\delta\nu\varphi)(\hat{x}). \tag{3.31}$$

Proof

For points x, $y \in \Gamma$, $\tilde{x} = \eta(x)$ and $\tilde{y} = \eta(y)$ denote the corresponding points in $\tilde{\Gamma}$ as before. Now, to the second order of δ, $u_\infty(\hat{x})$ can be written as

$$\begin{aligned} \tilde{u}_\infty(\hat{x}) &= \int_{\tilde{\Gamma}} \Phi_\infty(\hat{x}, \tilde{y})\tilde{\varphi}(\tilde{y})d\tilde{s}(\tilde{y}) && (3.32) \\ &= \int_{\Gamma} \Phi_\infty(\hat{x}, \eta(y))[\varphi(y) + \delta\varphi(y)][1 + \kappa(y)\delta\nu(y)]ds(y) && (3.33) \end{aligned}$$

subtracting $u_\infty(\hat{x})$ from $\tilde{u}_\infty(\hat{x})$ leads to

$$\begin{aligned} \tilde{u}_\infty(\hat{x}) - u_\infty(\hat{x}) &= \int_{\Gamma} \Phi_\infty(\hat{x}, \eta(x))[\varphi(y) + \delta\varphi(y) + \kappa(y)\delta\nu(y)\varphi(y)]ds(y) - \\ &\quad \int_{\Gamma} \Phi_\infty(\hat{x}, y)\varphi(y)ds(y) && (3.34) \\ &= \int_{\Gamma} \Phi_\infty(\hat{x}, \eta(y))[\delta\varphi(y) + \kappa(y)\delta\nu(y)\varphi(y)]ds(y) - \\ &\quad \int_{\Gamma} [\Phi_\infty(\hat{x}, \eta(y)) - \Phi_\infty(\hat{x}, y)]\varphi(y)ds(y) && (3.35) \\ &= L_1 + L_2. && (3.36) \end{aligned}$$

Here, given that $\Phi_\infty(\hat{x}, \eta(y)) = \Phi_\infty(\hat{x}, y) + O(|\delta\nu|)$, L_1 can be written to the second order of $\delta(x)$ as

$$\begin{aligned} L_1 &= \int_{\Gamma} \Phi_\infty(\hat{x}, y)[\delta\varphi(y) + \kappa(y)\delta\nu(y)\varphi(y)]ds(y) && (3.37) \\ &= S_\infty(\delta\varphi + \kappa\delta\nu\varphi)(\hat{x}) && (3.38) \end{aligned}$$

Similarly, using example 3.3 from [18]

$$L_2 = \int_\Gamma [\Phi_\infty(\hat{x}, \eta(y)) - \Phi_\infty(\hat{x}, y)]\varphi(y)ds(y) \tag{3.39}$$

$$= \int_\Gamma -ik\hat{x} \cdot \nu(y)\delta\nu(y)\Phi_\infty(\hat{x}, y)\varphi(y)ds(y) \tag{3.40}$$

$$= S_\infty(-ik\hat{x} \cdot \nu\delta\nu\varphi)(\hat{x}). \tag{3.41}$$

3.3 Discretization of the Far Field Mapping Domain Derivative

To evaluate $F'(\Gamma)$ it is necessary to solve the integral equations of the first kind (3.14) and (3.31). First, equation (3.14) is solved in terms of $\delta\varphi(x) + \kappa(x)\delta\nu(x)$, and substituted into equation (3.31).

Suppose the boundary curve is parameterized by $x(t) : [0, 2\pi] \to \Gamma$, and consider curve grid points $x(t_j)$ or x_j with $t_j = \pi j/n$ for $j = 0, ..., 2n-1$. Then Nyström method can be used to approximate the left hand side of equation (3.14) in the following manner

$$S(\partial\varphi + \kappa\delta\nu\varphi)(x) \approx \sum_{j=0}^{2n-1} [M_1(t_i, t_j)R^{(n)}_{|i-j|} + \frac{\pi}{n}M_2(t_i, t_j)][\delta\varphi_j + \kappa_j\delta\nu_j\varphi_j],$$

where $M_1(x(t_i), x(t_j)) = M_1(t_i, t_j)$, $M_2(x(t_i), x(t_j)) = M_2(t_i, t_j)$, $\delta\varphi(x(t_j)) = \delta\varphi_j$, $\kappa(x(t_j)) = \kappa_j$, $\delta\nu(x(t_j)) = \delta\nu_j$, $\varphi(x(t_j)) = \varphi_j$. Thus

$$S(\delta\varphi + \kappa\delta\nu\varphi)(x) \approx S_{ij}[\delta\varphi_j + \kappa_j\delta\nu_j\varphi_j], \tag{3.42}$$

where S_{ij} is a $2n$ by $2n$ matrix, and $\delta\varphi_j$, $\kappa_j\delta\nu_j\varphi_j$ are two $2n$ by 1 arrays. Similarly,

$$K(\delta\nu\varphi)(x) \approx \sum_{j=0}^{2n-1}[L_1(t_i,t_j)R^{(n)}_{|i-j|} + \frac{\pi}{n}L_2(t_i,t_j)]\delta\nu_j\varphi_j, \tag{3.43}$$

$$\approx A_{ij}\delta\nu_j, \tag{3.44}$$

where A_{ij} is a $2n$ by $2n$ matrix, and $\delta\nu_j$, is a $2n$ by 1 array.

$$\delta\nu(x)K^{'}(\varphi)(x) \approx \delta\nu_i \sum_{j=0}^{2n-1}[L_1(t_i,t_j)R^{(n)}_{|i-j|} + \frac{\pi}{n}L_2(t_i,t_j)]\varphi_j. \tag{3.45}$$

The contribution from this term to the linear system is a product of the form $B_{ij}\delta\nu_j$ where B_{ij} is a $2n$ by $2n$ diagonal matrix with diagonal terms

$$B_{ii} = \sum_{j=0}^{2n-1}[L_1(t_i,t_j)R^{(n)}_{|i-j|} + \frac{\pi}{n}L_2(t_i,t_j)]\varphi_j. \tag{3.46}$$

Finally,

$$-2ik\nu(x)\cdot de^{ikx\cdot d}\delta\nu(x) \approx -2ik\nu_i\cdot de^{ikx_i\cdot d}\delta\nu_i, \tag{3.47}$$

also contributes to the linear system with the product of a diagonal matrix C_{ij} and $\delta\nu_j$. The integral equation (3.14) is approximated by

$$S_{ij}(\delta\varphi_j + \kappa_j\delta\nu_j\varphi_j) = (A_{ij} + B_{ij} + C_{ij})\delta\nu_j. \tag{3.48}$$

Similarly, let $\theta_l = \frac{l\pi}{m}$ for $l = 0, ..., 2m-1$, and let $\hat{x}_l = (\cos\theta_l, \sin\theta_l)$ be $2m$ observation points for the far field pattern. Then the left hand side of equation (3.31) is approximated term-wise in the following manner, first

$$S_\infty(-ik\hat{x}_l\cdot\nu\delta\nu\varphi)(\hat{x}_l) = \frac{e^{ik\pi}}{\sqrt{8\pi k}}\int_0^{2\pi} e^{ik\hat{x}_l\cdot x(\tau)}[-ik\hat{x}\cdot\nu(\tau)\delta\nu(\tau)\varphi(\tau)]\|x^{'}(\tau)\|d\tau$$

$$\approx \frac{e^{ik\pi}}{\sqrt{8\pi k}}\sum_{j=0}^{2n-1}\frac{\pi}{n}e^{ik\hat{x}_l\cdot x_j}[-ik\hat{x}\cdot\nu_j\delta\nu_j\varphi_j]\|x_j^{'}\|,$$

contributes to the linear system with a term $E_{ij}\delta\nu_j$. The second term is

$$\begin{aligned} S_\infty(\delta\varphi + \kappa\delta\nu\varphi)(\hat{x}_l) &= \frac{e^{ik\pi}}{\sqrt{8\pi k}} \int_0^{2\pi} e^{ik\hat{x}_l \cdot x(\tau)} [\delta\varphi(\tau) + \kappa(\tau)\delta\nu(\tau)\varphi(\tau)] \| x'(\tau) \| d\tau \\ &\approx \frac{e^{ik\pi}}{\sqrt{8\pi k}} \sum_{j=0}^{2n-1} \frac{\pi}{n} e^{ik\hat{x}_l \cdot x_j} [\delta\varphi_j + \kappa_j \delta\nu_j \varphi_j] \| x_j' \|, \end{aligned}$$

which corresponds in the linear system to a term of the form $D_{ij}(\delta\varphi_j + \kappa_j\delta\nu_j\varphi_j)$. An approximating equation alike equation (3.48) is obtained

$$\delta u_\infty(\hat{x}_l) = E_{ij}\delta\nu_j + D_{ij}(\delta\varphi_j + \kappa_j\delta\nu_j\varphi_j). \tag{3.49}$$

Using the pseudo-inverse with tolerance ϵ of S_{ij} equation (3.48) can be rewritten as

$$\delta\varphi_j + \kappa_j\delta\nu_j\varphi_j = (S_\epsilon^+)_{ji}[A_{ij} + B_{ij} + C_{ij}]\delta\nu_j, \tag{3.50}$$

Substituting in equation (3.49) is obtained a discretized expression for the domain derivative in terms of $\delta\nu_j$

$$\delta u_\infty(\hat{x}_l) \approx E_{lj}\delta\nu_j + D_{lj}(S_\epsilon^+)_{ji}[A_{ij} + B_{ij} + C_{ij}]\delta\nu_j. \tag{3.51}$$

To approximate the density function at the curve grid points x_j equation 3.4 to obtain

$$S_{ij}\varphi_j \approx -2e^{ikx_i \cdot d}, \tag{3.52}$$

or

$$(\varphi_\epsilon^+)_j = -2(S_\epsilon^+)_{ji} e^{ikx_i \cdot d}. \tag{3.53}$$

The corresponding expression for the approximated far field pattern is

$$u_\infty(\hat{x}_l) \approx (S_\infty)_{lj}(\varphi_\epsilon^+)_j \tag{3.54}$$

$$= -2(S_\infty)_{lj}(S_\epsilon^+)_{ji}e^{ikx_i\cdot d}. \tag{3.55}$$

3.4 Regularization

We address the problem of regularizing equation (3.2) using a well known pseudo-inverse for matrices with large condition number (see [37] or [41]).

Definition 3.4.1 *Suppose that $A = U\Sigma V^*$ is the singular value decomposition (SVD) of a matrix A (m by n), then we define the pseudo-inverse of A as*

$$A_\epsilon^+ = V\Sigma^+U^*. \tag{3.56}$$

The singular values $\sigma_1, ..., \sigma_r$ in decreasing order are on the diagonal of Σ (m by n) and the reciprocals $1/\sigma_j$ on the diagonal of Σ^+ for $1 \leq j \leq r$ for some $r \leq m$, $r \leq n$.

Definition 3.4.2 *Suppose that $A = U\Sigma V^*$ is the singular value decomposition (SVD) of a matrix A (m by n), then we define the pseudo-inverse of A with tolerance ϵ as*

$$A_\epsilon^+ = V\Sigma_\epsilon^+U^*. \tag{3.57}$$

The singular values $\sigma_1, ..., \sigma_r$ in decreasing order are on the diagonal of Σ (m by n) and the reciprocals $1/\sigma_j$ on the diagonal of Σ_ϵ^+ for $1 \leq j \leq r$

for some r such that $\frac{\sigma_{r+1}}{\sigma_1} < \epsilon$ and $\frac{\sigma_r}{\sigma_1} \geq \epsilon$. The rest of the diagonal elements of Σ_ϵ^+ are equal to zero.

This pseudo-inverse allows to look for an "effective rank" of the matrix, relative to the number of significant digits we are working with. Based on the accuracy of the data, we decide on a tolerance ϵ and count only the singular values above it. We can formalize this discussion with the help of the following

Theorem 3.4.1 *Suppose that $A = U\Sigma V^*$ is the singular value decomposition (SVD) of a matrix A (m by n) with rank k, then*

A) For any $1 \leq r < k$, the matrix A_r (m by n) of rank r that minimizes $\|A - A_r\|_2$ is given by

$$A_r = \sigma_1 u_1 v_1^* + ...\sigma_r u_r v_r^* \tag{3.58}$$

and the minimum is $\|A - A_r\|_2 = \sigma_{r+1}$.

B) For any $\epsilon > 0$, the matrix A_{min} of minimum rank among all the matrices A' that satisfy $\|A - A'\|_2 \leq \epsilon$ is the same matrix from A), where $\sigma_{r+1} \leq \epsilon$ and $\sigma_r > \epsilon$.

It is a well known fact that the minimum length least squares solution to a linear system $Ax = b$ is $x^+ = A^+b = V\Sigma^+U^*b$. The following is a derivation of a bound of the error of the approximate solution to the linear system using A_ϵ^+. On one hand we have

$$\begin{aligned} \|A_r x^+ - b\|_2 &\leq \|A_r x^+ - Ax^+\|_2 + \|Ax^+ - b\|_2 && (3.59) \\ &\leq \|A_r - A\|_2 \|x^+\|_2 + \|Ax^+ - b\|_2 && (3.60) \\ &= \sigma_{r+1}\|x^+\|_2 + \|Ax^+ - b\|_2. && (3.61) \end{aligned}$$

Similarly,

$$\|Ax^+ - b\|_2 \leq \sigma_{r+1}\|x^+\|_2 + \|A_r x^+ - b\|_2, \tag{3.62}$$

and both inequalities combined lead to

$$| \, \|Ax^+ - b\|_2 - \|A_r x^+ - b\|_2 \, | \leq \sigma_{r+1}\|x^+\|_2. \tag{3.63}$$

It turns out that, with all parameters fixed, both an early cutoff and a late cutoff lead to a poor approximation; in the first case because many singular values are dropped, in the second case because the condition number of the approximating matrix A_r approaches the actual condition number of the discretized equation (3.2) as we include more singular values.

Chapter 4

Numerical Examples

In this chapter the method of continuation is presented in practice. Section 4.1 contains some remarks about the numerical experiments conducted along this chapter with the method. In section 4.2 the results of a test of stability are shown; the tests from [31] and [34] are used as a model in the design of our test. Finally, in section 4.3 we include some examples of the reconstruction of non-convex obstacles; examples are focused on the reconstruction of shapes with big concavities, like the "bitten donut" shown in figure 4.38 in p. 85.

4.1 Numerical Experiments

Numerical experiments to solve the inverse problem use synthetic far field data, which is obtained solving the direct problem with the method recommended in [9]. In the direct problem, the number of grid points on the obstacle boundary curve is equal to 256 in all experiments. In the inverse problem, the number of grid points on the approximated boundary curve is calculated using a heuristic rule of ten equidistant grid points per wavelength of the incident field; the

number of observation points of the far field pattern is set equal to this same number in both, the direct and inverse problems. Obstacles are probed using several incoming plane waves as described in section 3.1. In each iteration the relative error of the far field pattern is required to become smaller than 10% or the iteration is repeated with the wavenumber step-size reduced by a factor of 0.5. The wavenumber step-size is split at most 10 times in this adaptive march. For a stopping rule we use the relative residual

$$Res = \frac{\|x_i - x_{i+1}\|_{L^2}}{\|x_{i+1}\|_{L^2}}, \tag{4.1}$$

where x_i, x_{i+1} denote the approximated boundary curves obtained in the i^{th} and $(i+1)^{th}$ iterations. Iterations are stopped when the relative residual Res is less than a tolerance value ϵ or the wavenumber is equal or greater than a maximum value allowed k_{max}. In examples shown throughout this chapter we used an initial curve to start the iteration.

4.2 Stability Test

A test for stability with respect to random errors added to the data is applied to the method of continuation. The test consists of twin iterations with the real and imaginary parts of the data multiplied by a factor of $1 + \epsilon R$ in one of them, where $0 < \epsilon \leq 0.1$ and R is a random number in the interval $[-1, 1]$.

In the examples presented along this section we reconstruct the obstacle shown in figure 4.1. The obstacle is probed using three incoming plane waves with direction angles $\pi/3$, π and $5\pi/3$. The stopping condition is: the relative residual $Res < 10^{-3}$ or the wavenumber $k \geq 30$. In examples **1** to **6** the size of

Table 4.1: In this examples are tested several wavenumber step-sizes versus an earlier and a later cutoff.

	cutoff $= 0.1$	cutoff $= 0.01$
$\delta k = 2$	example 1	example 2
$\delta k = 1$	example 3	example 4
$\delta k = 0.25$	example 5	example 6

the noise is equal to 1% and the initial curve is the unit circle centered at the origin. The regularization cutoff and wavenumber step-size are chosen according to table 4.1.

In examples **7** and **8** the circle that serve as initial curve was changed from the unit circle centered at the origin. In these two examples the cutoff value is equal to 10^{-1} and the size of the noise added to the data is equal to 1.5% and 2% respectively. The obstacle is still reconstructed within two significant digits.

From the results displayed in this set of examples we like to highlight the following (by approximation we mean the approximated boundary curve approaching the scatterer boundary):

- In the current setting, two significant digits in the far field pattern data are precise enough in order to reconstruct the obstacle boundary,
- To an earlier cutoff corresponds more stability; to a later cutoff corresponds a faster approximation,
- To a greater wavenumber step-size corresponds a stronger boost in the curve update. To a smaller wavenumber step-size corresponds more con-

Figure 4.1: This figure shows the obstacle used for the stability test.

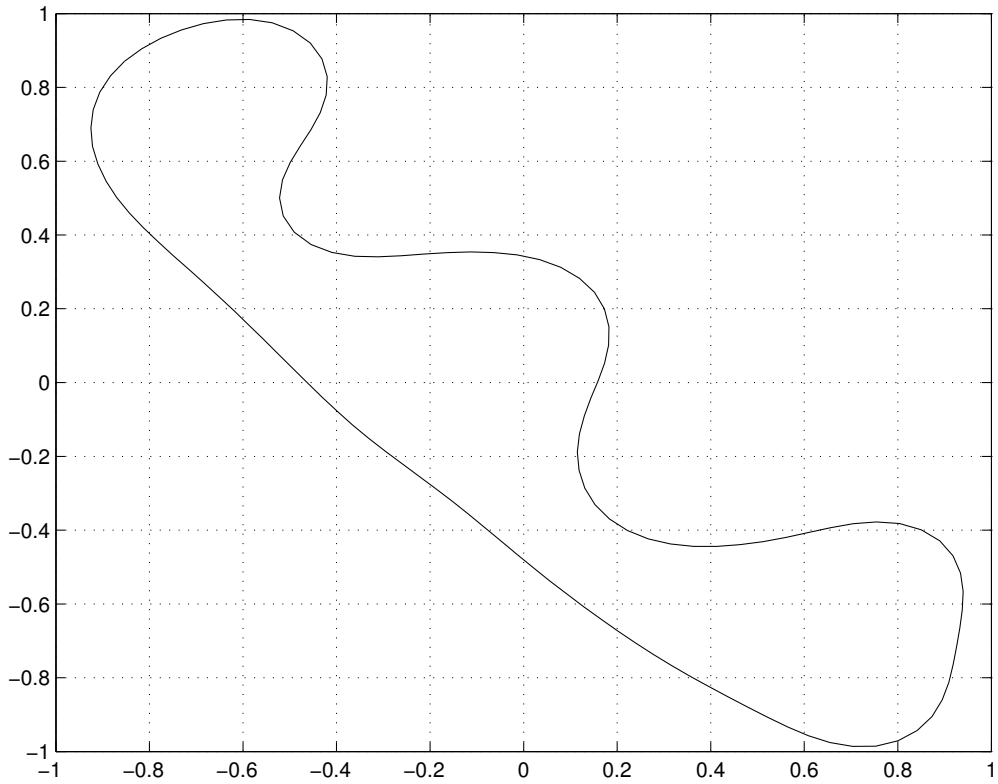

trol over the far field relative error.

- It is always possible to continue the iterations in order to further improve an approximation (although an approximation cannot be improved beyond two or three significant digits in the current setting).

These observations motivate the subject of the next section, where obstacles having a big concavity are probed.

4.2.1 Example 1

In figures 4.2 and 4.3 plots in the left column and the right column correspond to unperturbed and perturbed data respectively[1]; the wavenumber of the iteration is indicated in the bottom left of each plot. Notice that with an error in the data of 1% the difference between two corresponding plots with unperturbed and perturbed data can hardly be told by inspection. On the other hand, in figure 4.5 it can be seen that the relative residual of later iterations is more sensible to the introduced error. In figure 4.4 the initial curve, the target curve, the best approximation achieved are depicted, as well as the corresponding curve obtained with perturbed data as indicated in the legend inside the figure.

[1] All figures having 6 sub-plots are organized in this way

Figure 4.2: This figure depicts the target curve and the first three iterations, the initial curve is also shown in the plot corresponding to the first iteration.

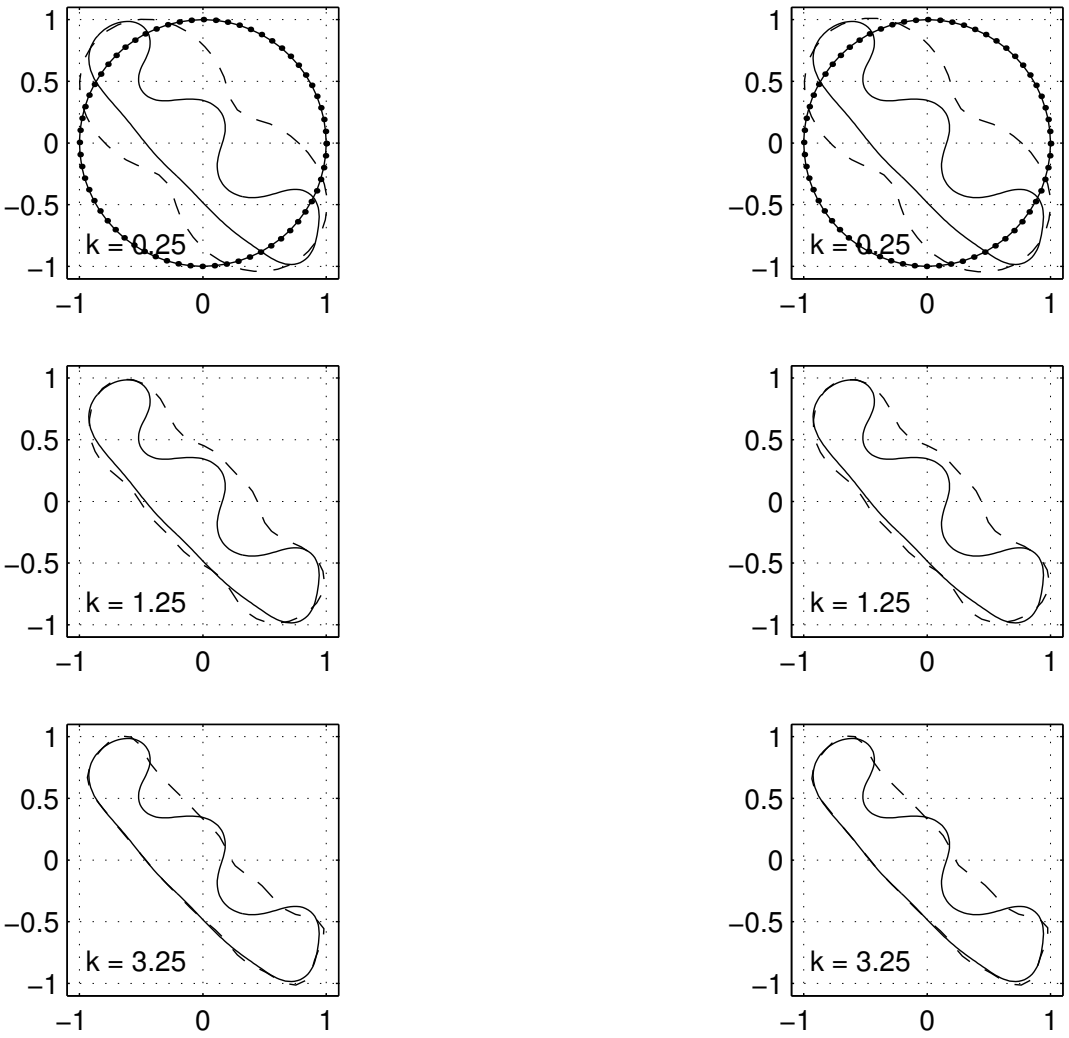

Figure 4.3: This figure shows some intermediate iterations. Intuitively, we see that iterations with smaller wavenumber "locate" the scatterer whereas iterations with greater wavenumber "reconstruct" its fine details.

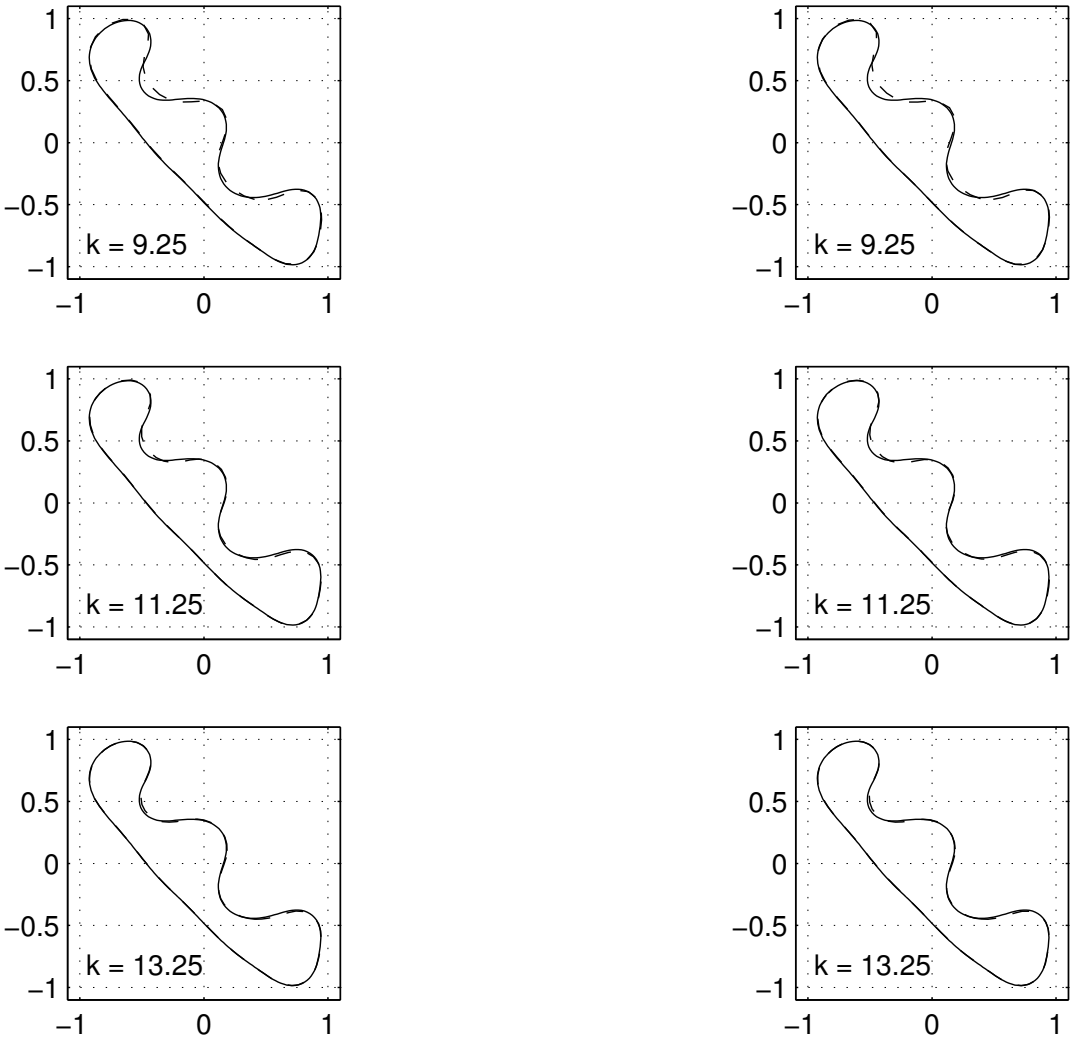

Figure 4.4: In this figure are the initial curve, the target curve and the best approximation achieved with unperturbed and perturbed data as indicated in the legend in the figure.

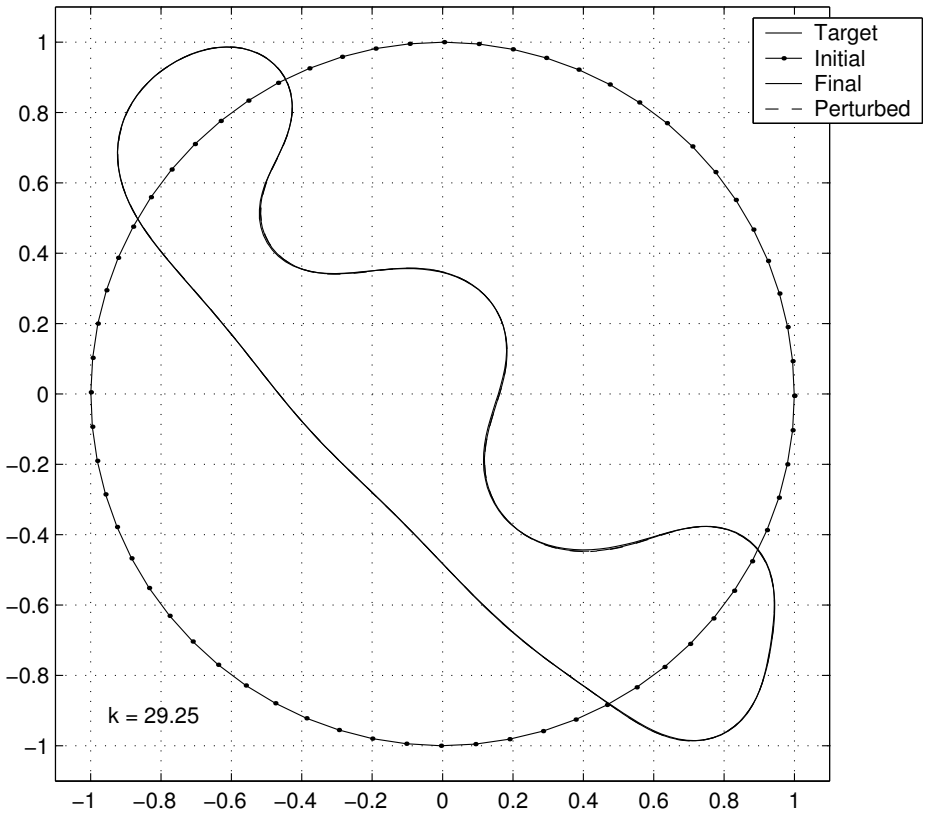

Figure 4.5: This figure shows the relative residual as a function of wavenumber in semi-logarithmic scale. In later iterations the relative residual is more sensible to the introduced error.

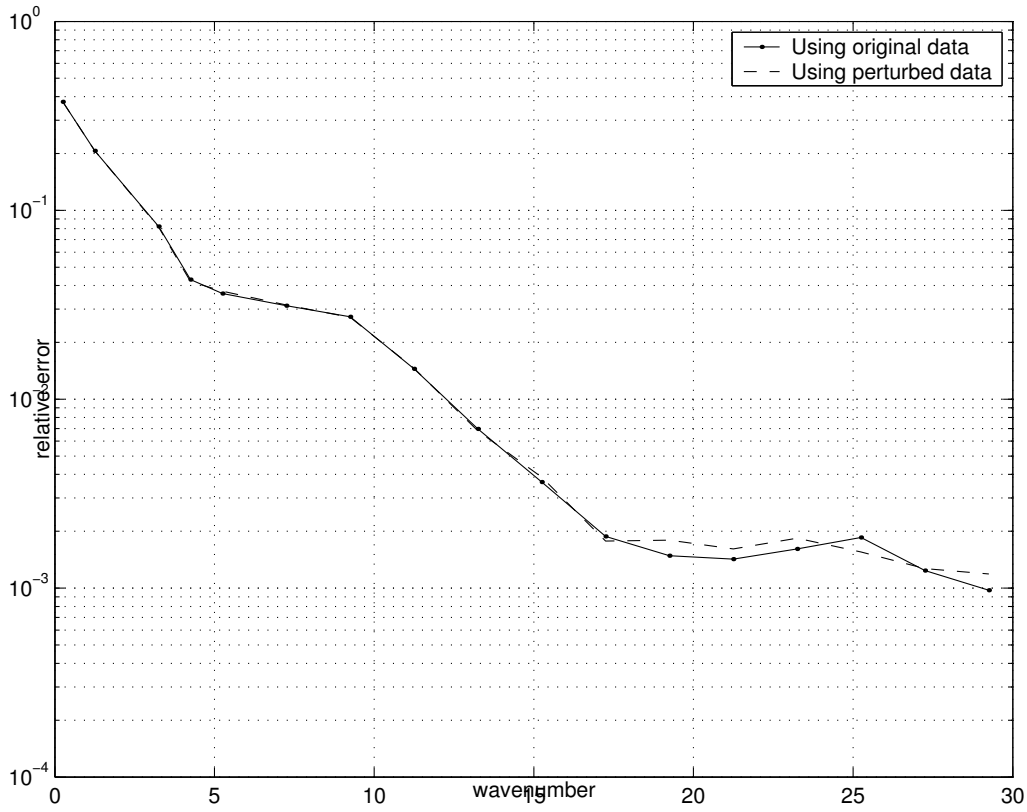

4.2.2 Example 2

This is the same as Example 1, except that the cutoff has been changed from 10^{-1} to 10^{-2}. In figure 4.6 it can be seen that it was necessary to take a smaller wavenumber step-size in the first and second iterations. In the previous example only the first iteration required a smaller wavenumber step-size. In figure 4.7 it is apparent that the difference between target curve and best approximation achieved is as tiny as in our previous example. In this example the relative residual does not decrease below 10^{-3} in the chosen wavenumber interval, and it is more sensitive to the introduced error compared to the case of cutoff $= 10^{-1}$, see figure 4.8.

Figure 4.6: In the first iterations it may be necessary to take a smaller wavenumber step-size.

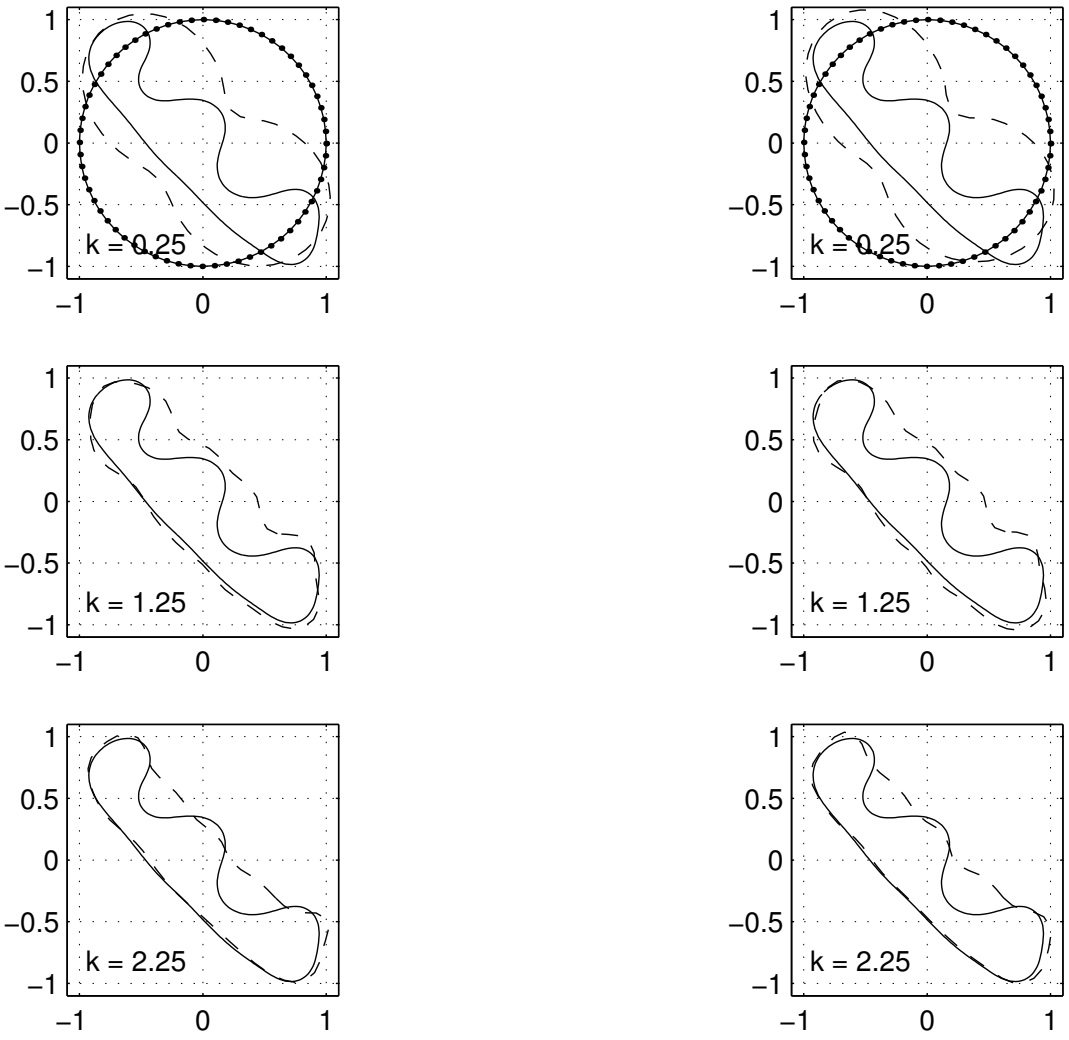

Figure 4.7: The difference between the target and reconstructed curve can hardly be told by inspection.

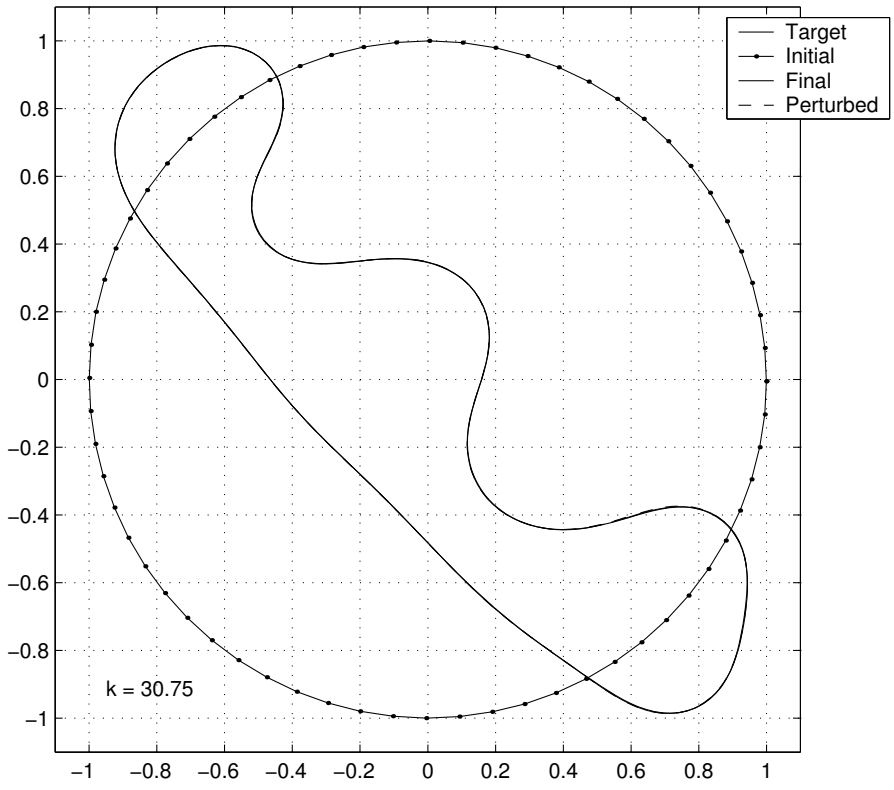

Figure 4.8: The relative residual as a function of wavenumber. In this case the relative residual corresponding to perturbed data decreases more slowly compared to example 1.

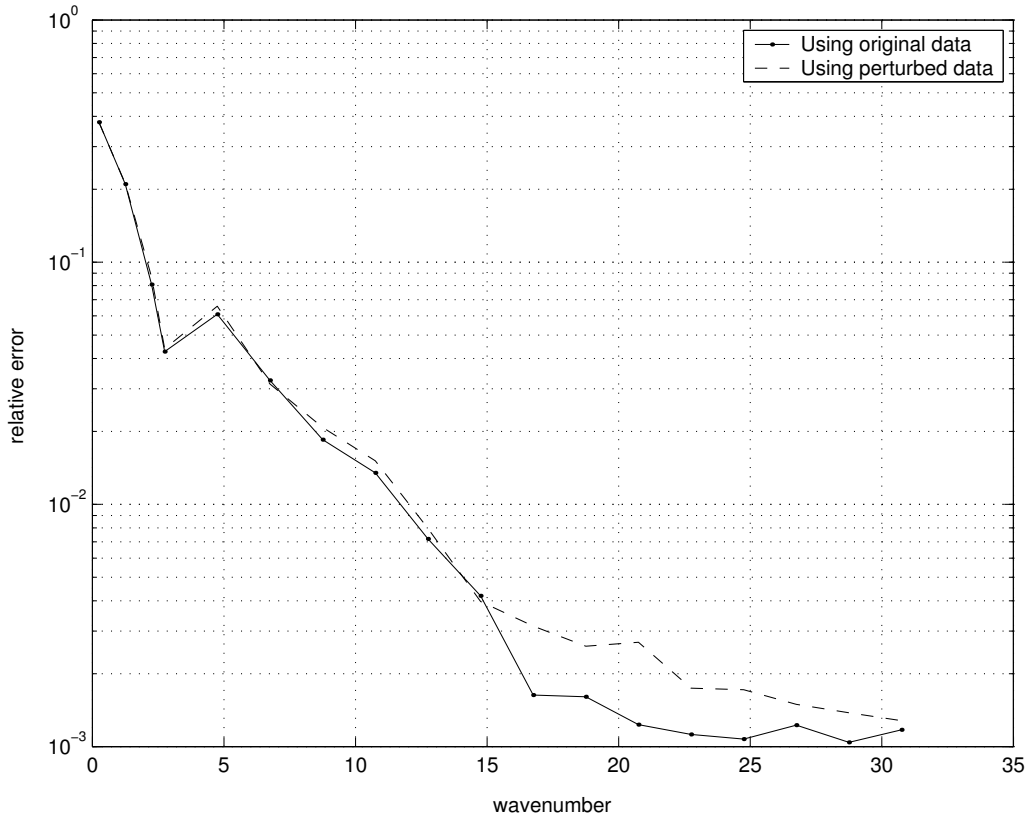

4.2.3 Example 3

In this example the regularization cutoff value is 10^{-1} and the wavenumber step-size is 1. Only in the first iteration a smaller wavenumber step-size is necessary, see figure 4.9. The wavenumber relative residue decreases below 10^{-3} at wavenumber $k = 26.25$, see figure 4.11.

Figure 4.9: In the first iteration it may be necessary to take a smaller wavenumber step-size.

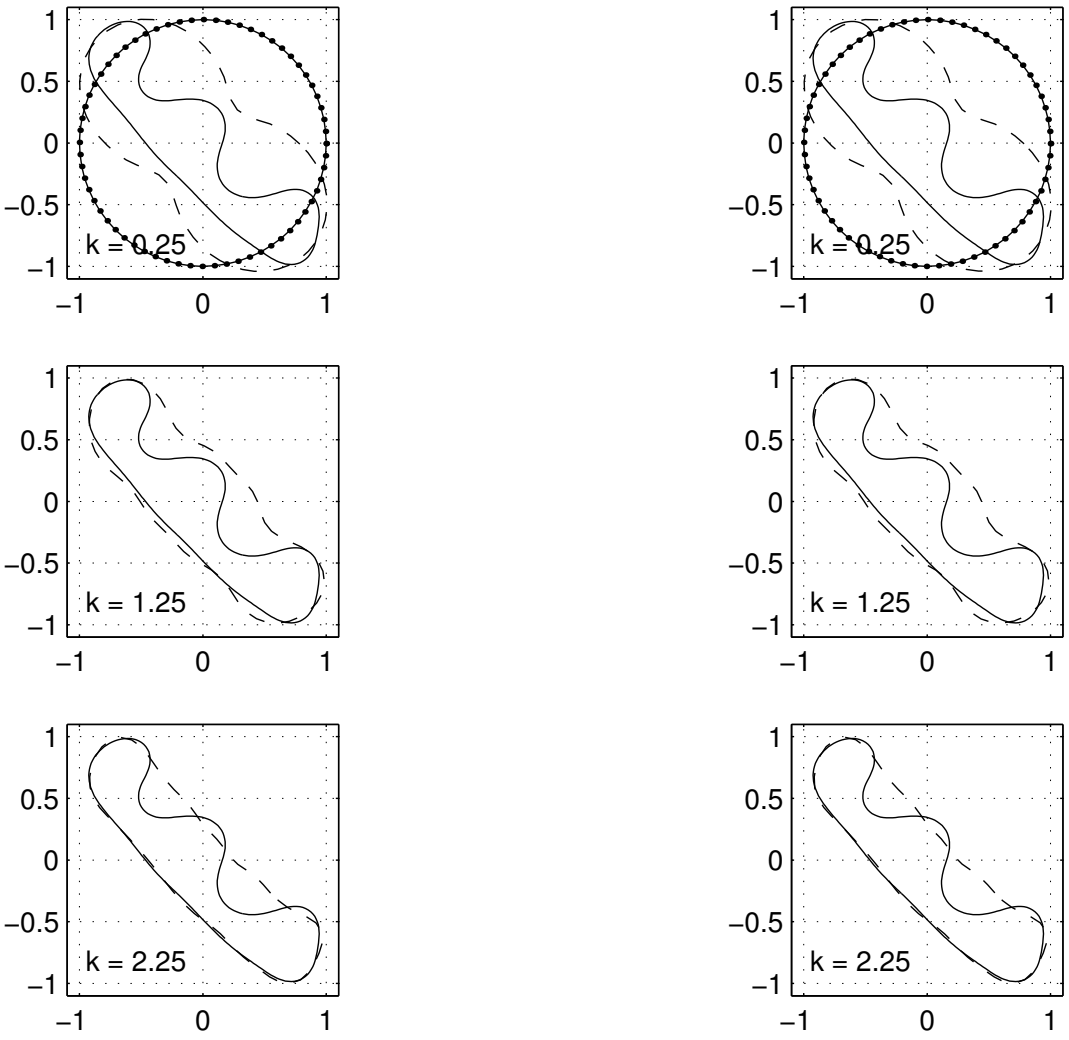

Figure 4.10: The obstacle boundary is reconstructed within two significant digits.

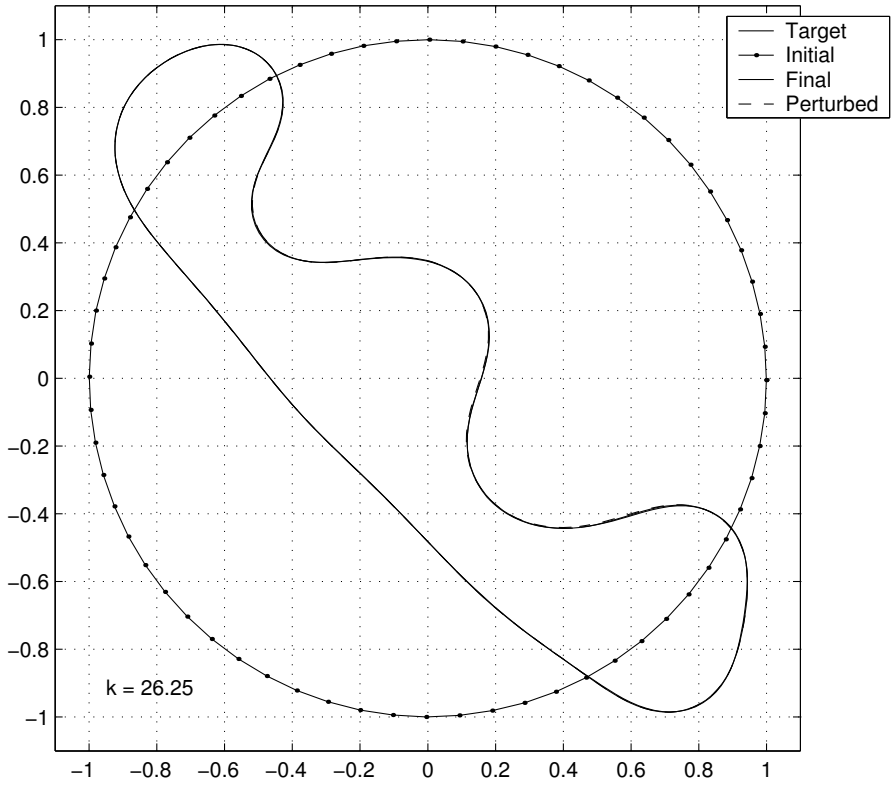

Figure 4.11: The relative residual as a function of the wavenumber. The wavenumber relative residue decreases below 10^{-3} at wavenumber $k = 26.25$.

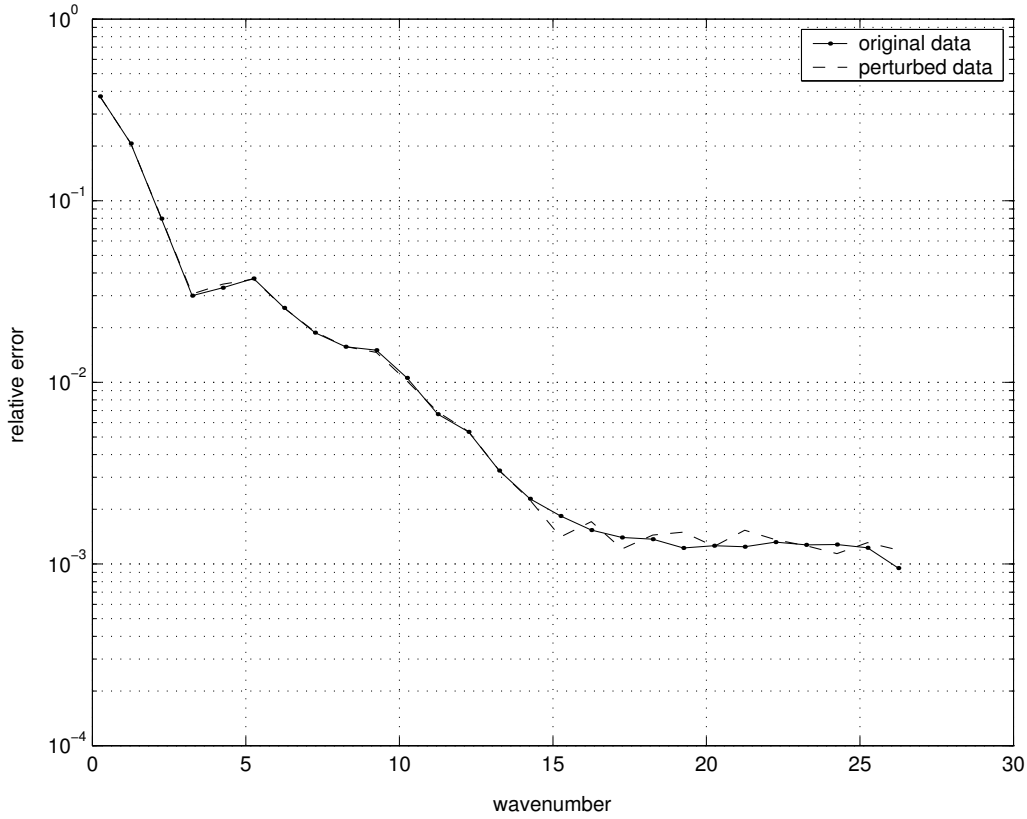

4.2.4 Example 4

This is the same as example 3 except that the regularization cutoff value has been changed from 10^{-1} to 10^{-2}, the wavenumber step-size is 1. The best approximation achieved of the obstacle boundary curve is about the same as in example 3, see figure 4.13. The wavenumber relative residual decreases below 10^{-3} at wavenumber 29.75, see figure 4.14.

Figure 4.12: In the considered examples the difference between iterations with perturbed and unperturbed data is tiny.

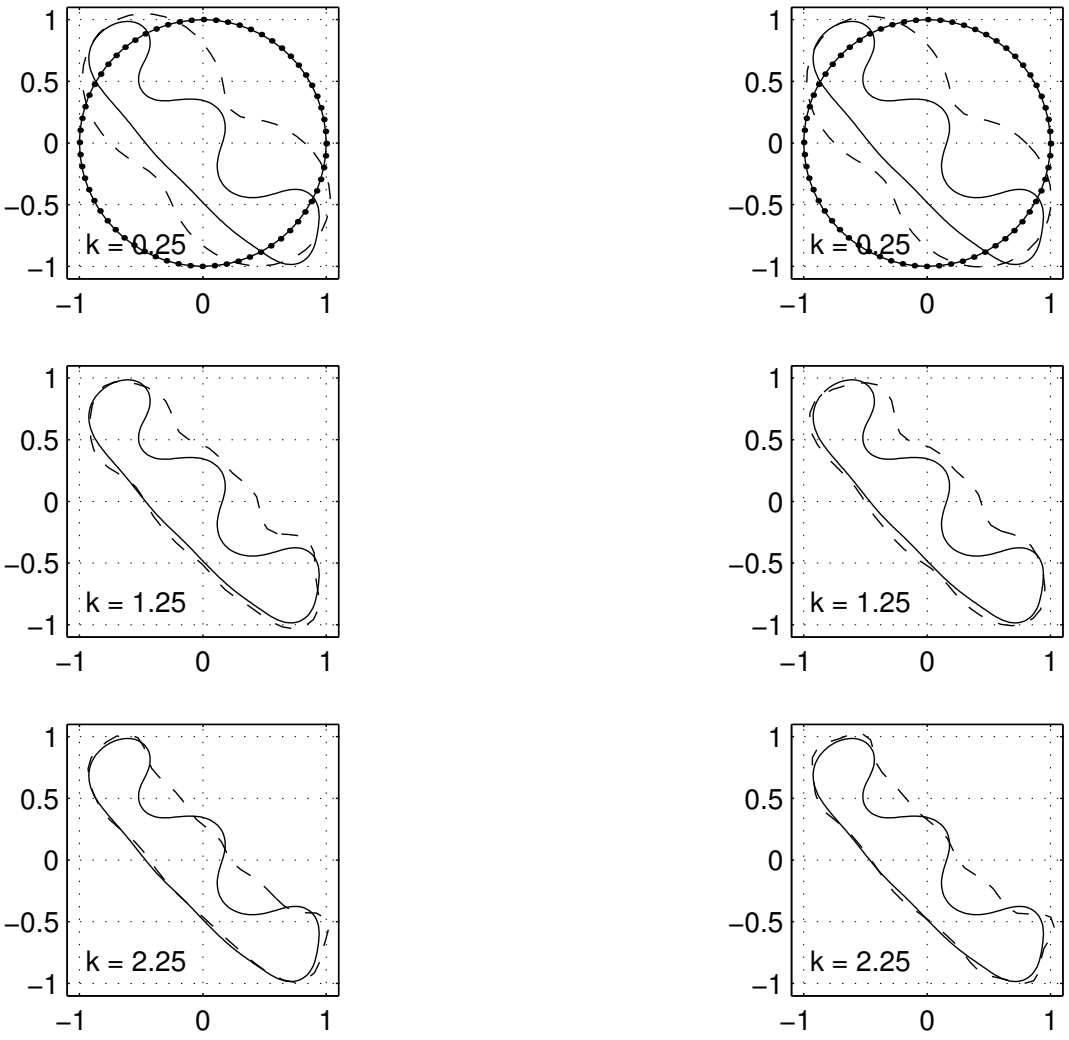

Figure 4.13: In this figure the target curve is depicted, as well as the initial curve and the best approximation achieved with perturbed and unperturbed data.

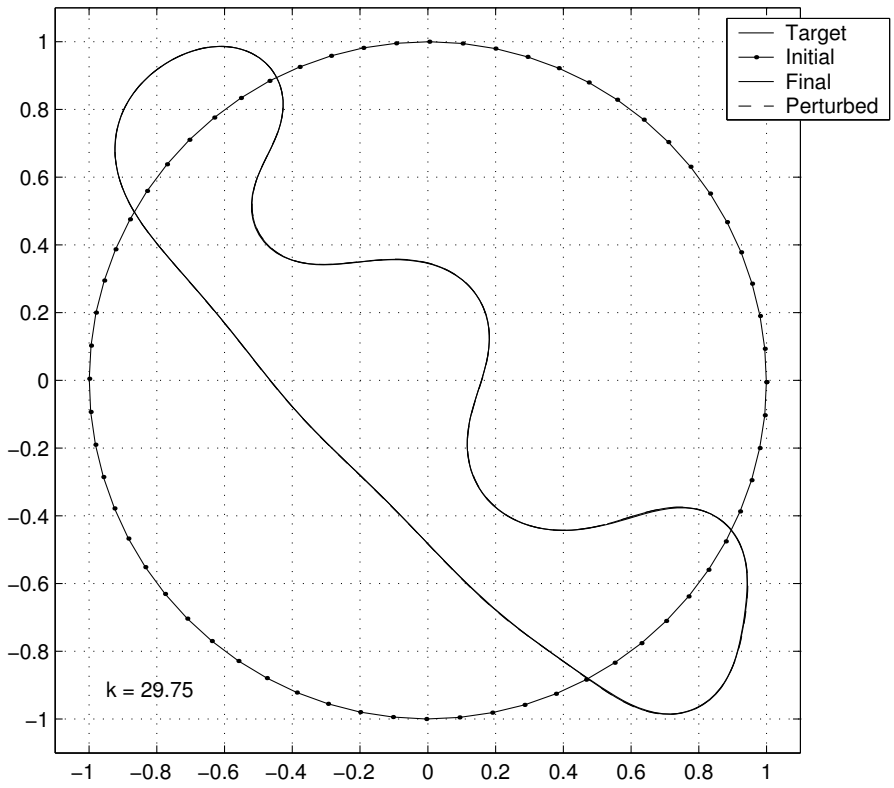

Figure 4.14: The relative residual as a function of wavenumber. The wavenumber relative residual decreases below 10^{-3} at wavenumber 29.75.

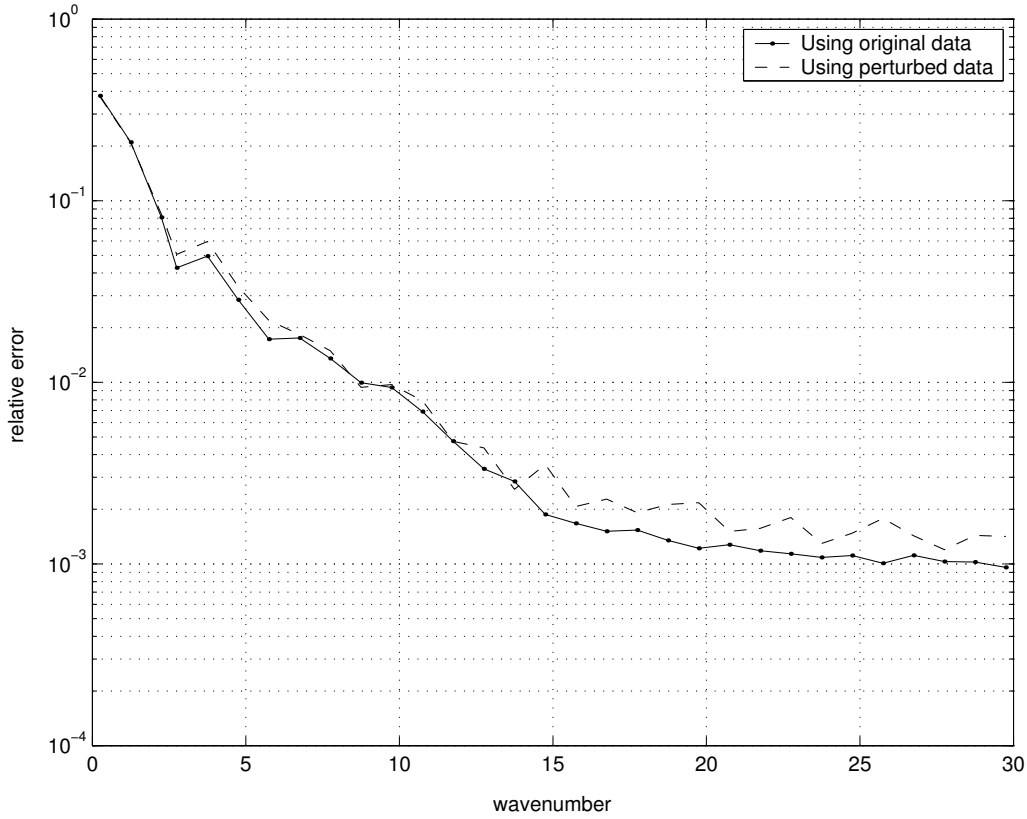

4.2.5 Example 5

In this and the next example is used a wavenumber step-size of 0.25, in this example the cutoff value is 10^{-1}. The relative residual does not decrease below 10^{-3} in the chosen wavenumber interval, see figure 4.17. This experiment is more expensive since many iterations are required. But in figure 4.16 we see that the reconstruction of the scattering obstacle with perturbed and unperturbed data is as good as in previous examples.

Figure 4.15: A smaller wavenumber step-size produces a smaller change in the curve update.

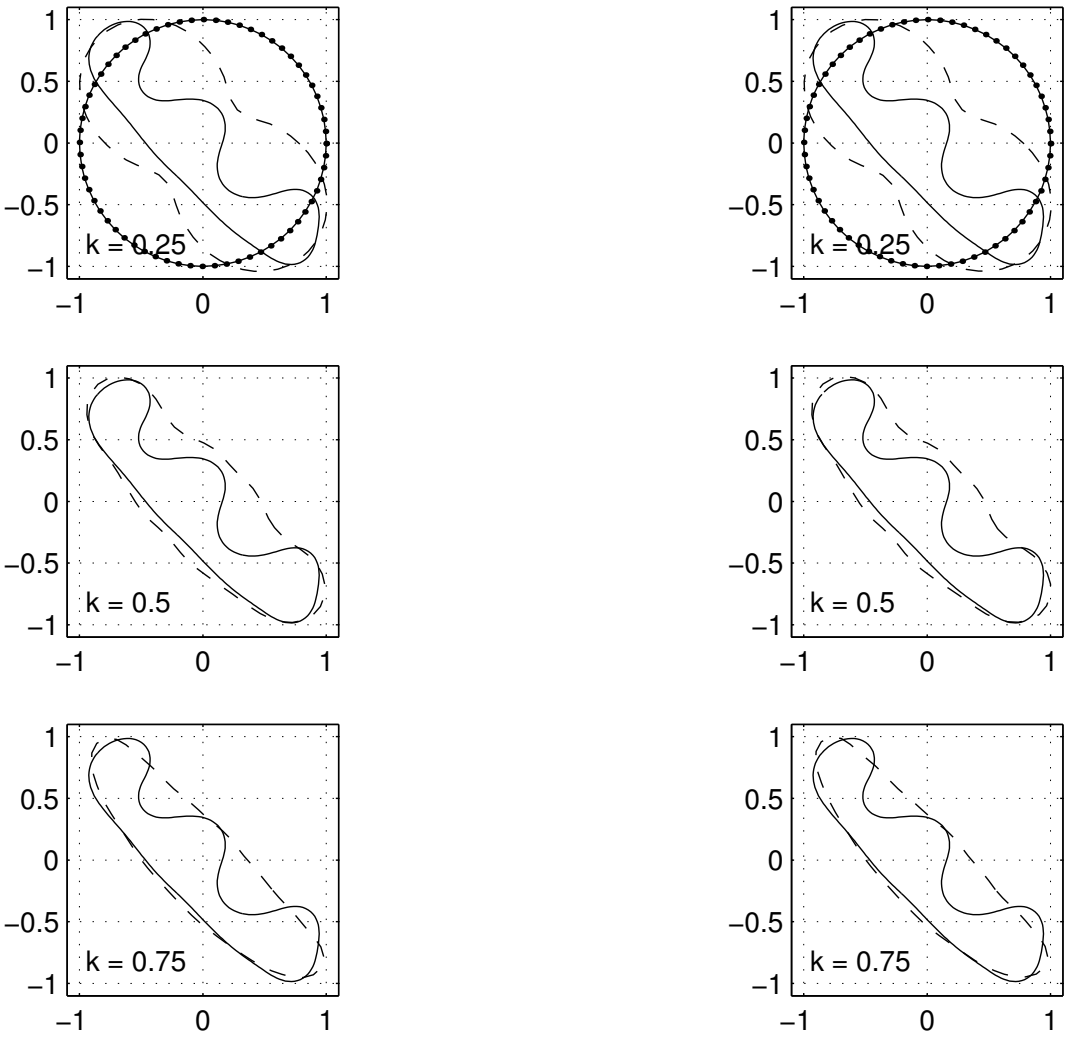

Figure 4.16: The best approximation achieved is as good as in previous examples.

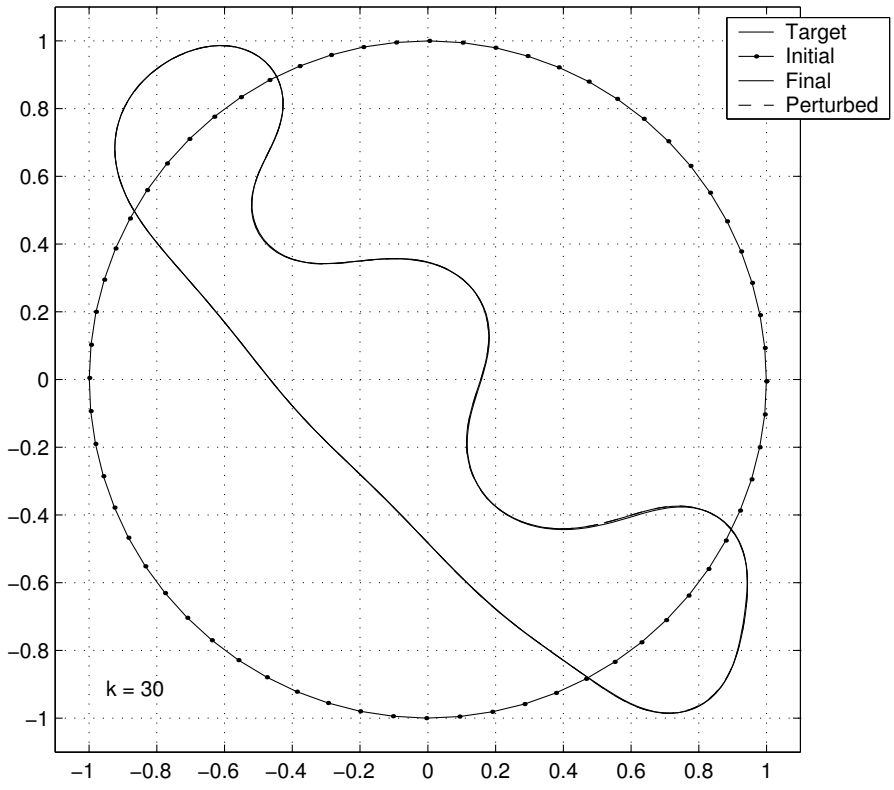

Figure 4.17: The relative residual does not decrease below 10^{-3} within the chosen wavenumber interval.

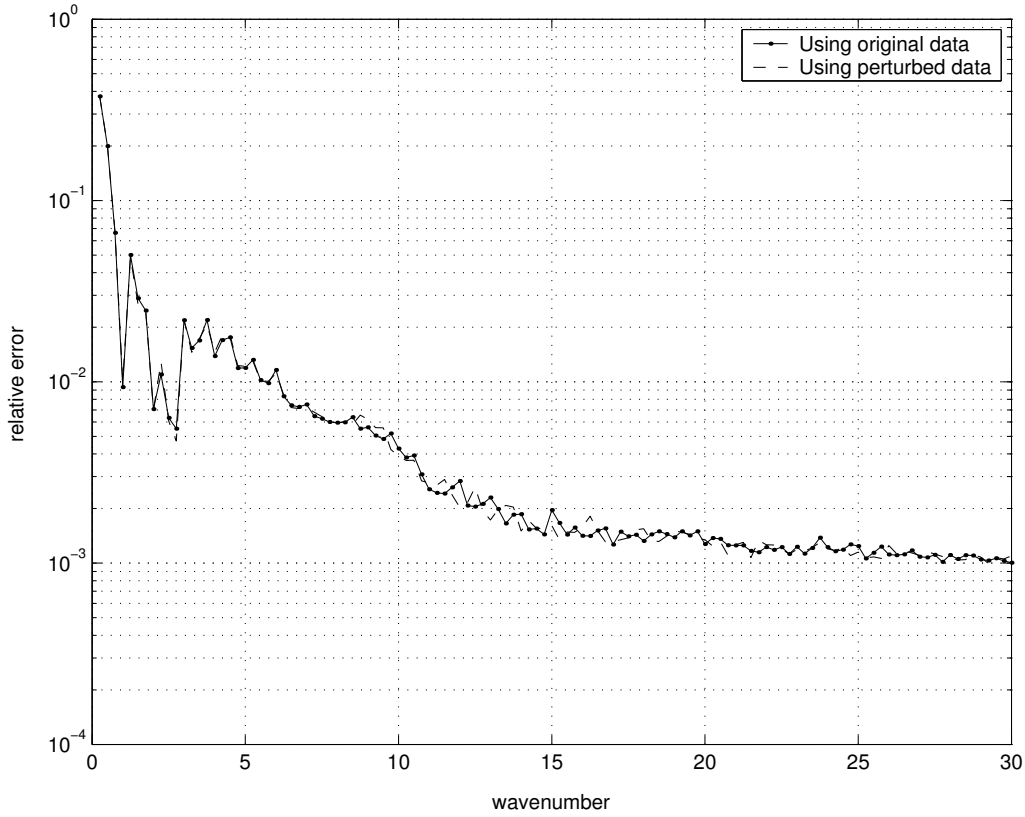

4.2.6 Example 6

Finally, in this example the wavenumber step-size is 0.25 and the regularization cutoff value is 10^{-2}. As expected, the relative residual is bigger for the perturbed data, and it does not decrease below 10^{-3} in the chosen wavenumber step-size, see figure 4.20. Presumably a smaller wavenumber step-size produces smaller curve updates for a given cutoff value, although in figure 4.19 we see that the reconstruction of the obstacle boundary is as good as in previous examples.

Figure 4.18: A smaller wavenumber step-size produces a smaller approximated boundary curve update, like in example 5.

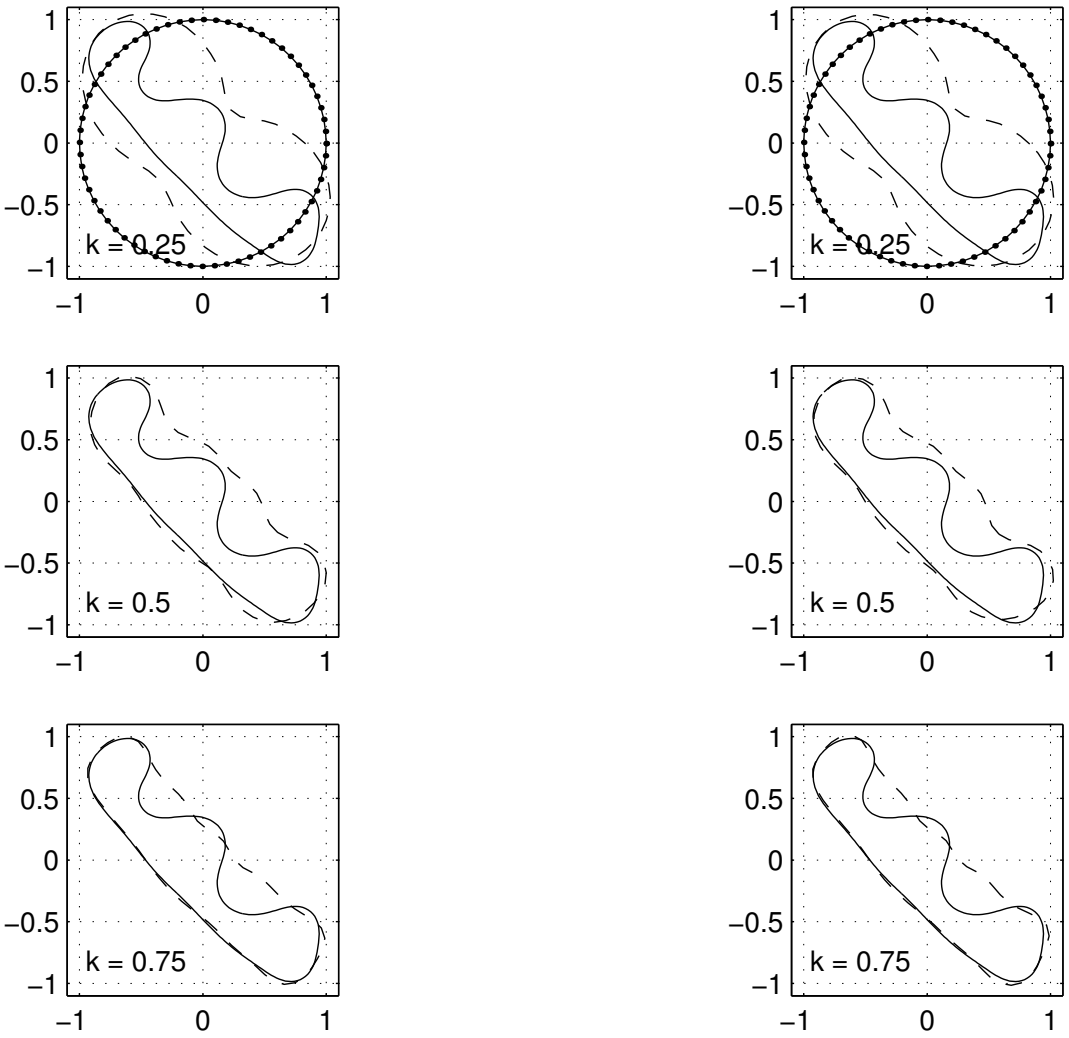

Figure 4.19: Although the relative residual is bigger for perturbed data, the best approximation achieved with unperturbed and perturbed data are not distinguishable by simple inspection.

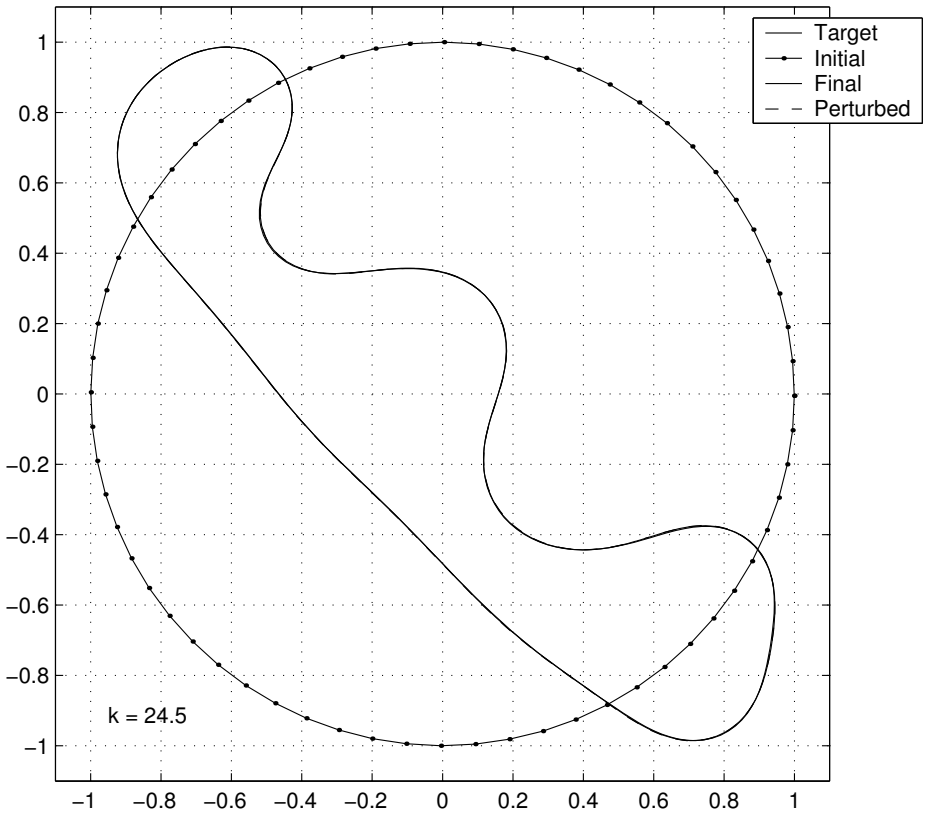

Figure 4.20: Among the considered examples, this is the case where the relative residual is more sensitive to the error introduced.

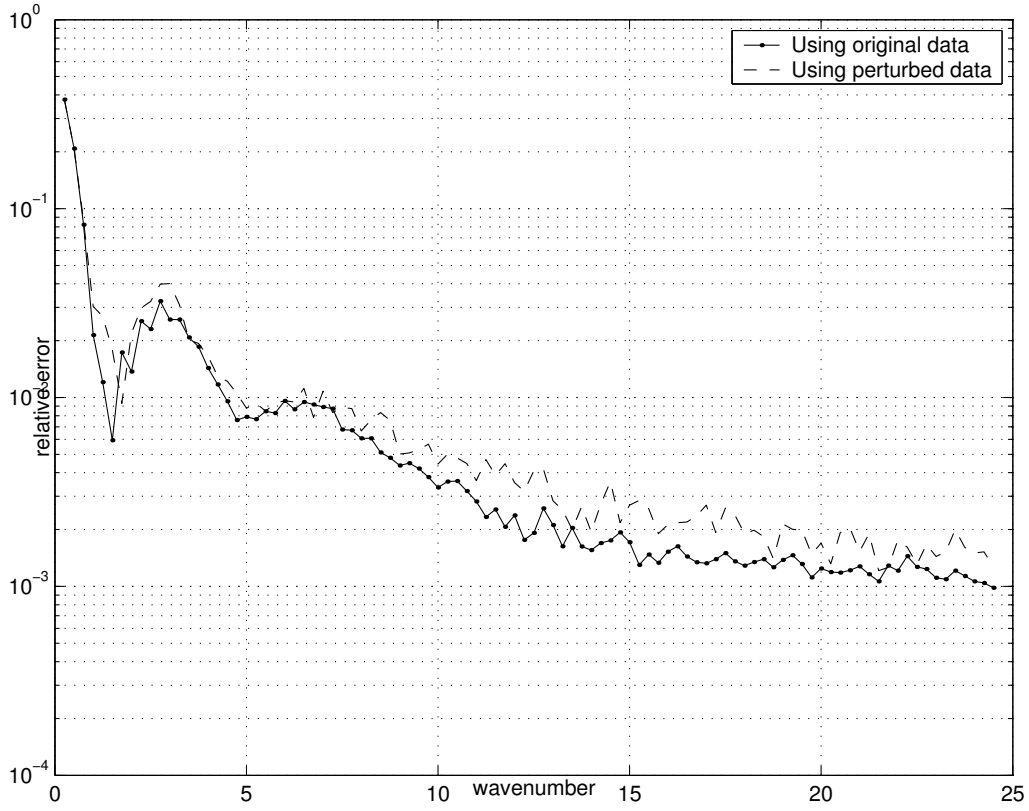

4.2.7 Example 7

This time the initial curve is the circle of radius 0.5 centered at $(0.3, -2.5)$. The initial curve chosen is a good initial guess for the iterations provided the wavenumber step-size in the early iterations is small enough. In the first three iterations smaller wavenumber step-sizes are required, see figure 4.21. The wavenumber step-size is 1 and the regularization cutoff is 10^{-1}. The relative residual decreases below 10^{-3} at wavenumber $k = 25.69$, see figure 4.23.

Figure 4.21: The initial curve chosen is a good initial guess for the iterations, wavenumber step-sizes are small in early iterations.

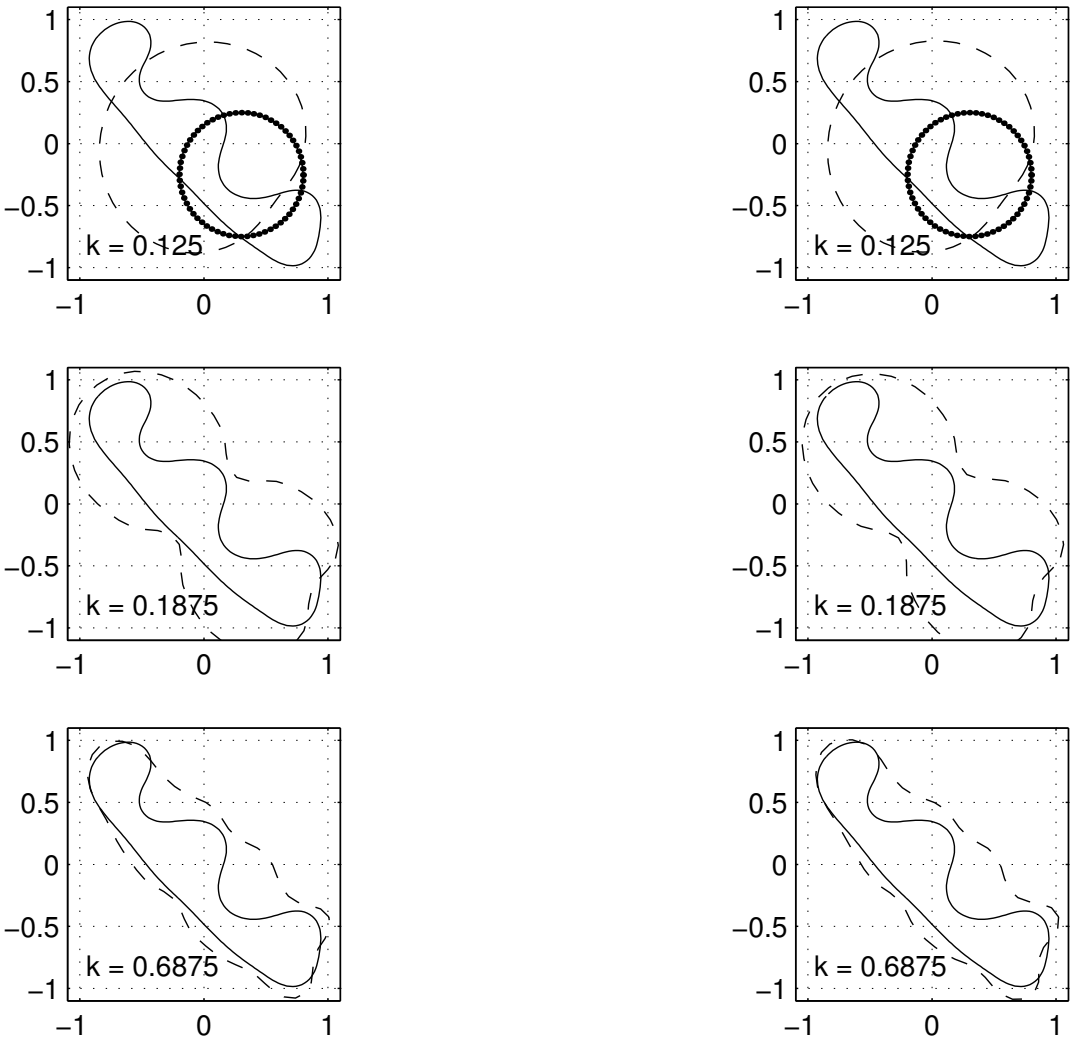

Figure 4.22: This figure depicts the initial curve, the target curve and the best approximation achieved with perturbed and unperturbed data.

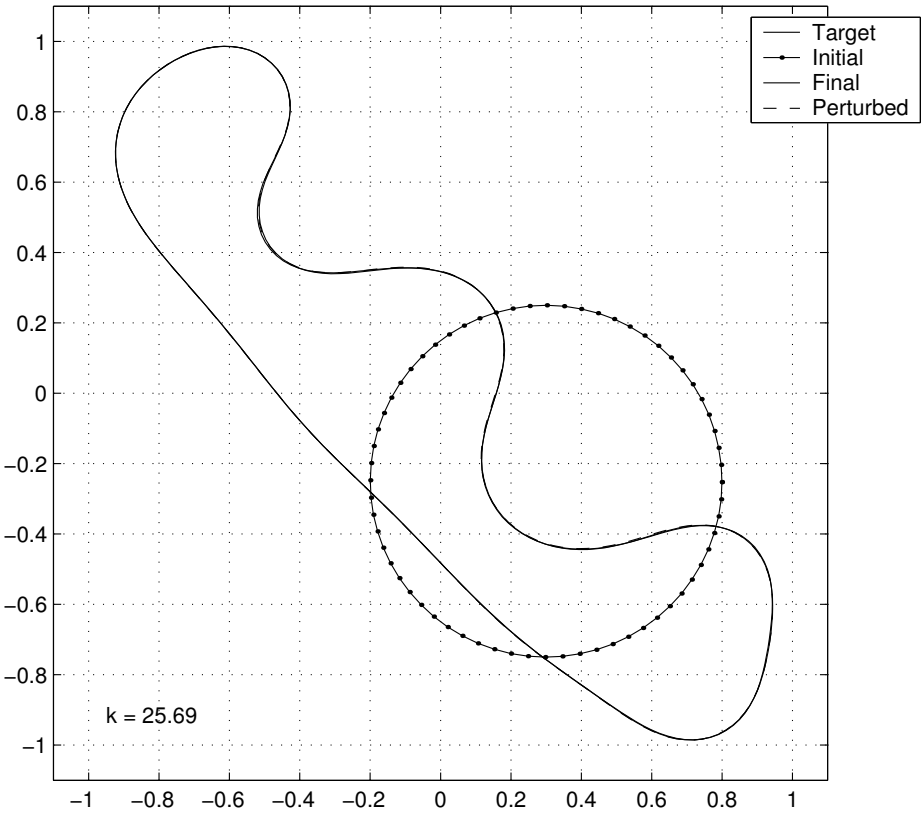

Figure 4.23: The relative residual decreases below 10^{-3} at wavenumber $k = 25.69$.

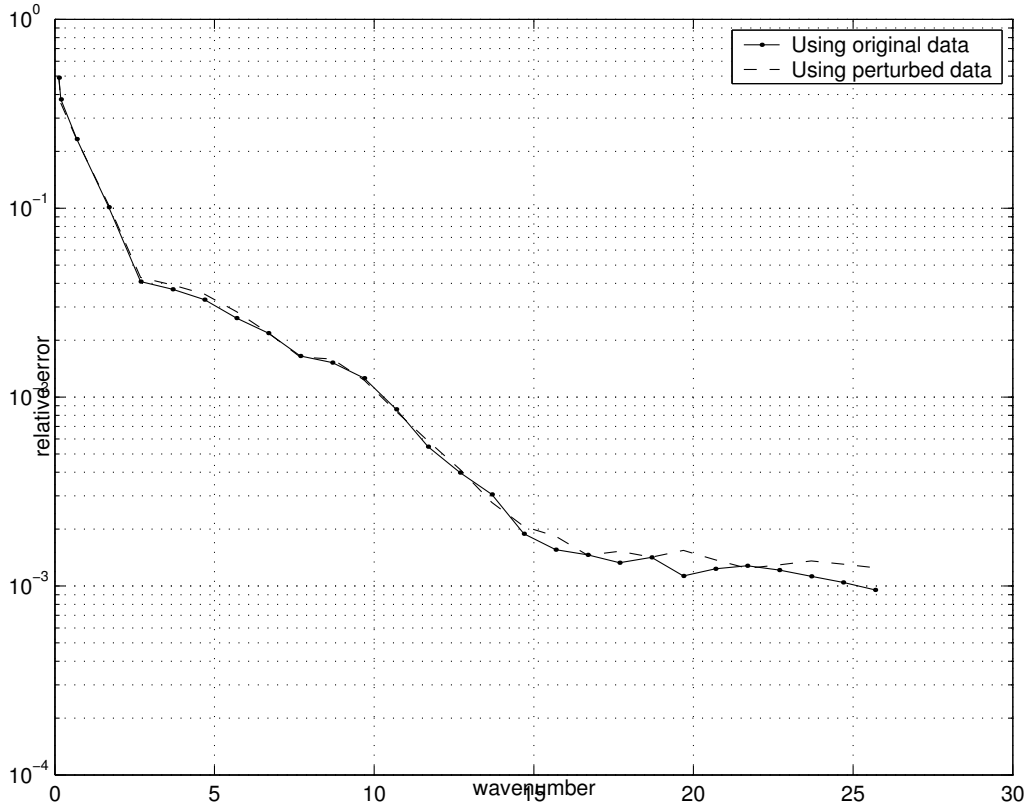

4.2.8 Example 8

In this example the initial curve is the circle of radius 2 centered at $(-0.15, -0.2)$. In the first and second iterations smaller wavenumber step-sizes are required, see figure 4.24. The relative residual does not decrease below 10^{-3} in the chosen wavenumber interval, see figure 4.26. In figure 4.25 it can be seen that the circle chosen as initial curve is not "close" to the obstacle boundary curve.

Figure 4.24: This time the initial curve is not shown in the first three iterations.

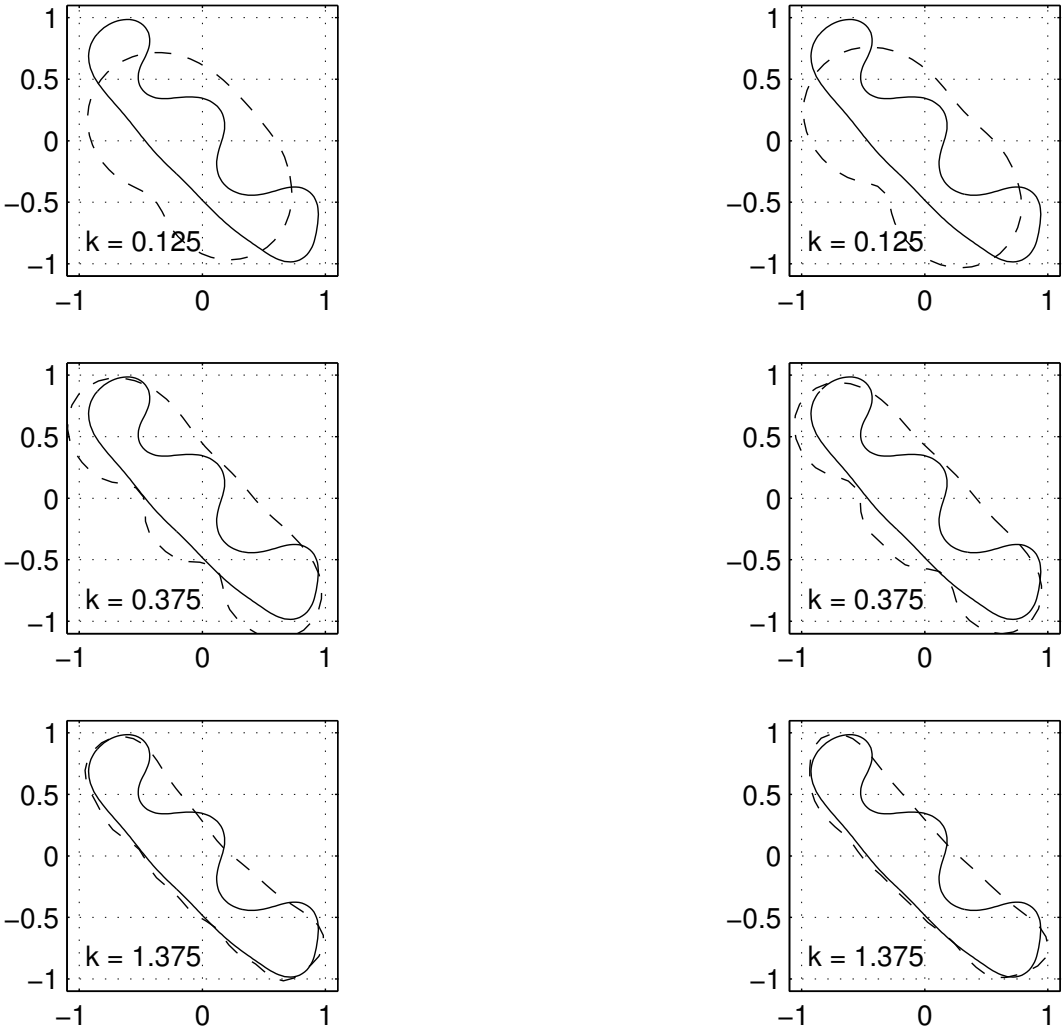

Figure 4.25: This figure depicts, as before, the initial curve, the target curve and the best approximation achieved with perturbed and unperturbed data.

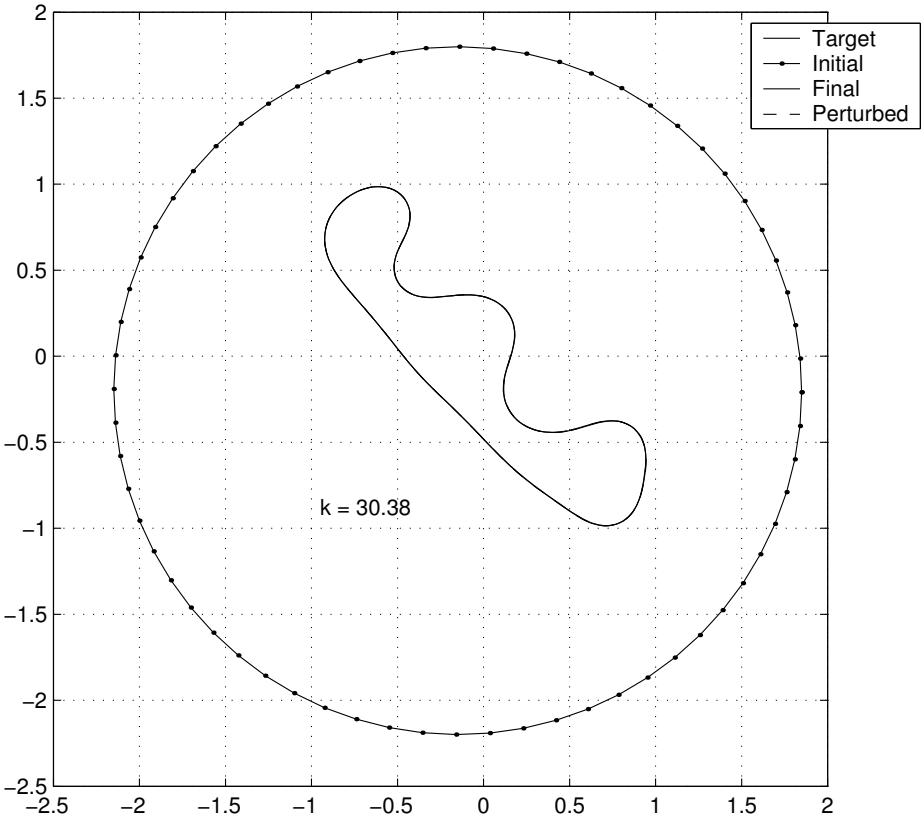

Figure 4.26: Although the relative residual decreases considerably, it does not decrease below 10^{-3} in the chosen wavenumber interval.

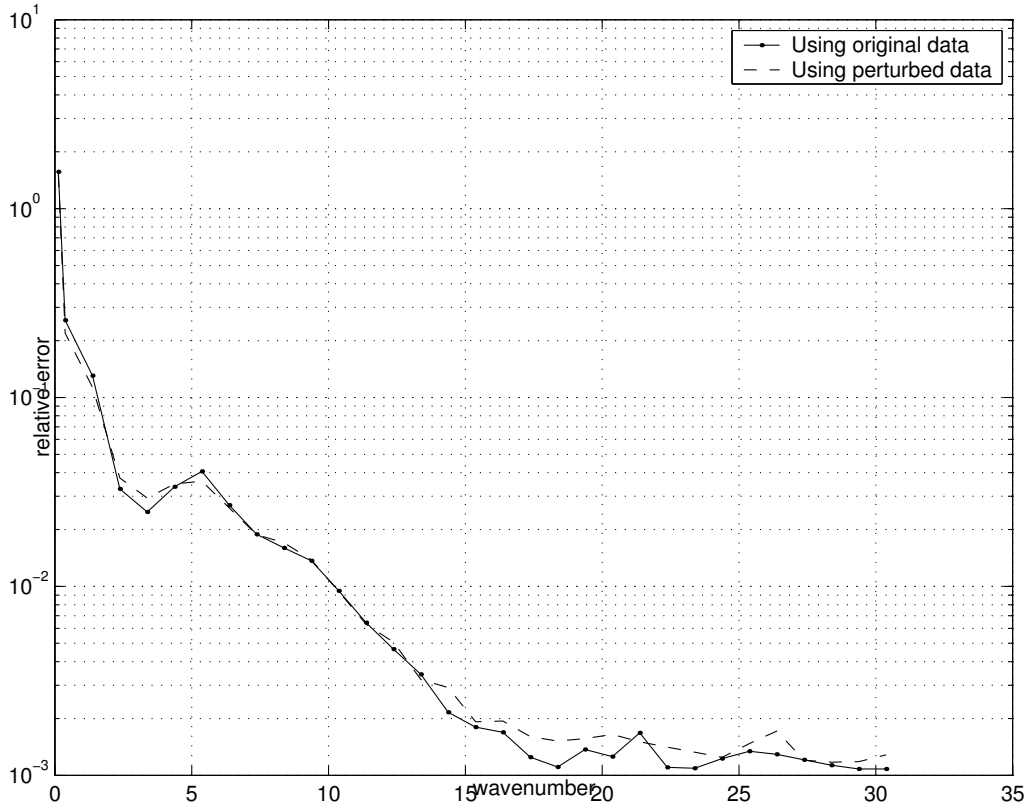

Table 4.2: Strongly concave obstacles are probed orienting a few waves around the cavity opening.

	number of waves	direction angles
example 1	3	$\pi/4, \pi, 7\pi/4$
example 2	4	$\pi/4, \pi, 7\pi/4, 0$
example 3	4	$\pi/4, \pi, 7\pi/4, 0$
example 4	4	$\pi/4, \pi, 7\pi/4, 0$
example 5	4	$\pi/4, \pi, 7\pi/4, 0$

4.3 Non-convex Obstacles

Examples in this section focus on obstacles having a concavity comparable to the size of the obstacle itself. Obstacles are probed orienting a few waves around the obstacle cavity opening. This is done so for the sake of illustrating the method of continuation at work; no extra information about the obstacle boundary is necessarily known a priori. Obstacle boundaries are reconstructed within two significant digits.

In all examples the regularization cutoff value is 10^{-1}, except in example **2** where the cutoff value is $8 * 10^{-2}$; in all examples the wavenumber step-size is 1 and the stopping condition is: the relative residual $Res < 10^{-3}$ or the wavenumber $k \geq 30$; the initial curve is the unit circle centered at the origin. In table 4.2 the number of waves and the direction angles used in each case are shown.

4.3.1 Example 1

Three waves per iteration are used to probe the object depicted in figure 4.27, one has direction $(1, 0)$ and the other two are oriented around the cavity opening with directions $(-1/\sqrt{2}, 1/\sqrt{2})$ and $(-1/\sqrt{2}, -1/\sqrt{2})$. In figure 4.28 are shown the approximated curves corresponding to the first four iterations; in the first plot the circle that serves as initial curve is also shown. Notice that the outer side of the curve has been almost reconstructed by the fourth iteration. In figures 4.29 to 4.32 it is shown the transition from the interval where the wavelength is greater than the obstacle cavity opening to the interval where the wavelength is smaller. In figure 4.32 the approximated boundary curve is already close to the obstacle boundary. In figure 4.36 the initial curve, the obstacle boundary curve and the best approximation achieved are depicted. The relative residual decrease below $\epsilon = 10^{-3}$ when the wavenumber is $k = 19.625$, see figure 4.37. Although the obstacle used in this example has a big concavity we can say that this is not a very complicated curve. In this example plots of all iterations required to reconstruct the obstacle boundary are shown.

Figure 4.27: Target boundary curve probed in example 1.

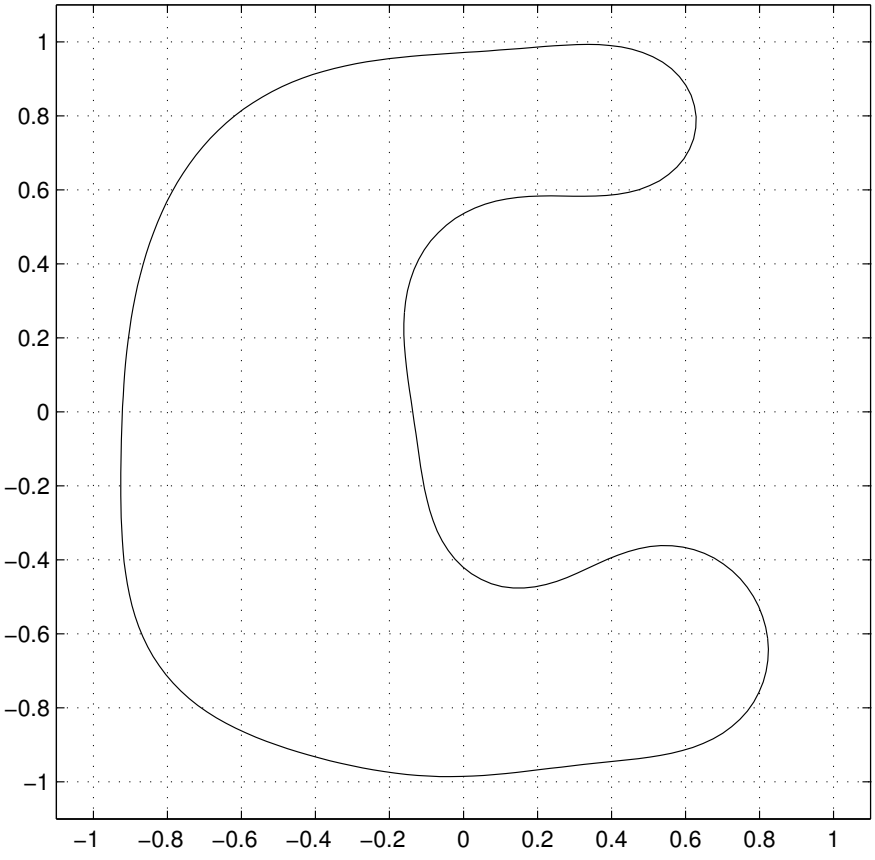

Figure 4.28: Smaller wavenumber step-sizes are required as the wavelength of incoming waves becomes comparable to the obstacle cavity opening.

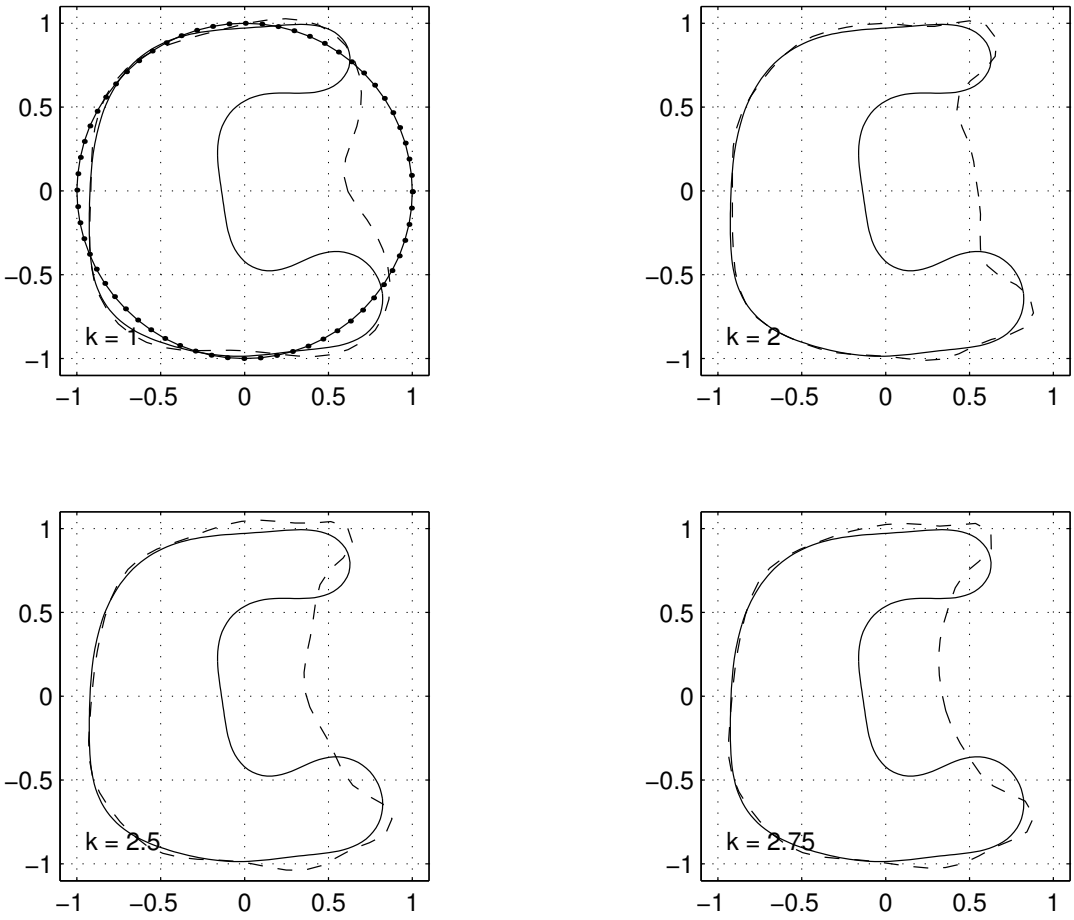

Figure 4.29: This and the next figure include iterations that correspond to the transition from the interval where the wavelength is greater than the obstacle cavity opening to the interval where the wavelength is smaller.

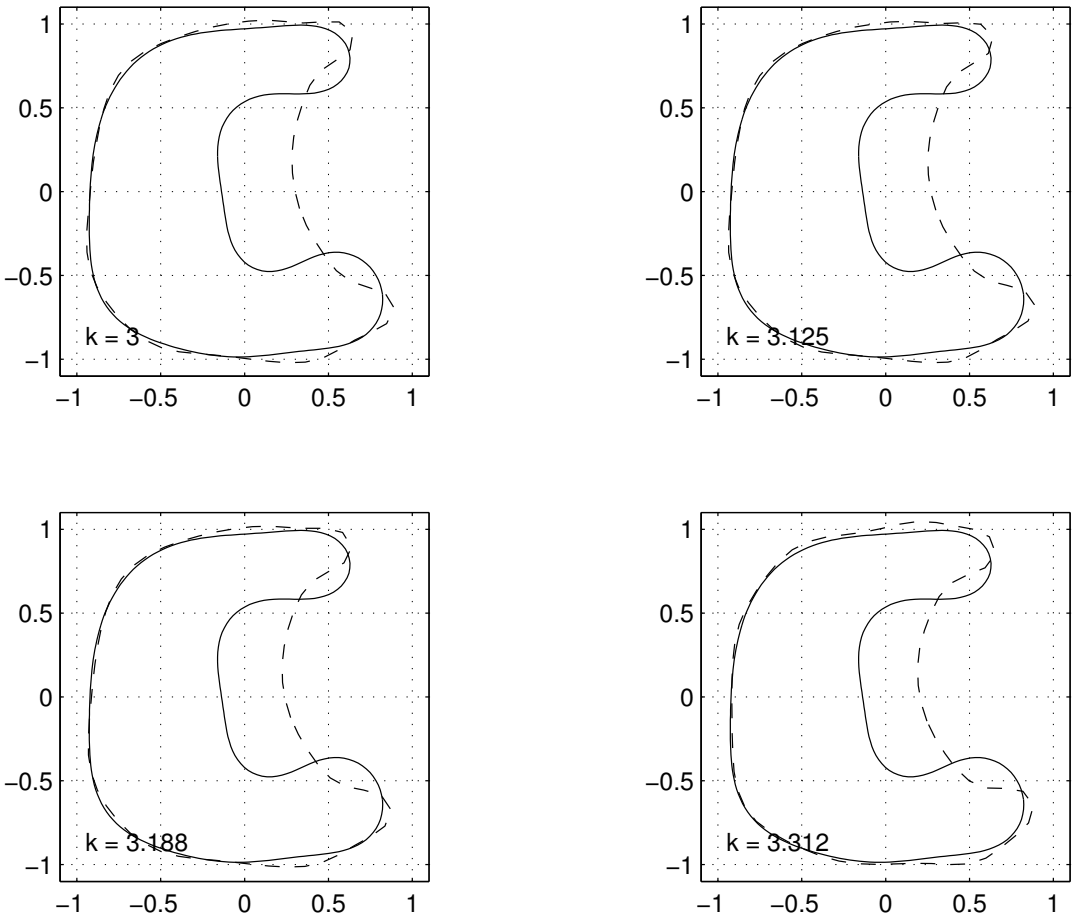

Figure 4.30: When the wavelength is smaller than the cavity opening the approximated boundary curve approaches also the inner side of the obstacle boundary.

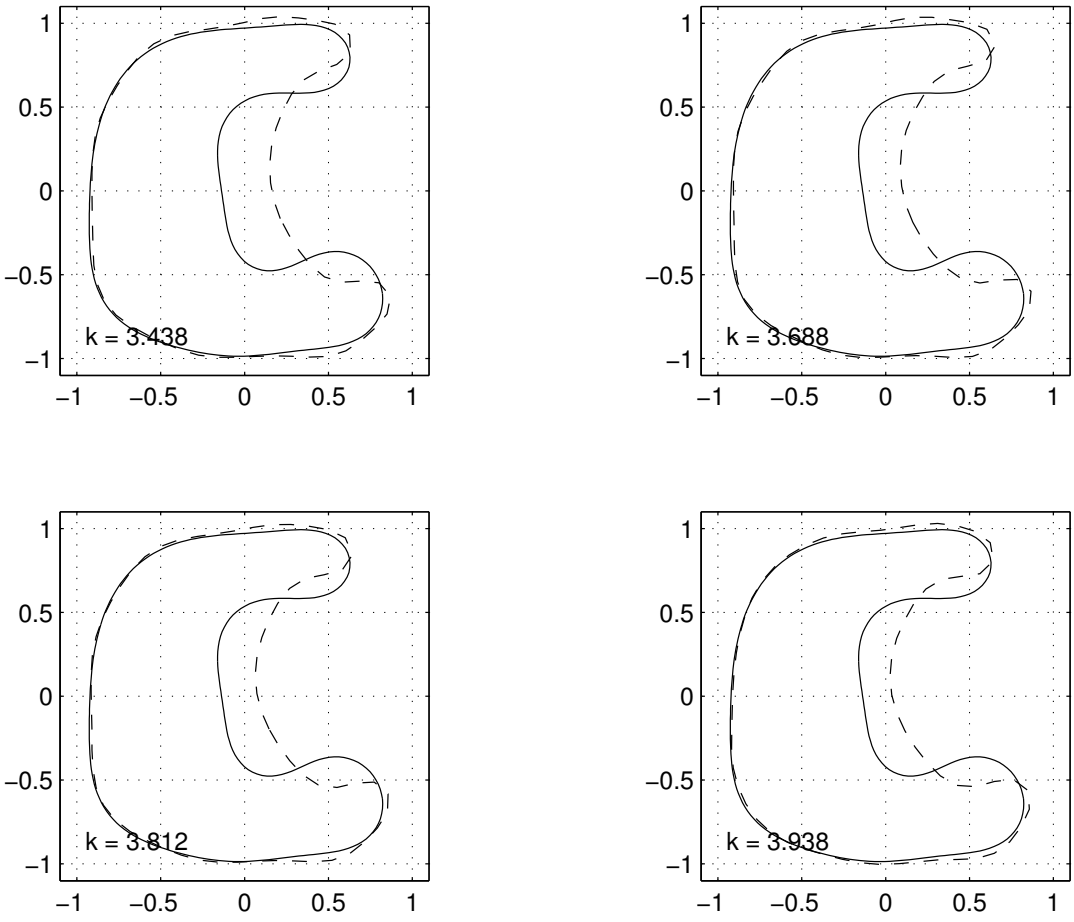

Figure 4.31: Iterations with a greater wavenumber reconstruct the fine details of the obstacle boundary.

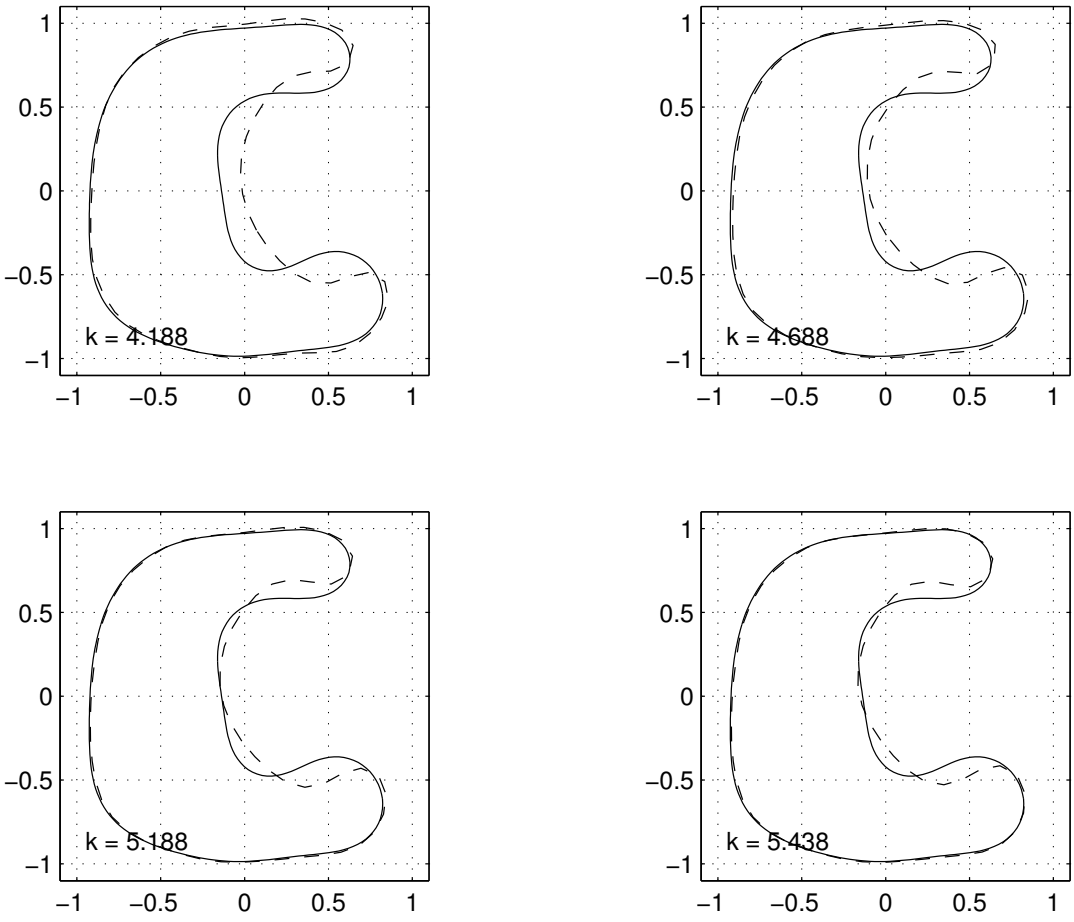

Figure 4.32: In the iterations presented in this figure, the approximated boundary curve is already close to the obstacle boundary.

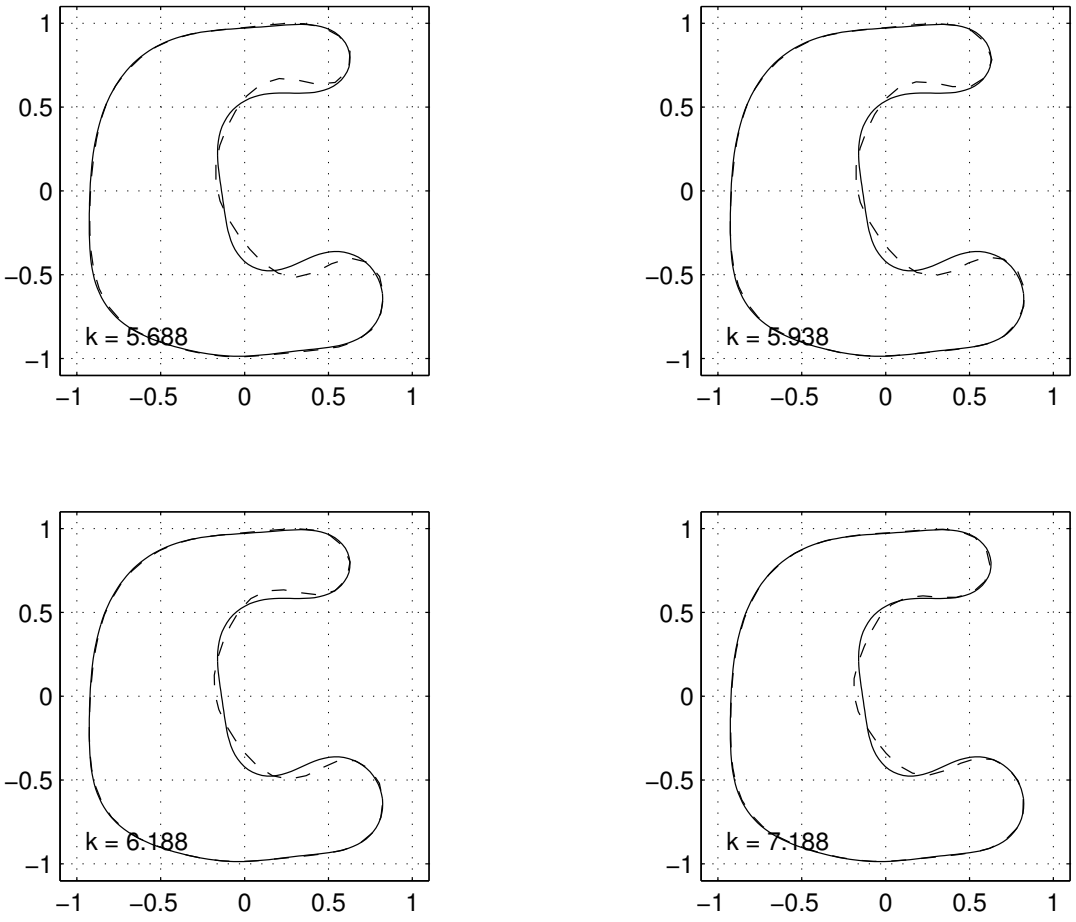

Figure 4.33: In the iterations presented in this figure, the approximated boundary curve is almost completely reconstructed.

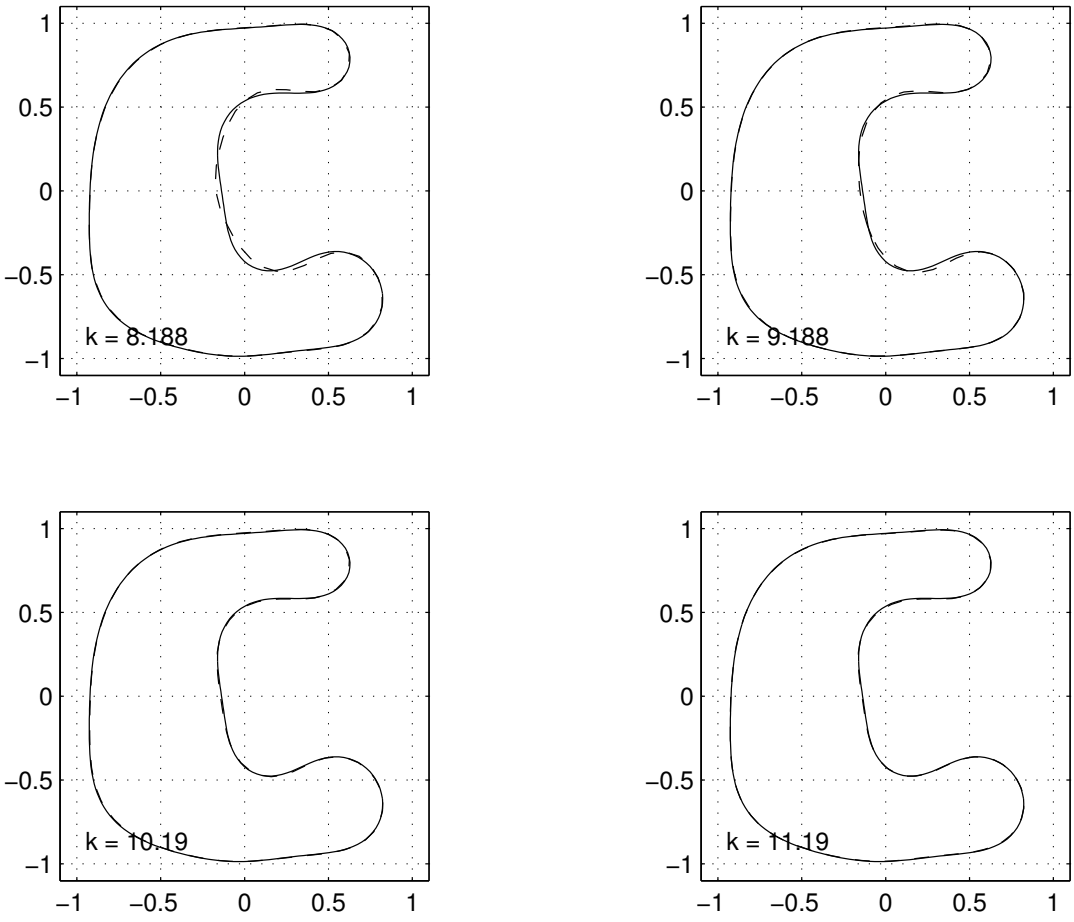

Figure 4.34: Relative changes between consecutive iterations are tiny when the stopping condition is close to being met.

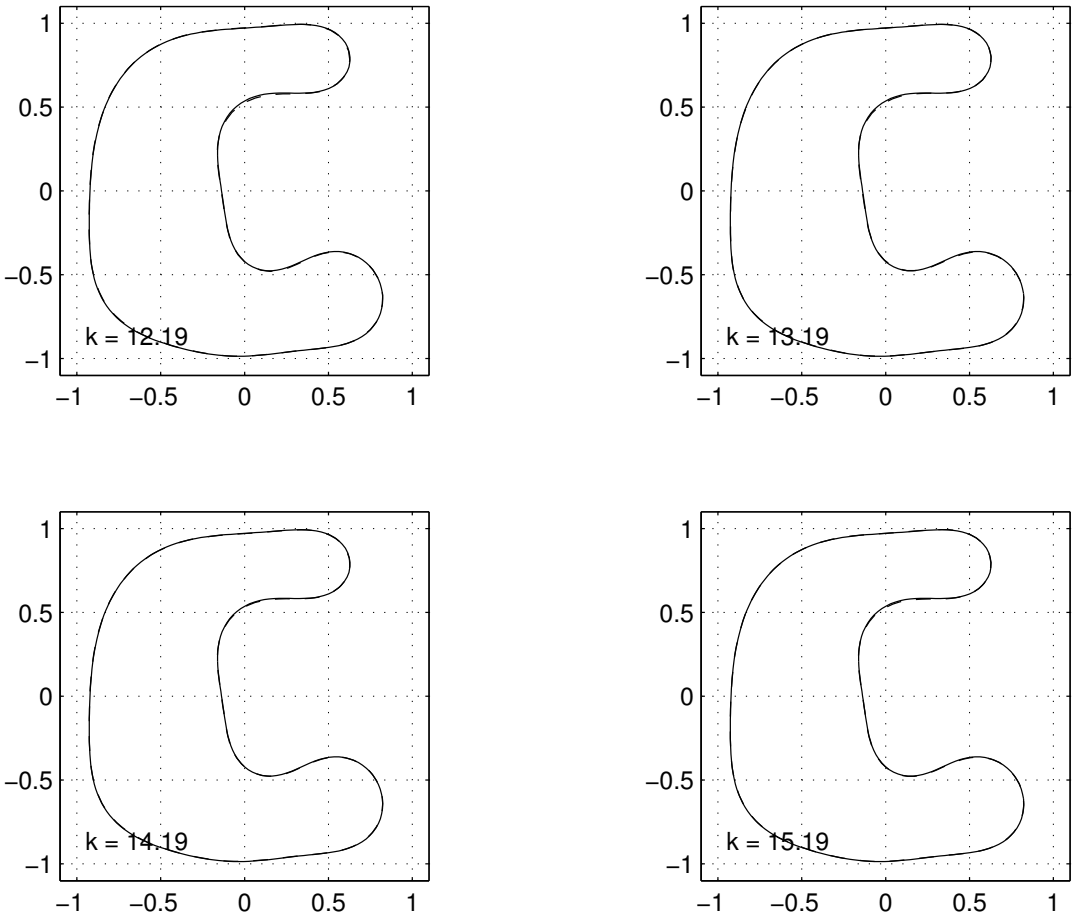

Figure 4.35: The final iterations of the approximation are depicted in this figure.

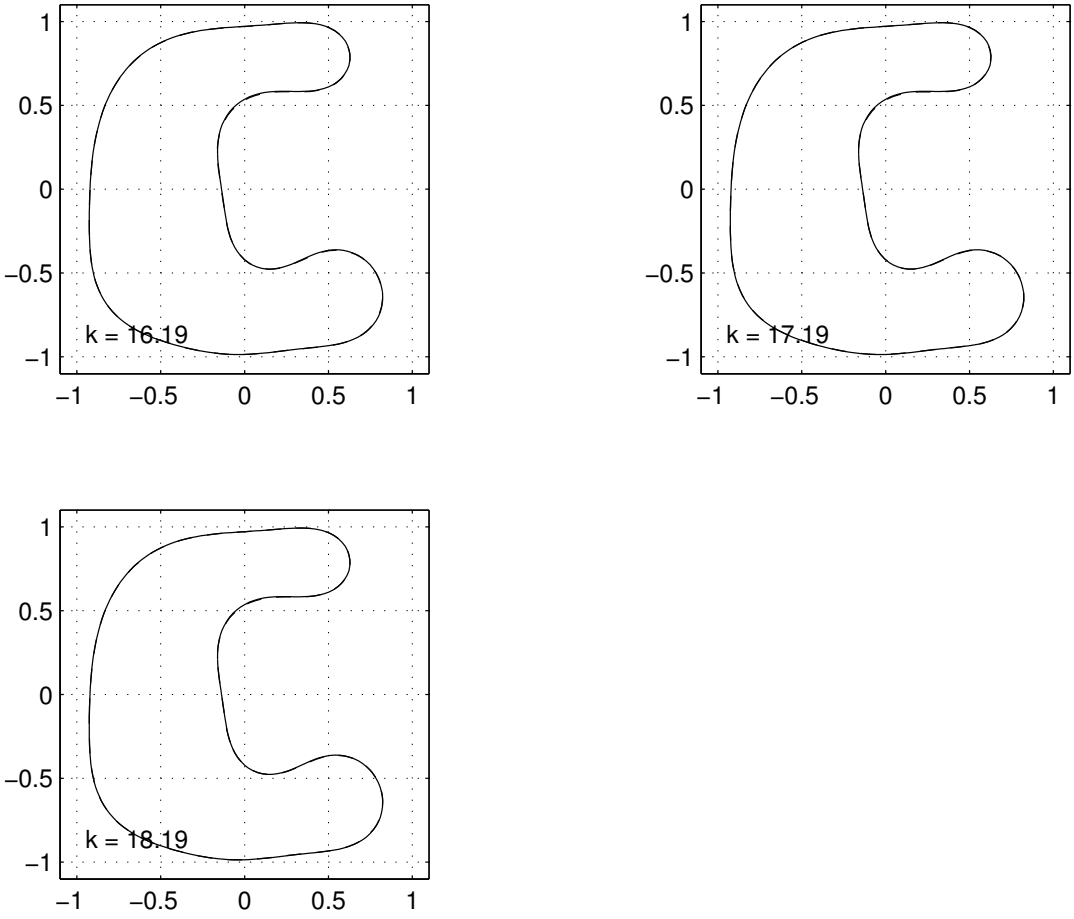

Figure 4.36: This figure depicts the initial curve, the obstacle boundary curve and the best approximation achieved. The obstacle boundary is reconstructed within two significant digits.

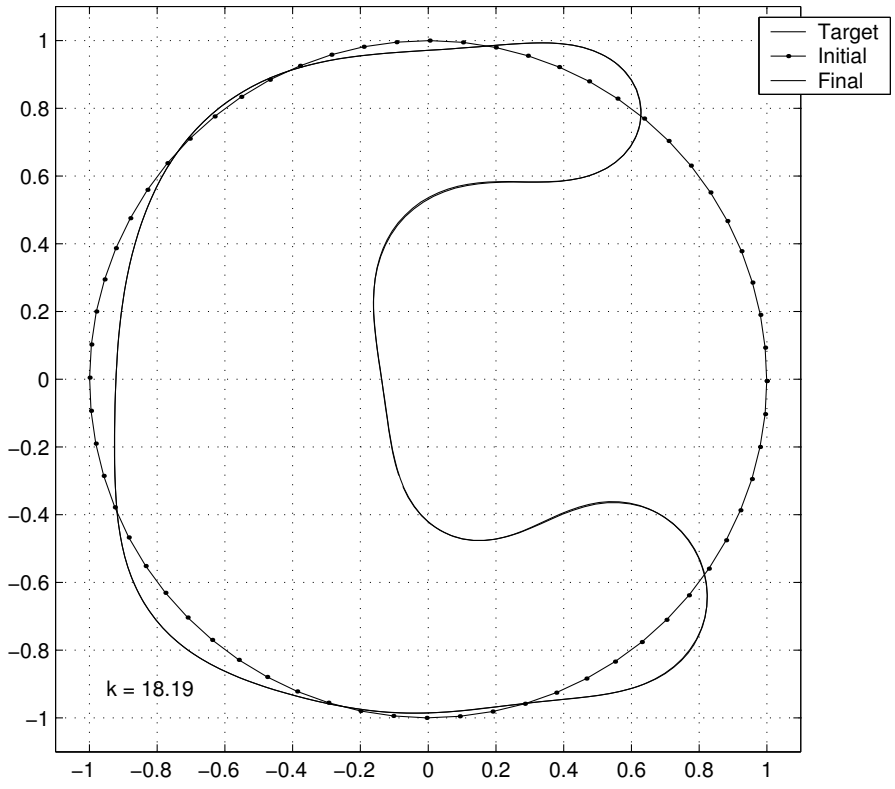

Figure 4.37: The relative residual as a function of wavenumber. The relative residual becomes smaller than $\epsilon = 10^{-3}$ at $k = 18.19625$.

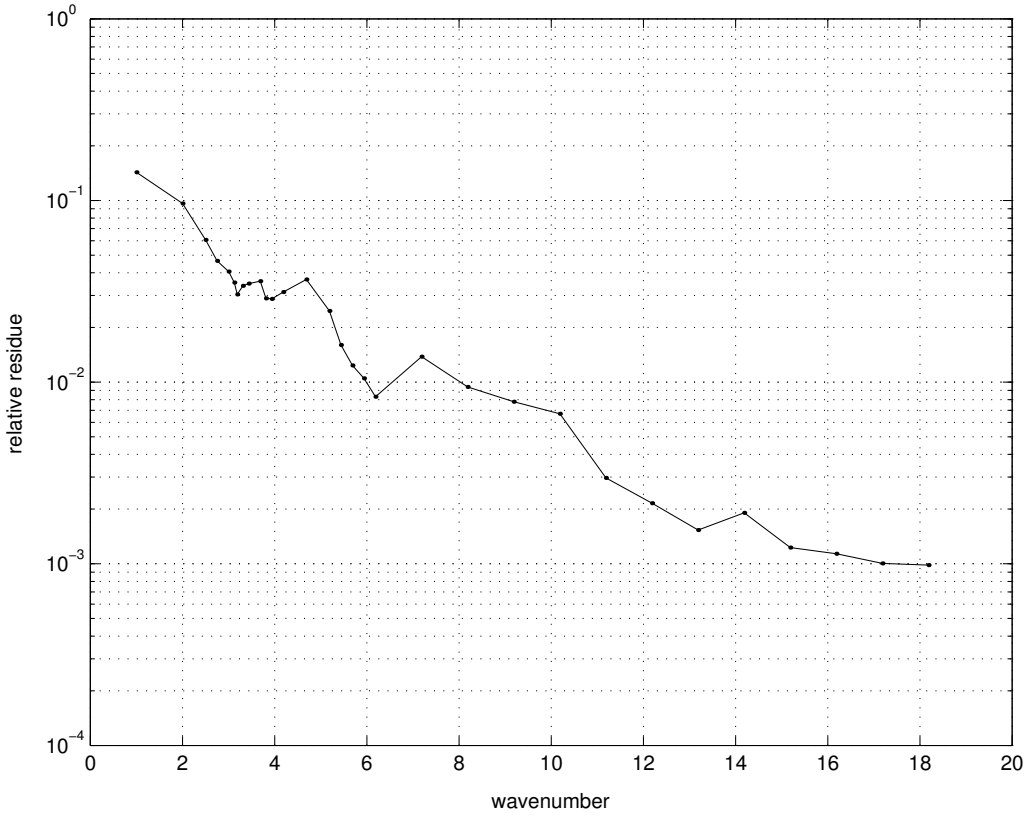

4.3.2 Example 2

This time the target boundary curve is the domain depicted in figure 4.38. To probe this figure and those considered in the remaining examples are used four incoming waves per iteration, one has direction $(1, 0)$ and the other three are oriented around the cavity opening with directions $(-1/\sqrt{2}, 1/\sqrt{2})$, $(-1, 0)$ and $(-1/\sqrt{2}, -1/\sqrt{2})$. Notice that the opening of the obstacle cavity is smaller than the cavity inner part. This figure may be regarded as difficult to reconstruct. Figures 4.39 and 4.41 represent the change from the interval where the wavelength of the incoming waves is greater than the cavity opening to the interval where the wavelength is smaller. In the iterations shown in figure 4.42 the obstacle is finally reconstructed. In this experiment the relative residual does not decrease below 10^{-3} in the chosen wavenumber interval, see figure 4.44.

Figure 4.38: Boundary curve probed in example 2. This figure may be regarded as difficult to reconstruct since the cavity inner part is bigger than the cavity opening.

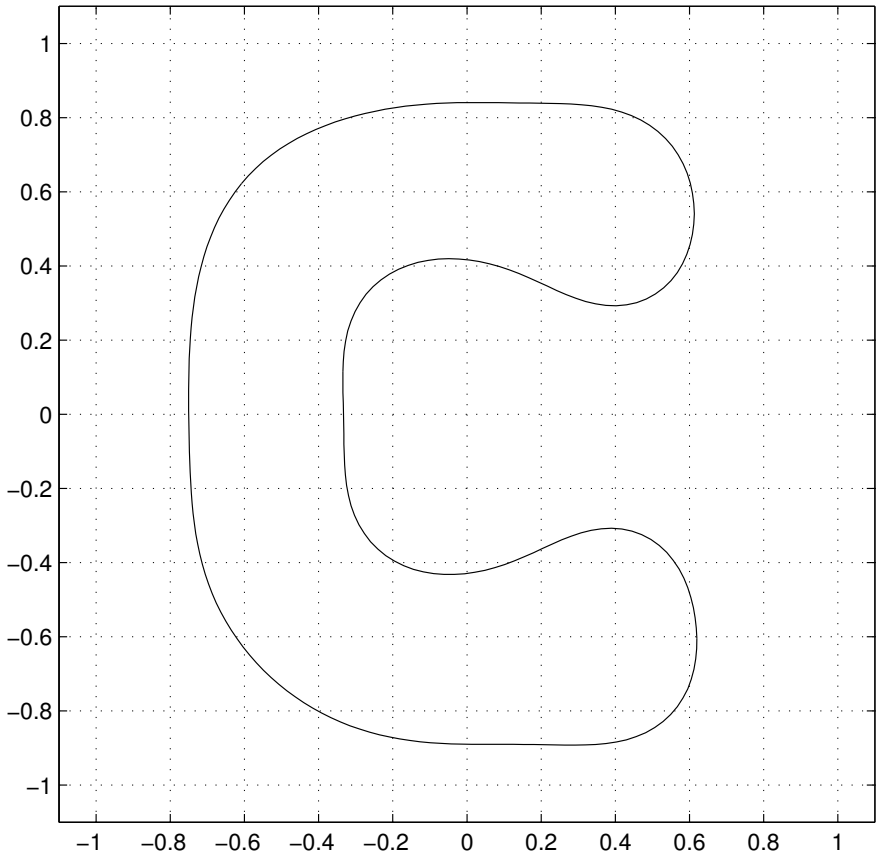

Figure 4.39: It is not necessary to take smaller wavenumber step-sizes until the semi-wavelength is comparable to the cavity opening.

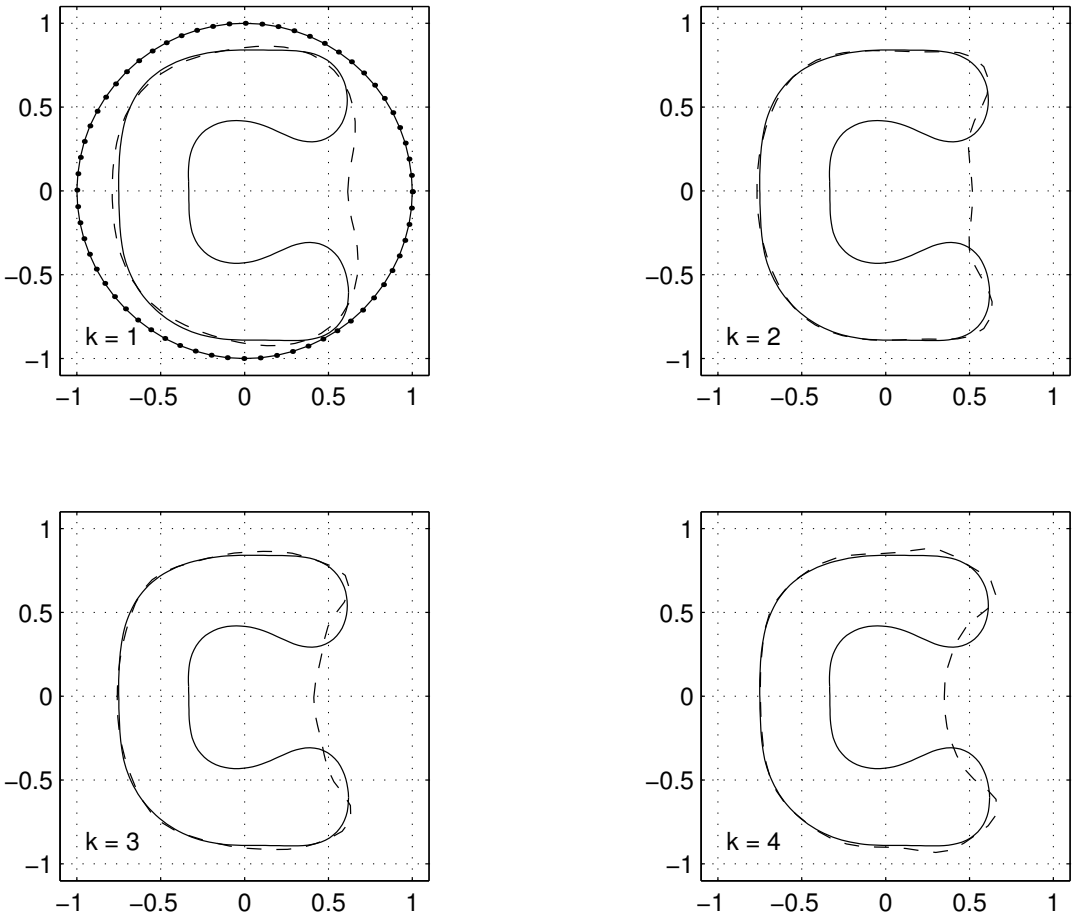

Figure 4.40: When the semi-wavelength is about the same size of the cavity opening the approximated boundary curve starts approaching the inner side of the boundary curve.

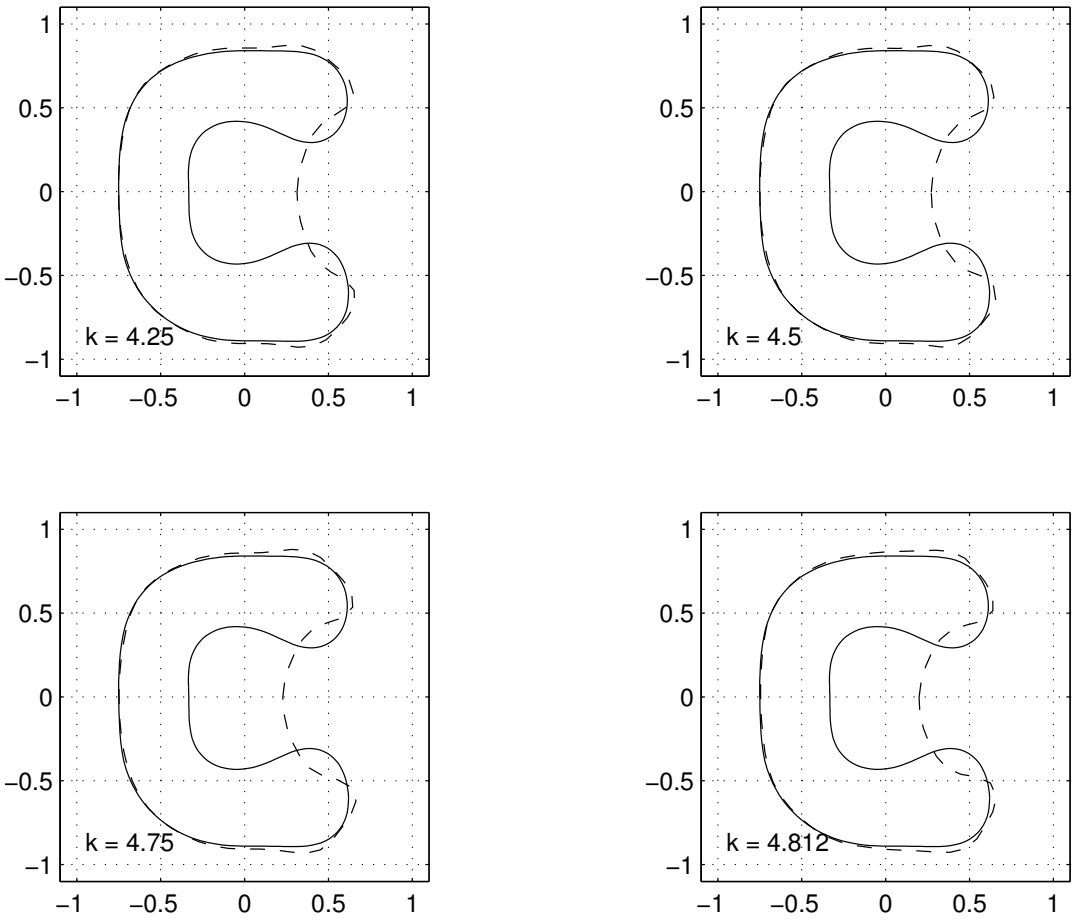

Figure 4.41: Iterations in this figure represent the transition from the interval where the wavelength of incoming waves is greater than the cavity opening to the interval where the wavelength is smaller.

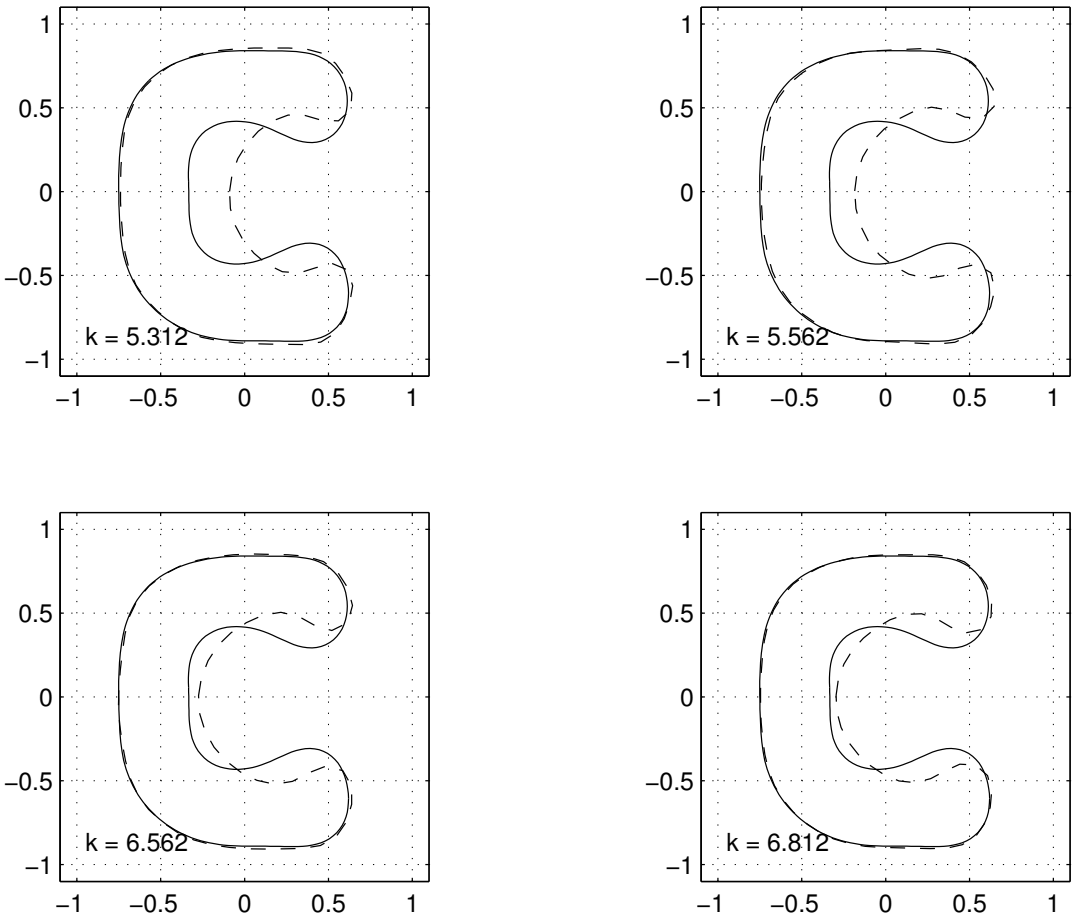

Figure 4.42: In iterations shown in this figure the obstacle is already reconstructed.

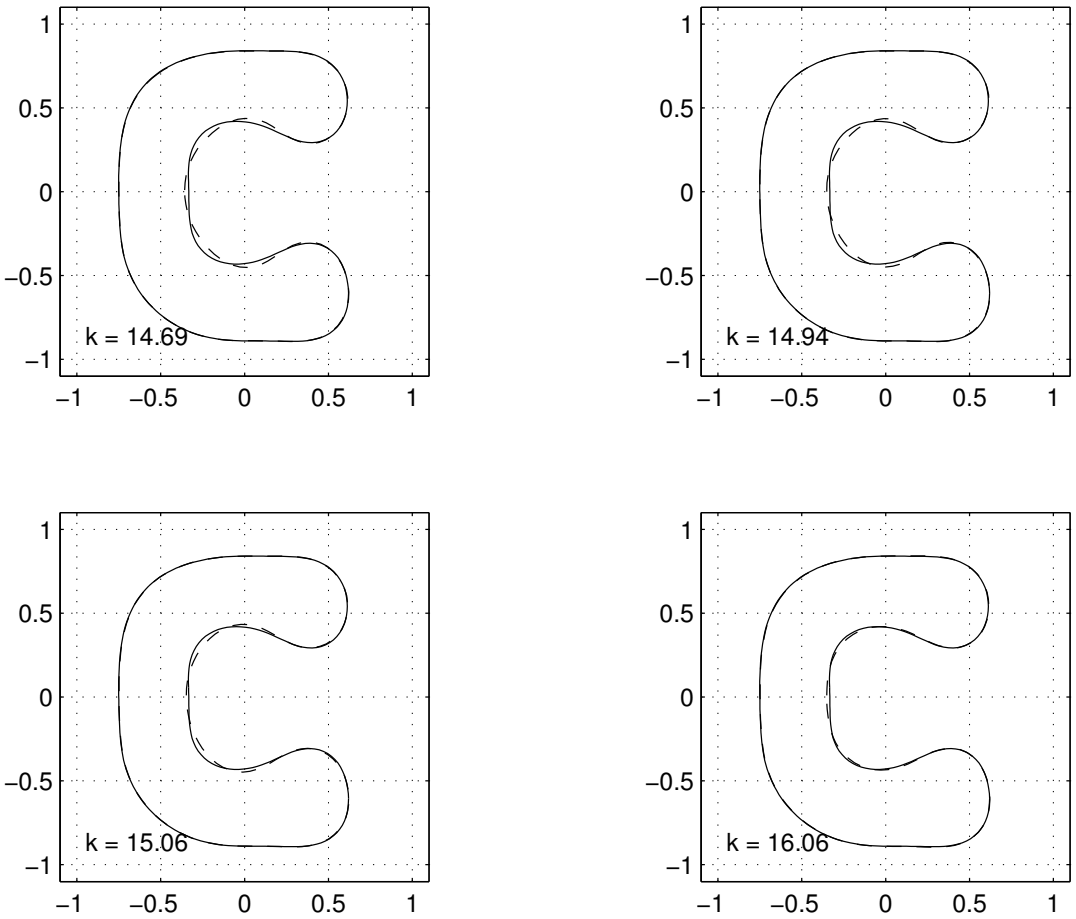

Figure 4.43: This figure depicts the initial curve, the obstacle boundary curve and the best approximation achieved as indicated in the legend in the figure.

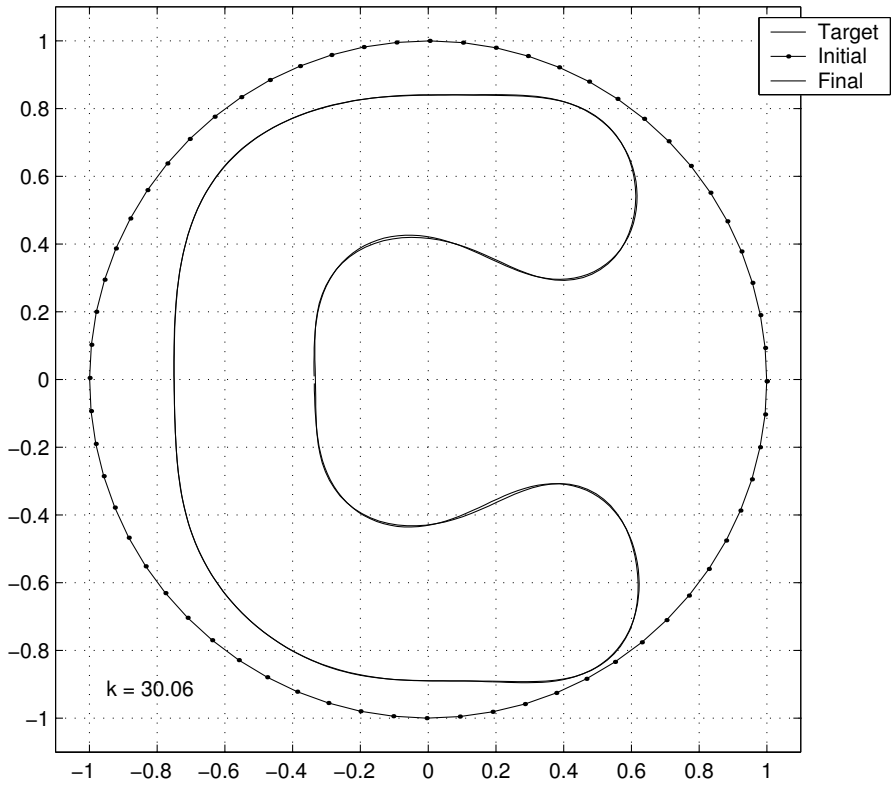

Figure 4.44: The relative residual does not decrease below 10^{-3} in the chosen interval. However, the boundary curve is reconstructed within to significant digits.

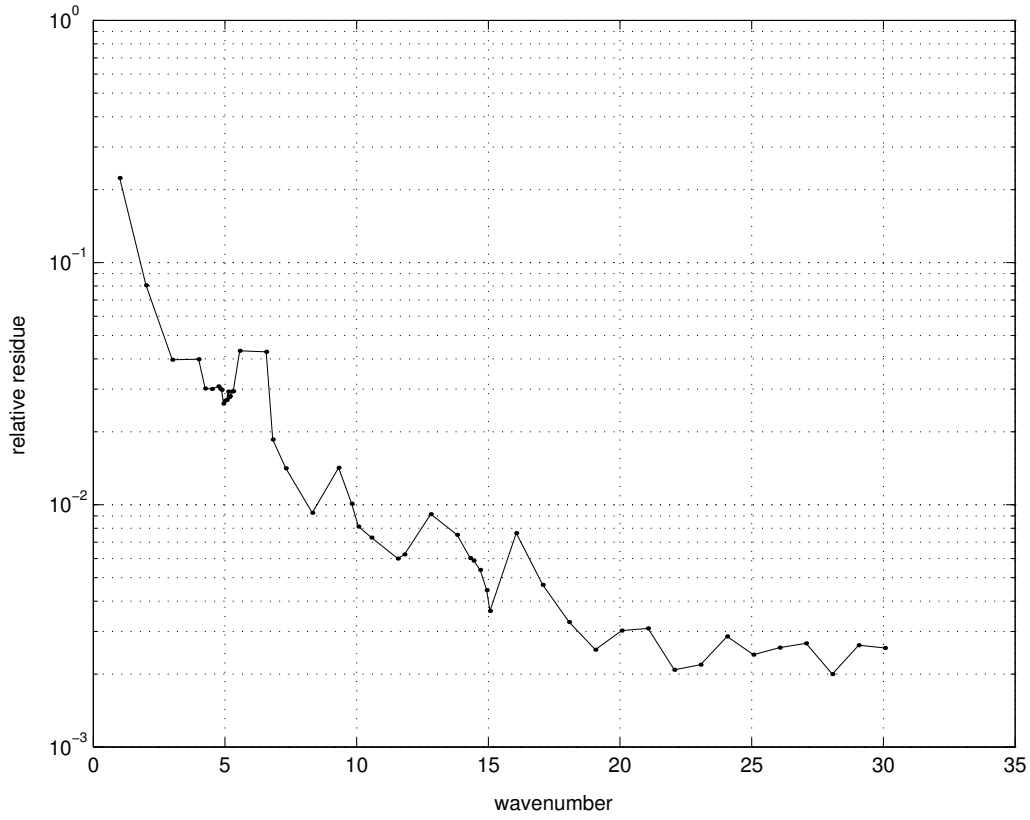

4.3.3 Example 3

For this example a more complicated boundary curve is chosen, see figure 4.45. This boundary curve and those considered in examples **4** and **5** are alike, except that the the legs that form the obstacle cavity are more curved in the later two cases. When the semi-wavelength is about the same size of the cavity opening the approximated boundary curve starts approaching the inner part of the obstacle boundary curve, see figure 4.48. In figure 4.50 the initial curve, the target curve and the best approximation achieved are shown.

Figure 4.45: Boundary curve probed in example 3. The aspect ratio of this obstacle is bigger compared to the two previous examples.

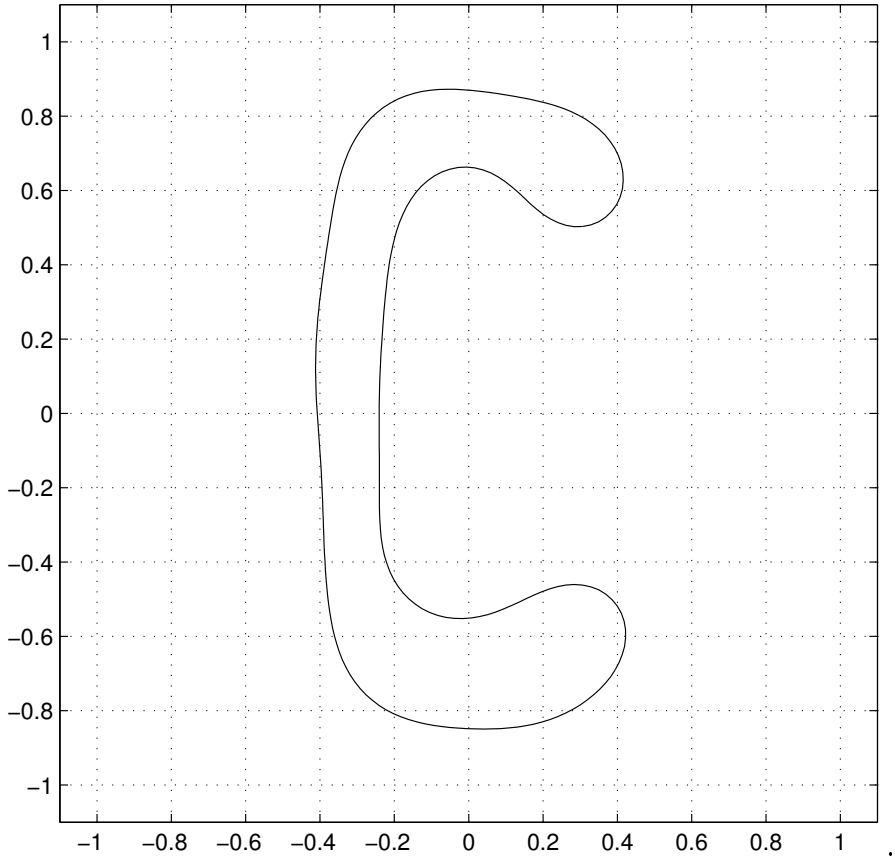

Figure 4.46: In the first iterations the approximated boundary curve approaches the outer side of the obstacle boundary curve.

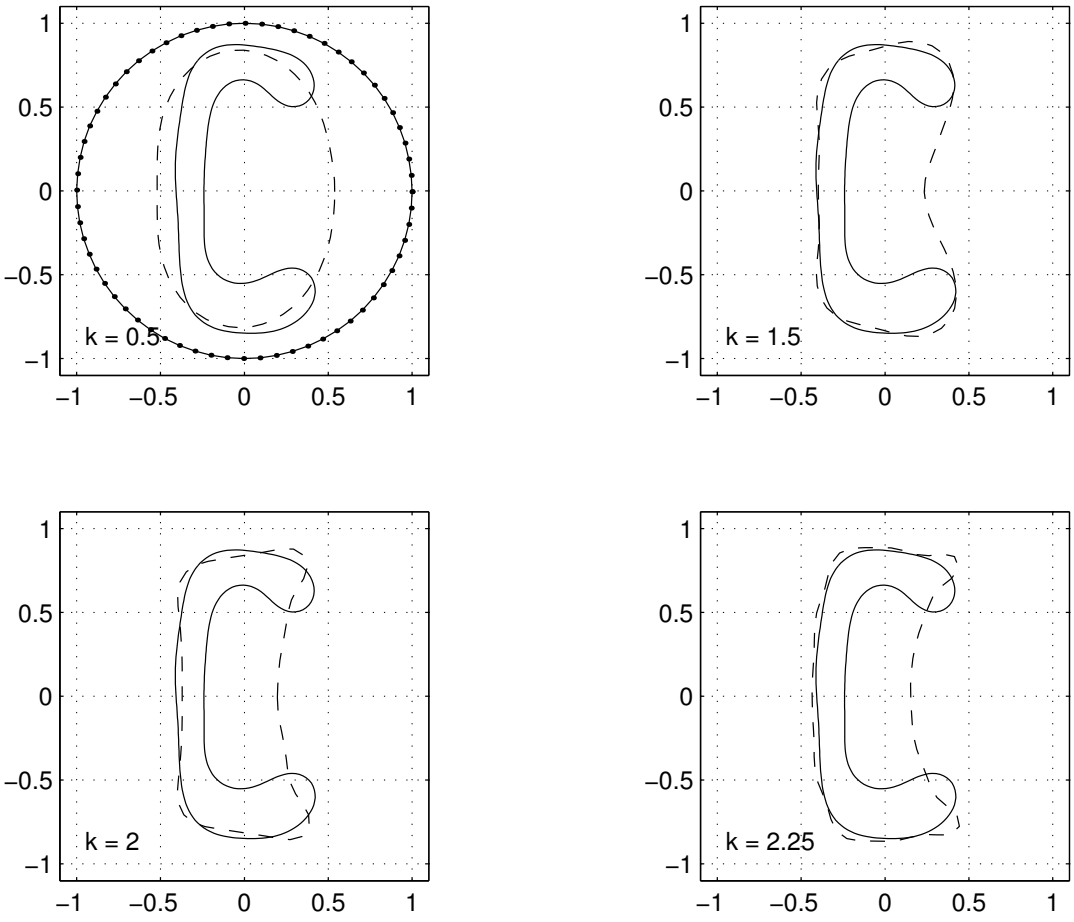

Figure 4.47: When the semi-wavelength is about the same size of the cavity opening the approximated boundary curve starts approaching the boundary curve inner part.

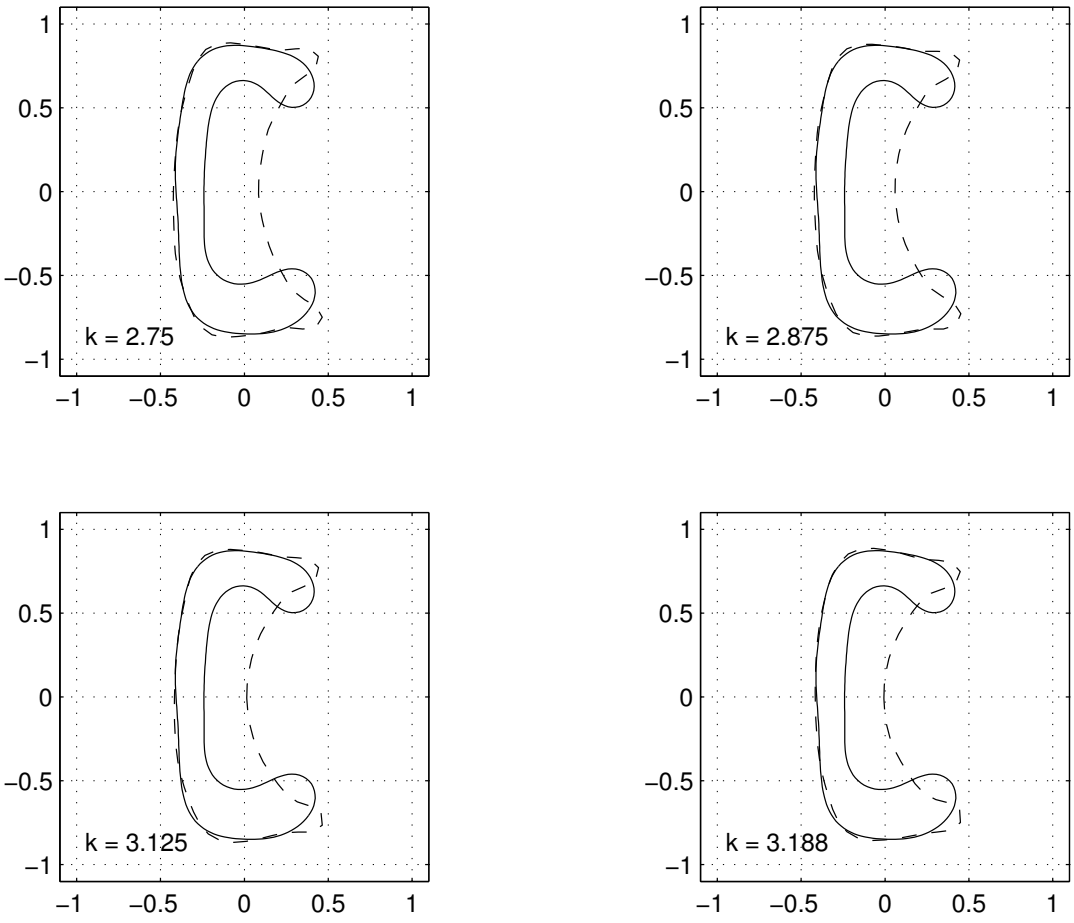

Figure 4.48: When the semi-wavelength is small enough the details of the boundary inner part are reconstructed.

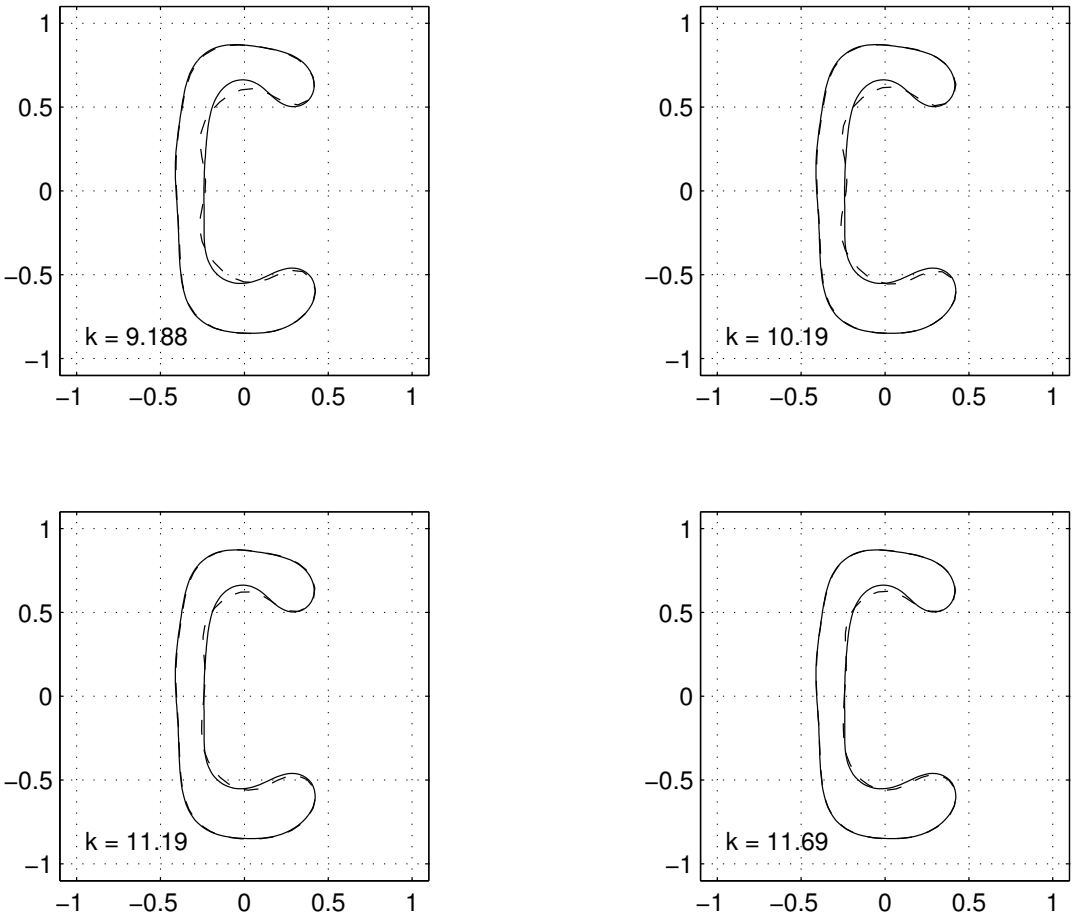

Figure 4.49: In the iterations shown in this figure, the reconstruction of the boundary curve is almost complete.

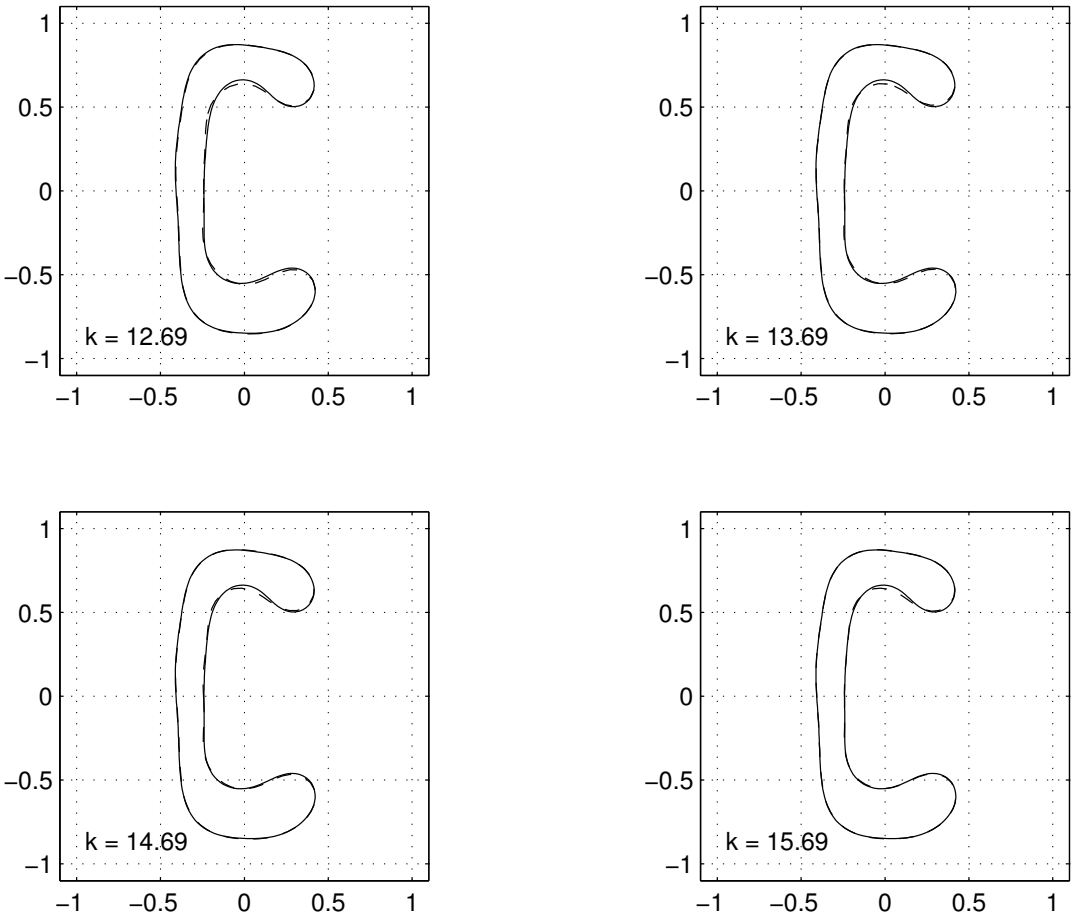

Figure 4.50: The domain considered in this example is also reconstructed within two significant digits.

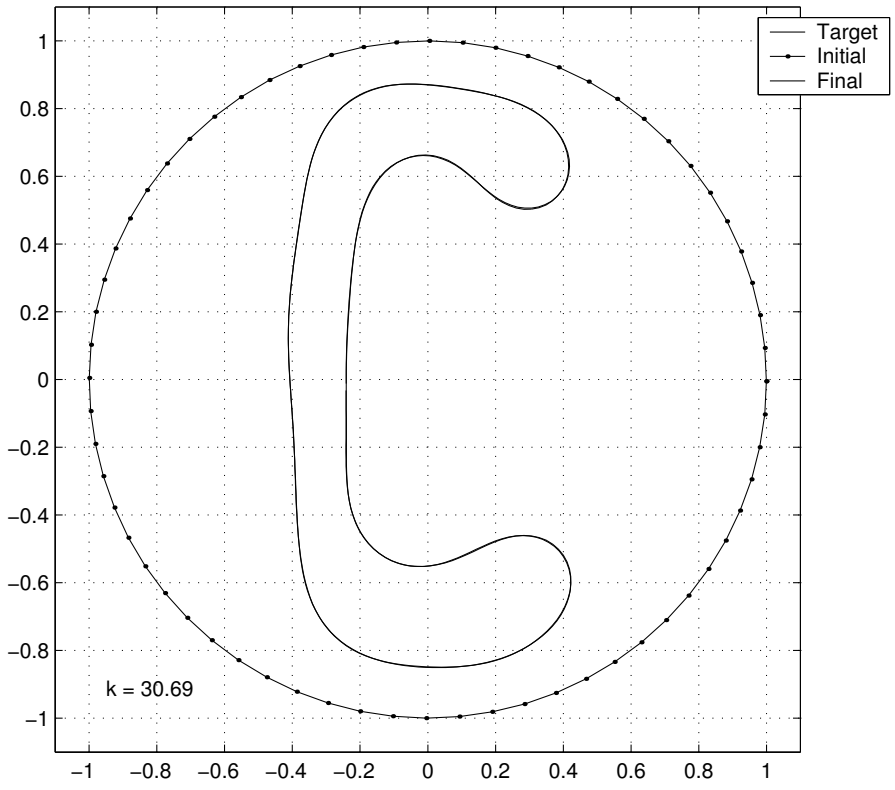

Figure 4.51: The relative residual does not decrease below 10^{-3} in the chosen wavenumber interval. But the obstacle is reconstructed within two significant digits.

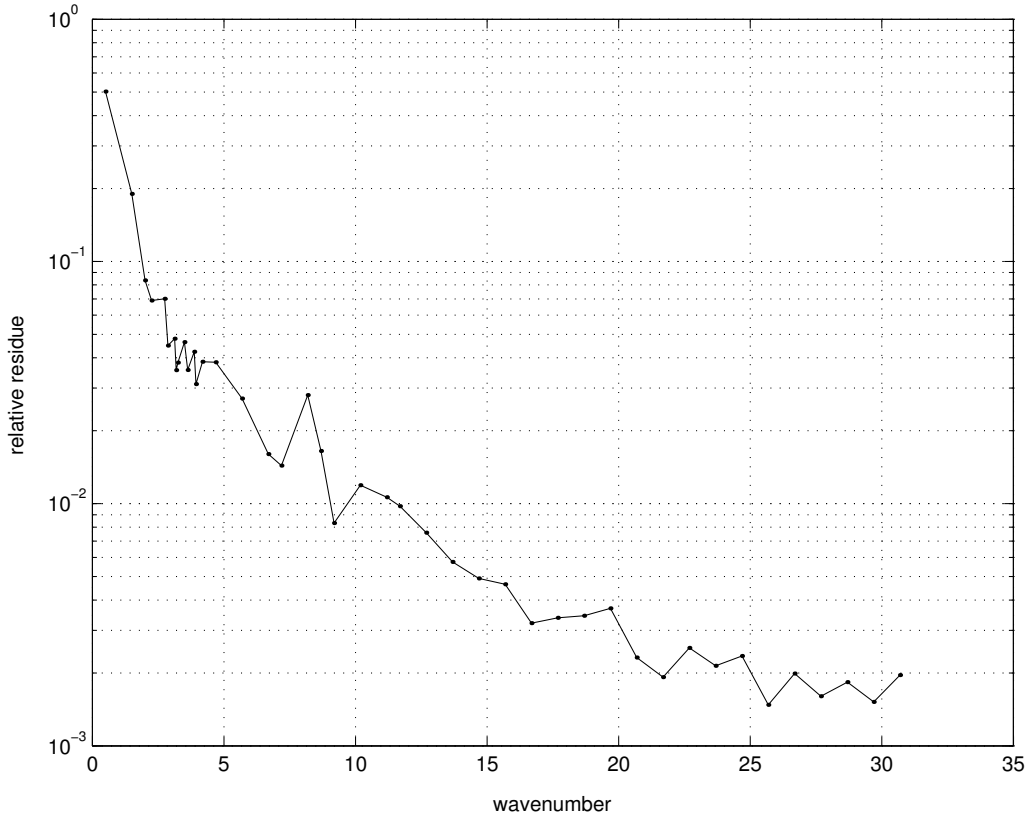

4.3.4 Example 4

In this examples is probed the figure depicted in figure 4.52. This boundary curve is alike the curve considered in the previous example, except that in the current case the inner part of the curve boundary is slightly bigger than the cavity opening. As expected, in the first iterations the approximated boundary curve approaches the outer side of the obstacle boundary curve, see figure 4.53, and the approximated boundary curve starts approaching the inner part of the obstacle boundary curve, see figure 4.55 when the semi-wavelength is about the same size of the cavity opening. In figure 4.57 are the initial curve, the target curve and the best approximation achieved.

Figure 4.52: Boundary curve probed in example 4. This obstacle is alike the one used in example 3, except that the obstacle in the current example has a smaller cavity opening.

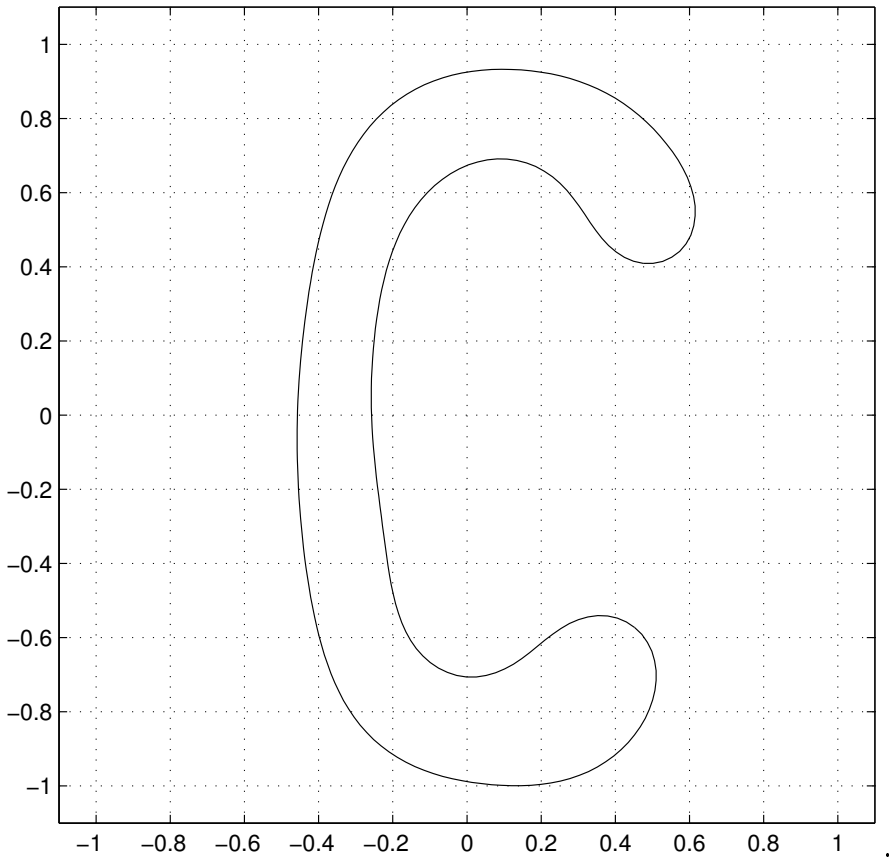

Figure 4.53: In the first iterations the approximated boundary curve approaches the outer side of the obstacle boundary curve.

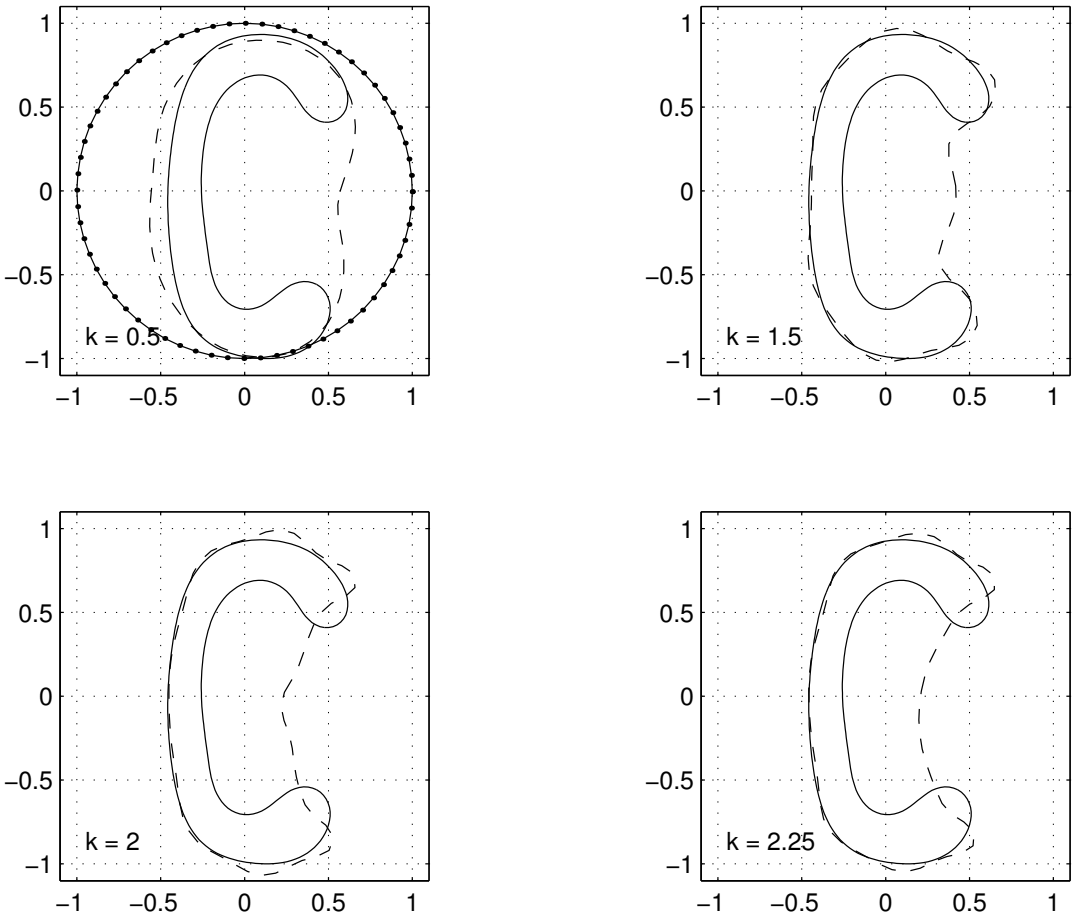

Figure 4.54: When the semi-wavelength is about the same size of the outer opening the approximated boundary curve starts approaching the cavity inner part.

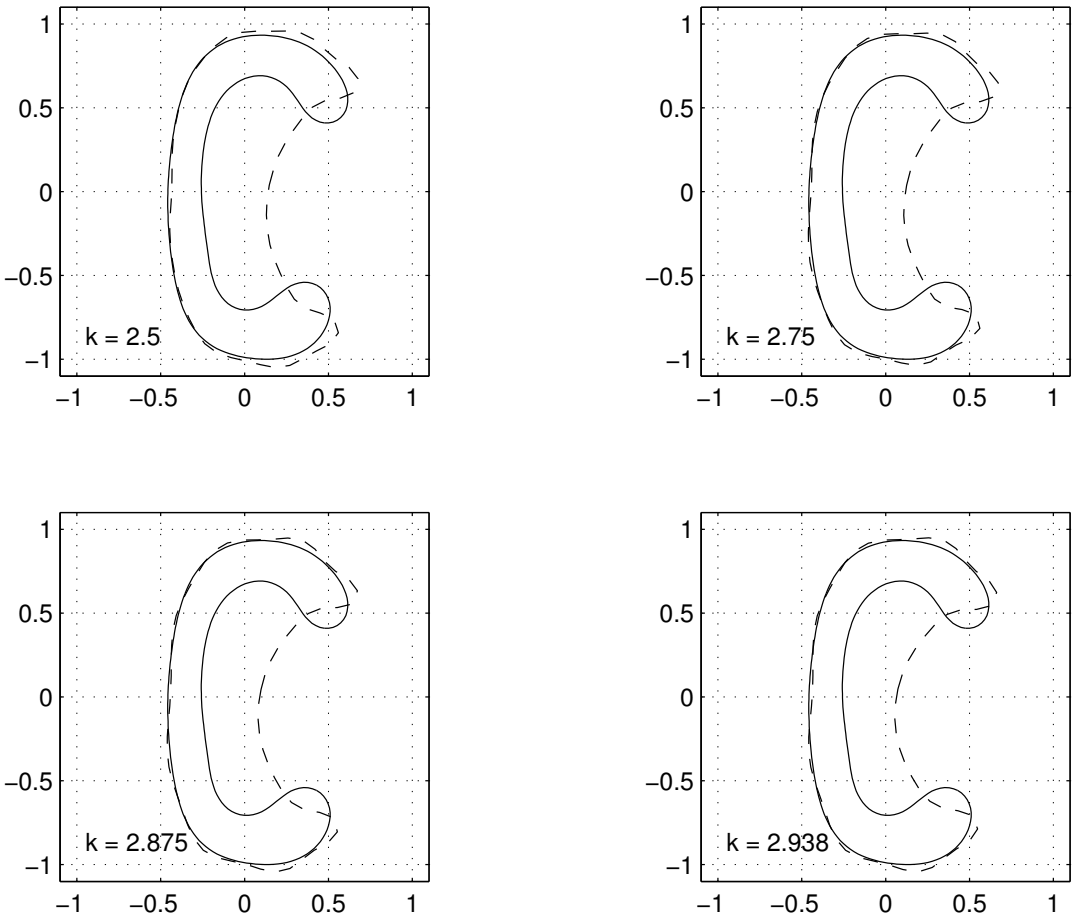

Figure 4.55: When the semi-wavelength is small enough the inner part of the boundary curve is reconstructed.

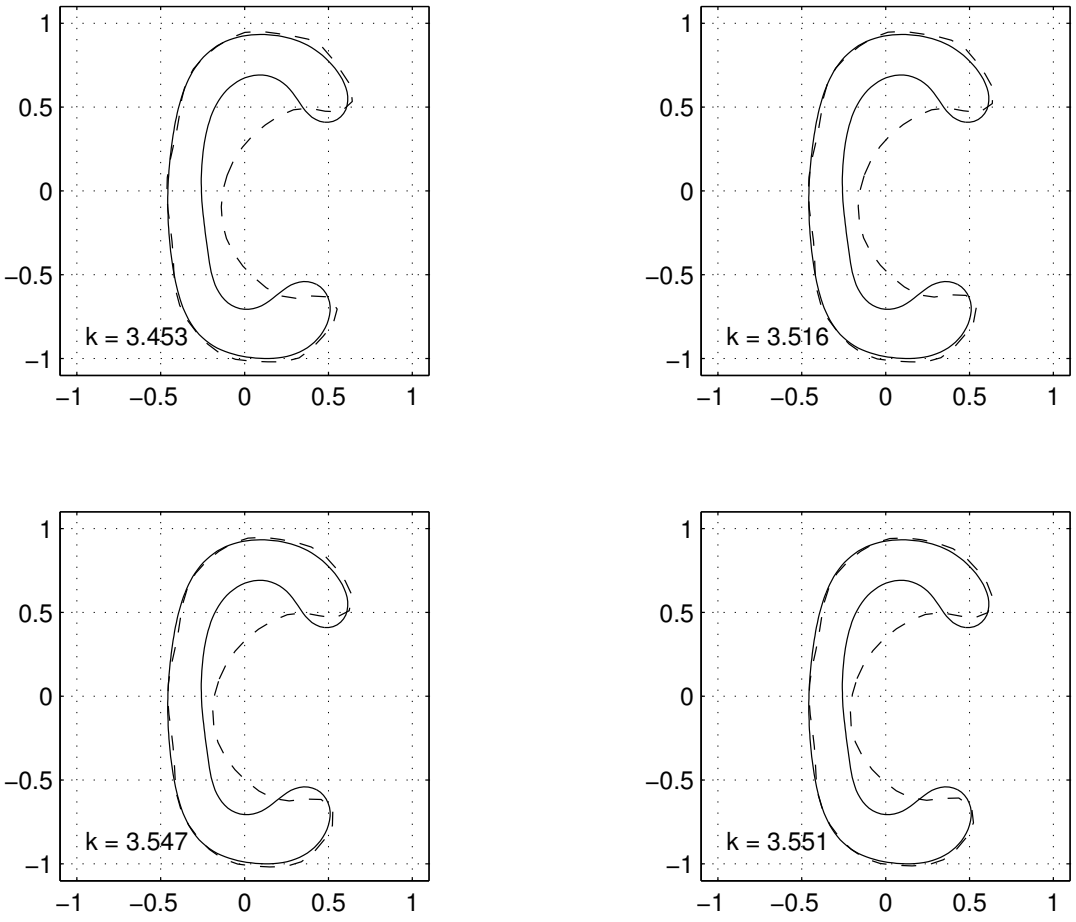

Figure 4.56: When the reconstruction is nearly complete the relative changes between consecutive approximated curves are tiny.

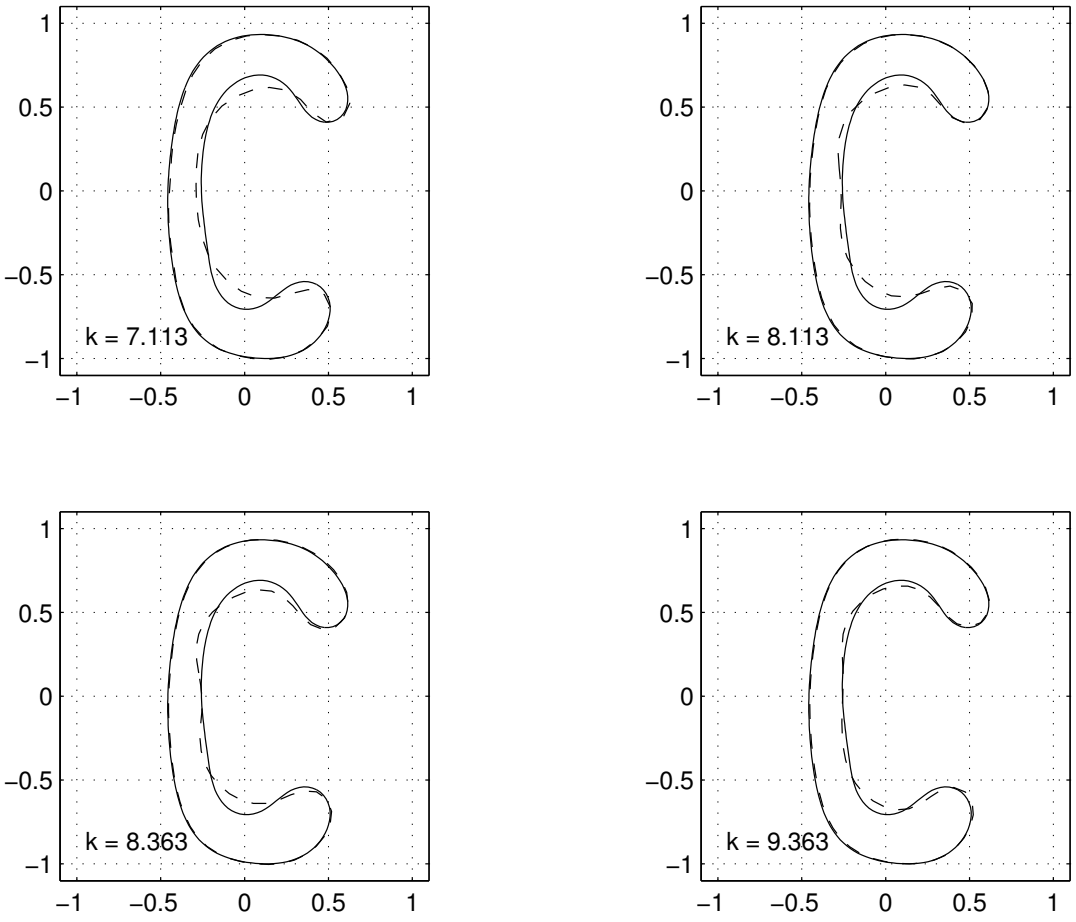

Figure 4.57: The domain chosen for this example is also reconstructed within two significant digits.

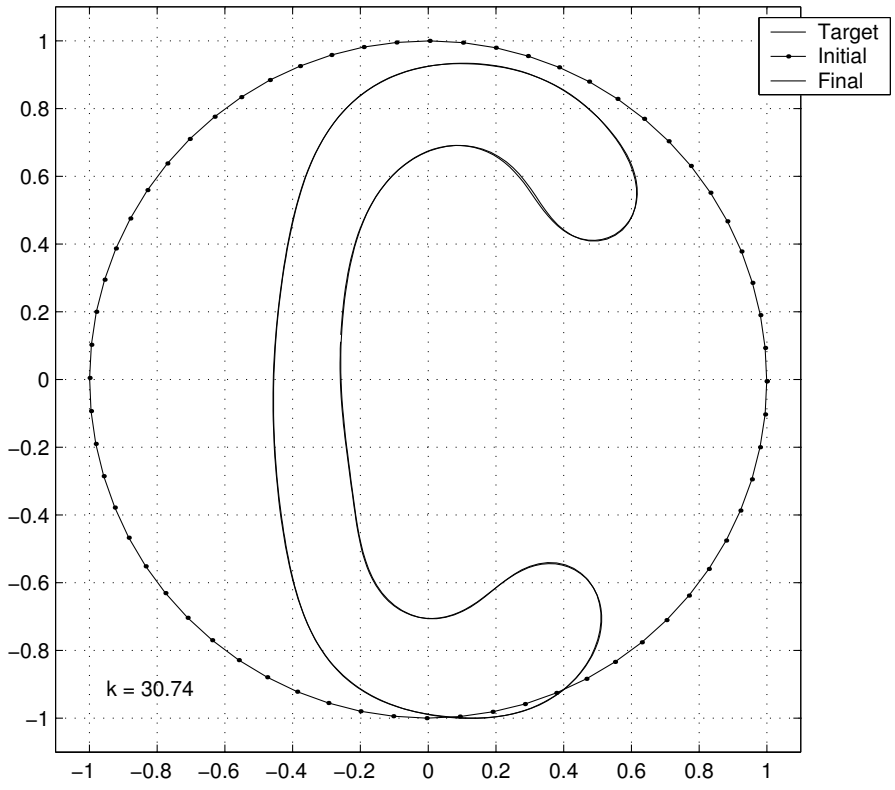

Figure 4.58: The relative residual does not decrease below 10^{-3} in the chosen wavenumber interval. But the obstacle is reconstructed within two significant digits.

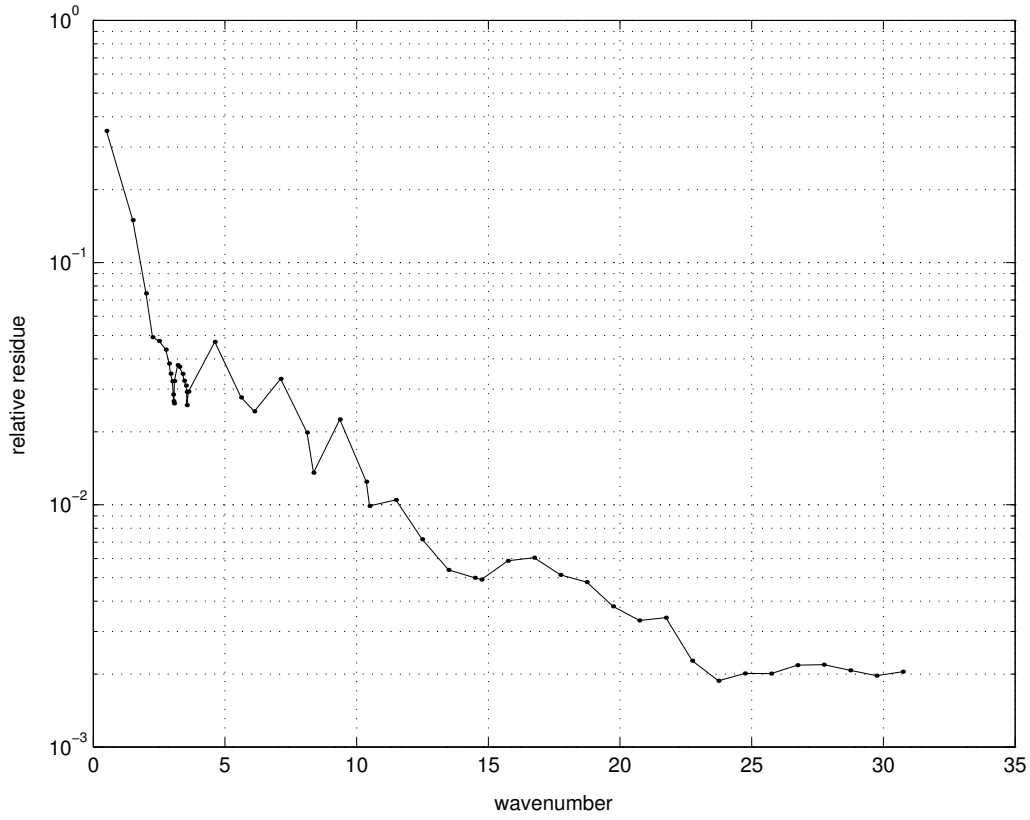

4.3.5 Example 5

For this final example a more complicated boundary curve is chosen, see figure 4.59. As in previous examples the obstacle boundary curve is reconstructed within two significant digits. In figure 4.64 are the initial curve, the target curve and the best approximation achieved.

Figure 4.59: Boundary curve probed in example 5. In this final example we have slightly modified the obstacle shape used in the two previous examples.

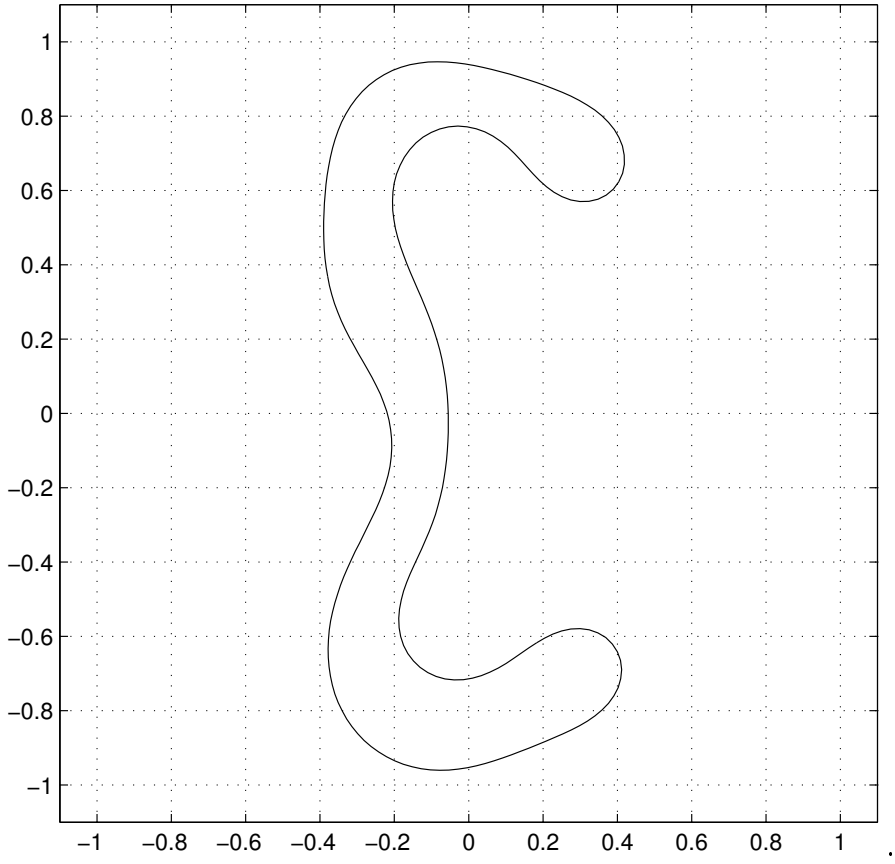

Figure 4.60: In the first iterations the approximated boundary curve approaches the outer side of the obstacle boundary curve.

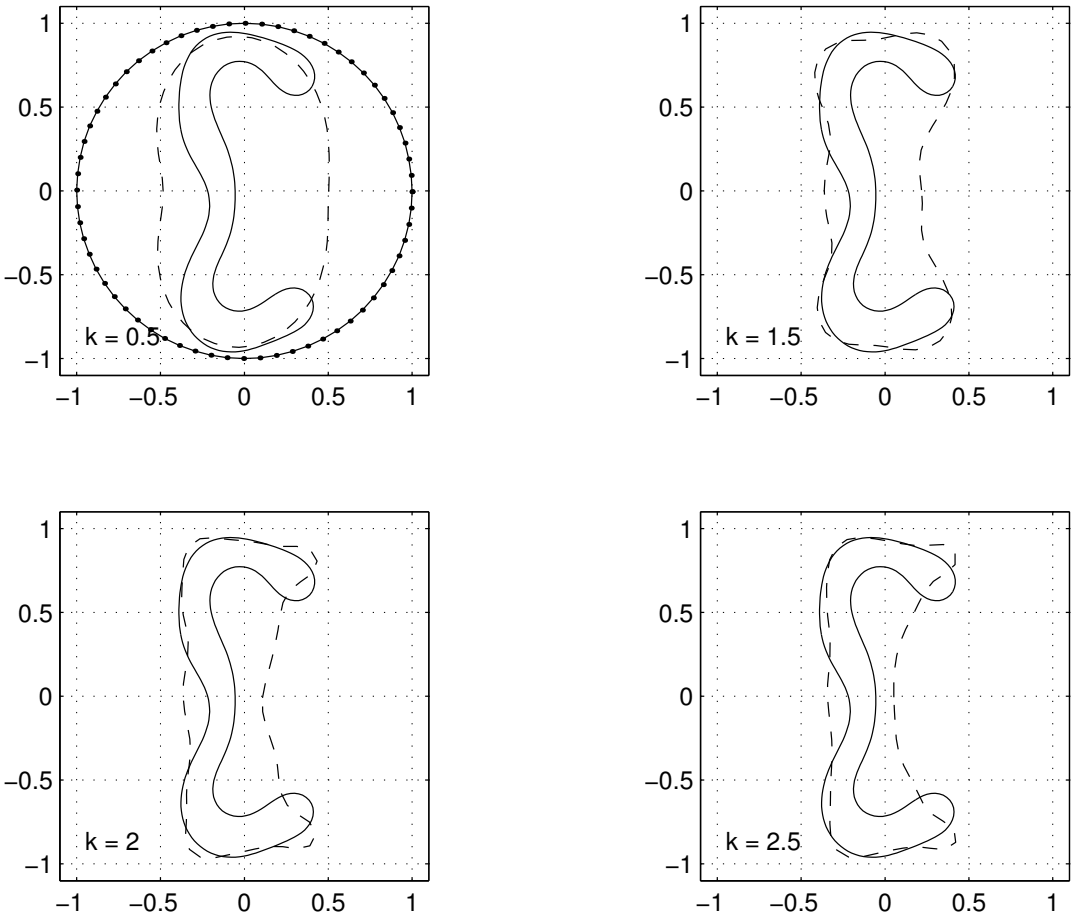

Figure 4.61: When the semi-wavelength is about the same size of the outer opening the approximated boundary curve starts approaching the cavity inner part.

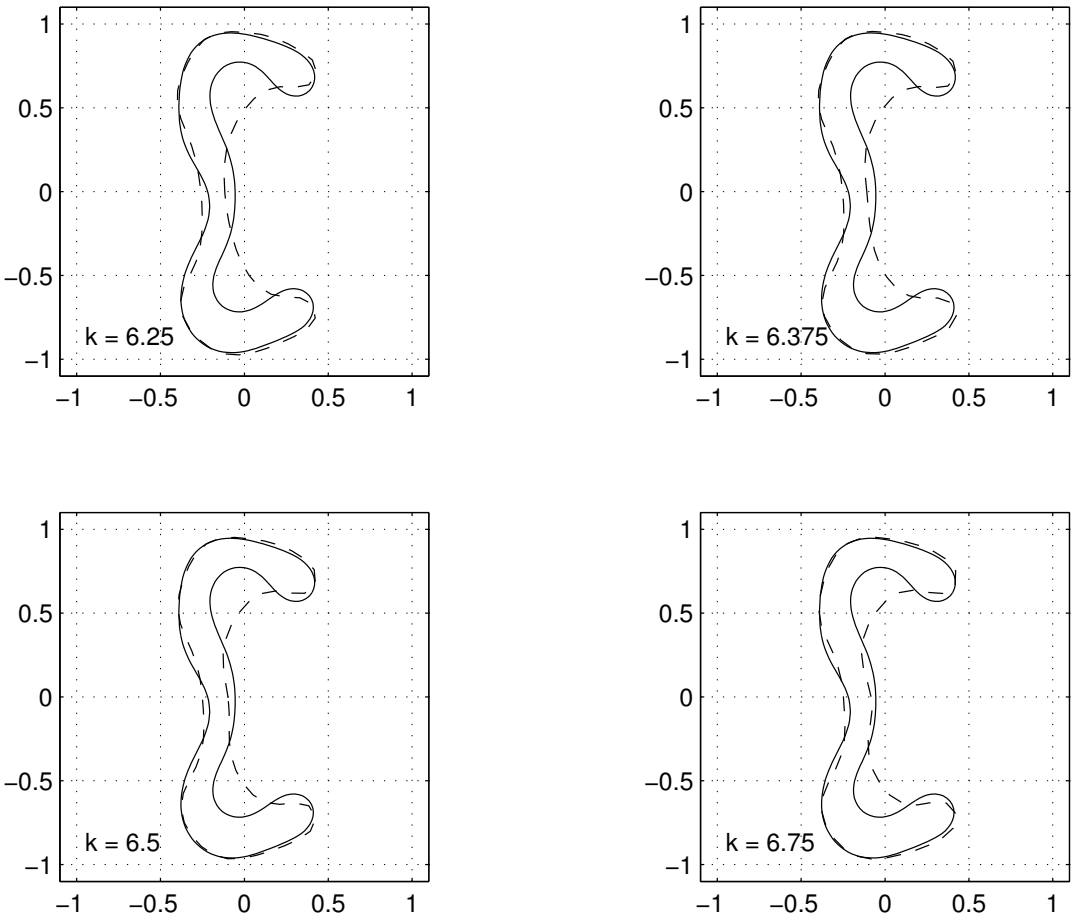

Figure 4.62: The fine details of the inner side of the boundary curve are reconstructed when the wavelength is smaller than the cavity opening.

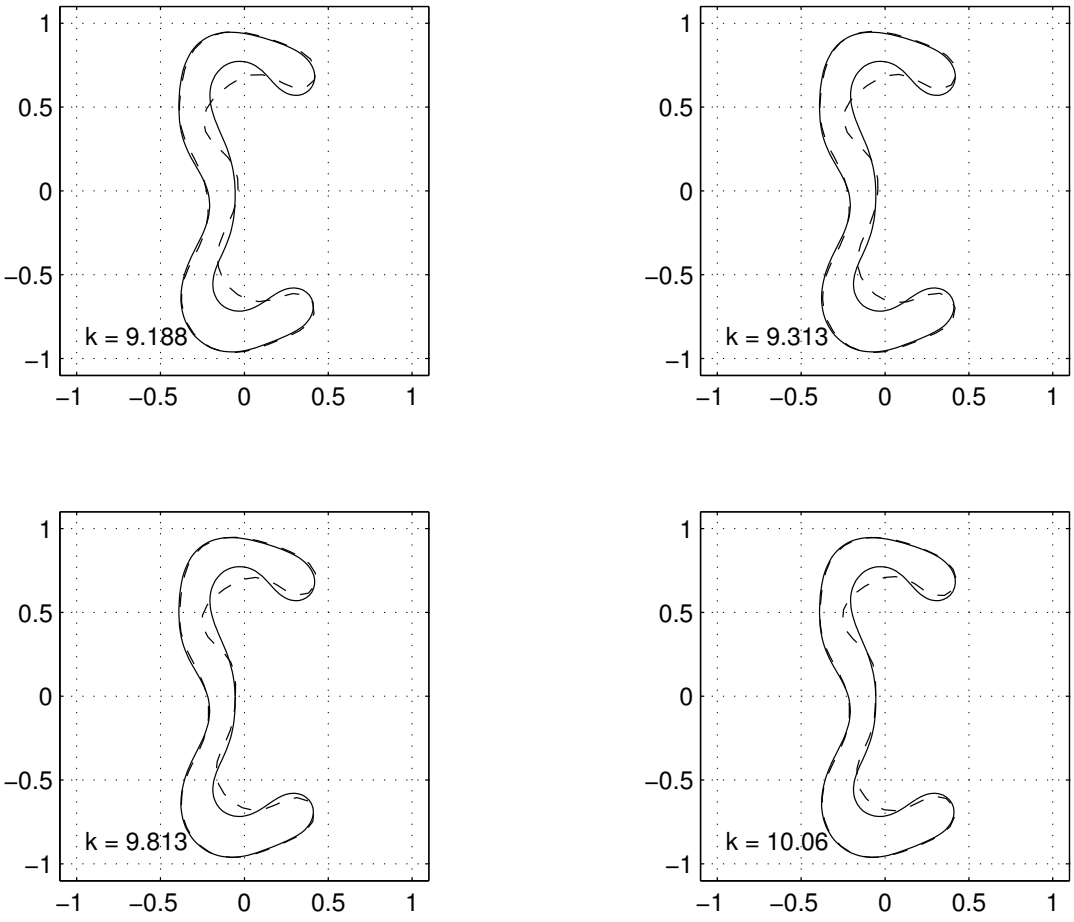

Figure 4.63: When the reconstruction of the boundary curve is close to being complete the relative change between consecutive approximated curves is tiny.

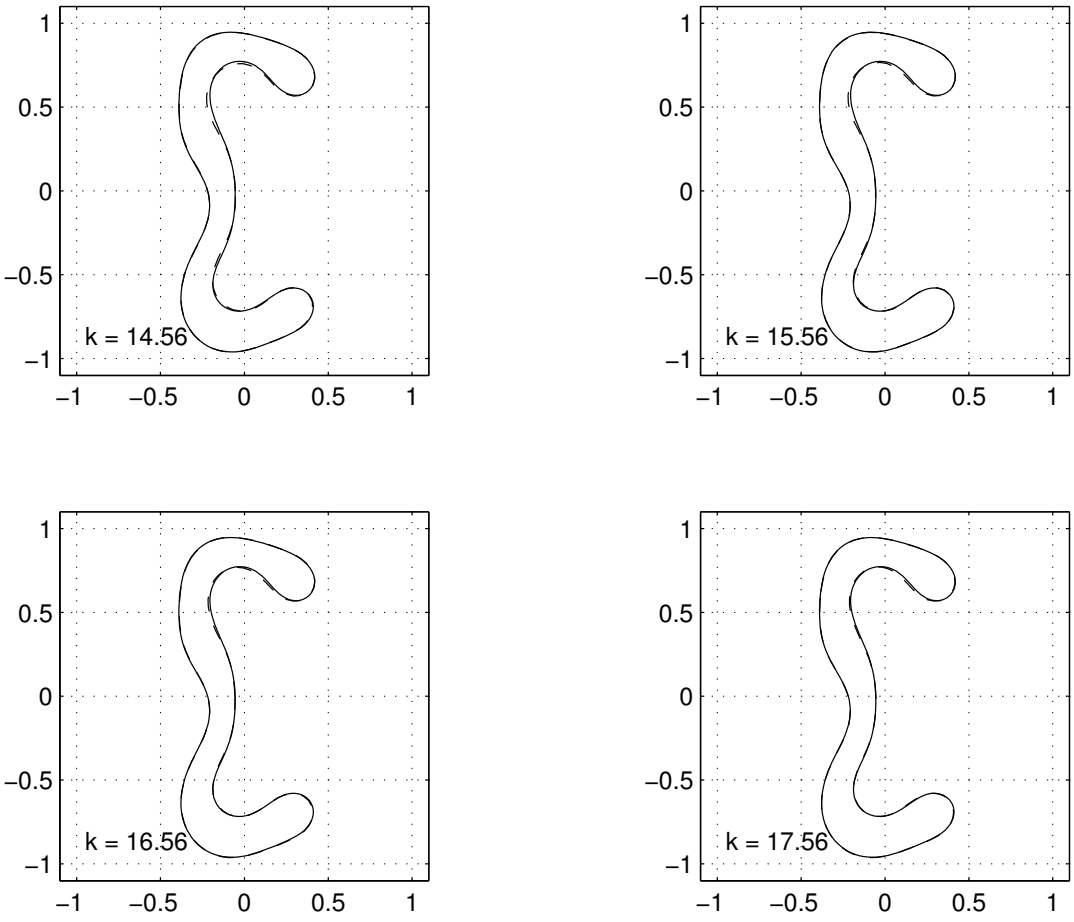

Figure 4.64: The ϵ shaped domain is also reconstructed within two significant digits.

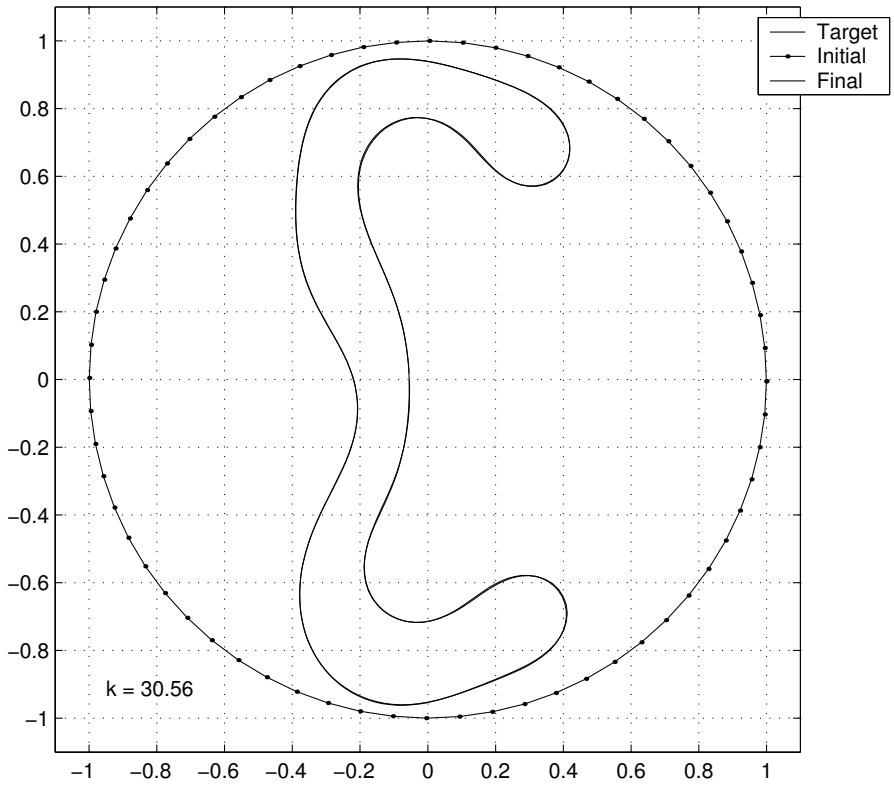

Figure 4.65: The relative residual does not decrease below 10^{-3} in the chosen wavenumber interval. But the ϵ shaped obstacle is reconstructed within two significant digits.

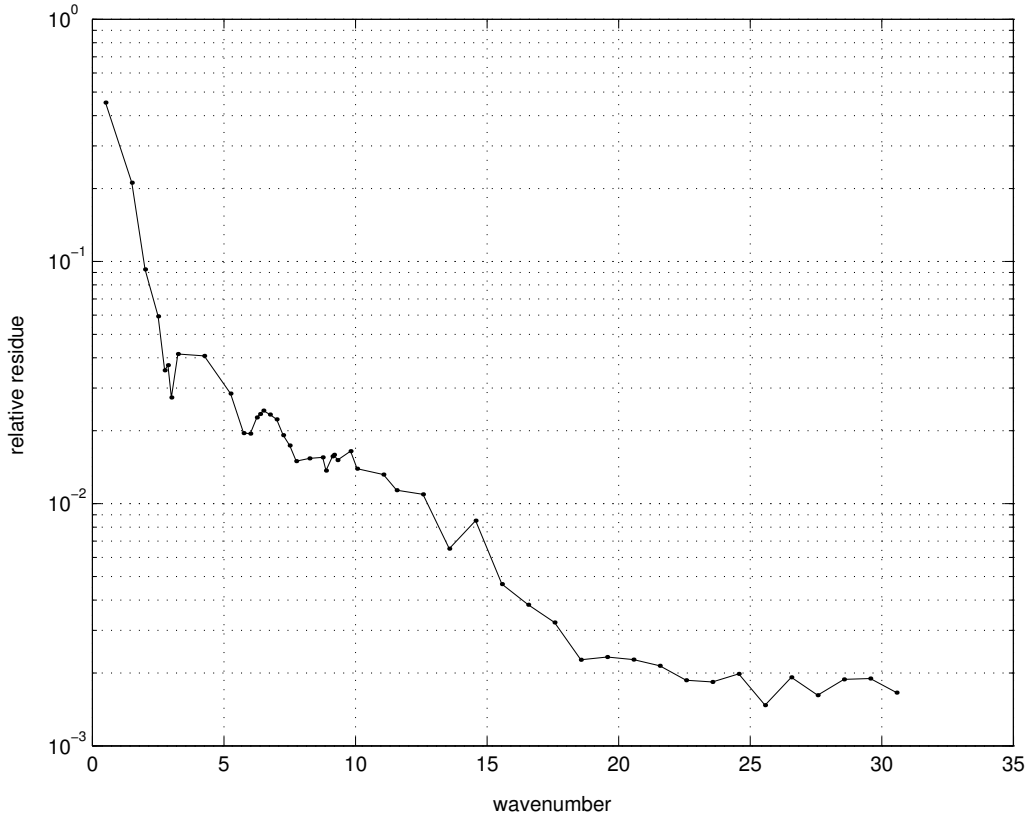

Chapter 5

Future Work

It is apparent that further research is needed on the method of continuation introduced in this work. It is necessary to establish theoretical results on the convergence of the method, as well as to develop other regularization schemes in order to extend the continuation method to other closely related problems. There are several extensions or variants of the solution of the problem that we regard as important to investigate:

To adapt the continuation method to inverse obstacle scattering problem with Neumann boundary condition and the inverse impedance problem. The integral equation representation of radiating solutions to the Helmholtz equations is key for the representation of the far field mapping in the present work. In the integral equation formulation of the direct obstacle scattering problems with Neumann condition and the inverse impedance problem stronger singularities are obtained in the kernels of the integral operators. It is necessary to implement appropriate quadratures for its numerical treatment.

To adapt the method of continuation to the inverse transmission problem. Another natural question to ask is whether the continuation method can be extended to the inverse transmission problem. The question of practicality in terms of computational cost should be addressed.

Reconstruction of multiple obstacles. The further development of numerical tools to generate and process arbitrary simple closed curves is necessary for the systematic study of the inverse obstacle scattering problem, with an emphasis on the problem of the reconstruction of multiple obstacles.

Appendix

Combined Potential Representation of the Far Field Pattern and the Domain Derivative of the Far Field Mapping

Let us define for convenience three operators for $x \in \Gamma$

$$K_\tau(\varphi)(x) = 2\int_\Gamma \frac{\partial G(x,y)}{\partial \tau(y)}\varphi(y)ds(y), \tag{A.1}$$

$$T(\varphi)(x) = 2\lim_{h\to+0}\int_\Gamma \frac{\partial^2 G(x+h\nu(x),y)}{\partial \nu(x)\partial\nu(y)}\varphi(y)ds(y), \tag{A.2}$$

$$T'(\varphi)(x) = 2\lim_{h\to+0}\int_\Gamma \frac{\partial^2 G(x+h\nu(x),y)}{\partial^2 \nu(y)}\varphi(y)ds(y). \tag{A.3}$$

K_τ is bounded from $C(\Gamma)$ to $C(\Gamma)$, whereas T, T' are bounded from $C^1(\Gamma)$ to $C(\Gamma)$. For real $\mu \neq 0$, let $H : C(\Gamma) \to C(\Gamma)$ be defined by the formula

$$H(\varphi)(x) = 2\int_\Gamma \Psi(x,y)\varphi(y)ds(y), \tag{A.4}$$

where

$$\Psi(x,y) = \frac{\partial G(x,y)}{\partial \nu(y)} - ik\mu G(x,y), \tag{A.5}$$

and $G(x,y)$ is the fundamental solution of the Helmholtz equation. Let $u^s(x) = \int_\Gamma \Psi(x,y)\varphi(y)ds(y)$ for $\varphi(y) \in C(\Gamma)$ and $x \notin \Gamma$, then $u^s(x)$ is solution of the direct scattering problem with incident field $u^i(x)$ if and only if φ is solution of the integral equation of the second kind

$$(I - H)(\varphi)(x) = -2u^i(x), \quad x \in \Gamma, \tag{A.6}$$

or

$$\lim_{h \to +0} \int_\Gamma \Psi(x + h\nu(x), y)\varphi(y)ds(y) = -u^i. \tag{A.7}$$

The following well known result is required to represent the far field pattern in terms of the combined potential.

Lemma A.0.1 *For $y \in \Gamma$ and $x \in \mathbb{R}^2 - D$ such that $\|x\| \gg \|y\|$, it follows that*

$$G(x,y) = \frac{i}{4}\sqrt{\frac{2}{k\pi\|x\|}}e^{i(k\|x\| - \pi/4) - ik\hat{x}\cdot y}\left[1 + O(\frac{1}{\|x\|})\right], \tag{A.8}$$

$$\frac{\partial G(x,y)}{\partial \nu(y)} = \frac{i}{4}\sqrt{\frac{2}{k\pi\|x\|}}e^{i(k\|x\| - \pi/4) - ik\hat{x}\cdot y}(-i)\hat{x}\cdot\nu(y)\left[1 + O(\frac{1}{\|x\|})\right]. \tag{A.9}$$

The far field pattern can be expressed in terms of the combined potential by

$$u_\infty(\hat{x}) = \int_\Gamma \Psi_\infty(\hat{x}, y)\varphi(y)ds(y), \tag{A.10}$$

with kernel $\Psi_\infty : \Omega \times \Gamma \to \mathbb{C}$ given by

$$\Psi(\hat{x}, y) = \frac{k}{4}e^{-ikx\cdot y}[\hat{x}\cdot\nu(y) + \mu]. \tag{A.11}$$

Using the notation introduced in lemma 3.2.1 let us assume that at each point $x(s)$ the boundary is perturbed along the normal direction to the point $\tilde{x} = \eta(x)$ on the perturbed curve $\tilde{\Gamma}$. We further assume that the perturbation is small so that conditions from equation 3.9 are satisfied. Let us denote by $\tilde{\varphi}$ the solution of the integral equation on $\tilde{\Gamma}$

$$\lim_{h \to +0} \int_{\tilde{\Gamma}} \Psi(\tilde{x} + h\nu(\tilde{x}), \tilde{y}) \tilde{\varphi}(\tilde{y}) d\tilde{s}(\tilde{y}) = -u^i(\tilde{x}). \tag{A.12}$$

Lemma A.0.2 *Suppose under the conditions of lemma 3.2.2 that for* $x \in \Gamma$

$$\delta(x) = \max\{ \mid \kappa(x)\delta\nu(x) \mid, \mid \frac{d(\delta\nu)}{ds}(x) \mid \} \tag{A.13}$$

then

$$\delta\varphi(x) = \tilde{\varphi}(\tilde{x}) - \varphi(x) \tag{A.14}$$

is of the order $\delta(x)$. *Furthermore, to the second order of* $\delta(x)$, $\delta\varphi(x)$ *satisfies the equation*

$$\begin{aligned}(I - H)(\delta\varphi)(x) = &-(I - H)(\kappa\delta\nu\varphi)(x) - K_\tau(\varphi\frac{d(\delta\nu)}{ds})(x) \\ &+ (T' - ik\mu K)(\delta\nu\varphi)(x) + [(T - ik\mu K')(\varphi)(x) - 2\frac{\partial u^i}{\partial \nu}(x)]\delta\nu(x).\end{aligned} \tag{A.15}$$

Proof

For points x,$y \in \Gamma$ lets denote by $\tilde{x} = \eta(x)$ and $\tilde{y} = \eta(y)$ the corresponding points on $\tilde{\Gamma}$ it follows from 3.9 that A.7 that can be rewritten as

$$\lim_{h \to +0} \int_{\Gamma} \Psi(\eta(x), \eta(y)) \tilde{\varphi}(\eta(y))(1 + \kappa(y)\delta\nu(y)) ds(y) = -u^i(\eta(x)) \tag{A.16}$$

to the second order of $\delta(x)$. Substracting A.7 from A.12, we obtain

$$V(x) = -\frac{\partial u^i}{\partial \nu}(x), \tag{A.17}$$

again to the second order of $\delta(x)$, where

$$V(x) = \lim_{h\to+0}\left\{\int_\Gamma \Psi(x+h\nu(x),y)[\delta\varphi(y)+\kappa(y)\varphi(y)\delta\nu(y)]ds(y) + \int_\Gamma [\Psi(\eta(x)+h\nu(\eta(x)),\eta(y)) - \Psi(x+h\nu(x),y)]\varphi(y)ds(y)\right\}. \quad (A.18)$$

The second integral in A.18 can be split into three parts

$$\int_\Gamma [\Psi(\eta(x)+h\nu(\eta(x)),\eta(y)) - \Psi(x+h\nu(x),y)]\varphi(y)ds(y) = I_1+I_2+I_3, \quad (A.19)$$

where

$$\begin{aligned} I_1 &= \int_\Gamma [\Psi(\eta(x)+h\nu(\eta(x)),\eta(y)) - \Psi(\eta(x)+h\nu(x),\eta(y))]\varphi(y)ds(y), \\ I_2 &= \int_\Gamma [\Psi(\eta(x)+h\nu(x),\eta(y)) - \Psi(\eta(x)+h\nu(x),y)]\varphi(y)ds(y), \\ I_3 &= \int_\Gamma [\Psi(\eta(x)+h\nu(x),y) - \Psi(x+h\nu(x),y)]\varphi(y)ds(y). \end{aligned}$$

It follows from the jump conditions of the acoustic potentials at the boundary Γ that, to the second order of $\delta(x)$

$$I_1 = -K_\tau(\varphi\frac{d(\delta\nu)}{ds})(x), \quad (A.20)$$

$$I_2 = [T' - ik\mu(K-I)](\varphi\delta\nu)(x), \quad (A.21)$$

$$I_3 = [T - ik\mu(K'+I)](\varphi)(x)\delta\nu(x). \quad (A.22)$$

The lemma follows immediately. ■

The integral equation A.15 specifies the linear relation

$$(I-H)(\delta\varphi)(x) = W(\delta\nu) \quad (A.23)$$

between the perturbational variables $\delta\nu$ and $\delta\varphi$ where $W : C^1(\Gamma) \to C(\Gamma)$ is the linear operator defined by the right hand side of A.18. Since H is compact $I-H$ has a bounded inverse, thus A.23 can be solved to yield an expression for

$\delta\varphi$ in terms of $\delta\nu$ for given Γ and φ. The same perturbational analysis can be applied to the far field pattern with the combined potential representation. Let $\tilde{u}_\infty$ be the far field pattern generated by the density function $\tilde{\varphi}$ on $\tilde{\Gamma}$ so that

$$\tilde{u}_\infty(\hat{x}) = \int_{\tilde{\Gamma}} \Psi_\infty(\hat{x}, \tilde{y})\tilde{\varphi}(\tilde{y})d\tilde{s}(\tilde{y}). \tag{A.24}$$

Lemma A.0.3 *Under the conditions of lemma 3.2.2 suppose that the density functions $\varphi \in C(\Gamma)$ and $\tilde{\varphi} \in C(\tilde{\Gamma})$ are the solutions of the integral equations A.7 and A.12 respectively. Suppose further that u_∞, $\tilde{u}_\infty \in C(\Omega)$ are defined by A.10, A.24 are the far field patterns corresponding respectively to the densities φ, $\tilde{\varphi}$. Then*

$$\delta u_\infty(\hat{x}) = \tilde{u}_\infty(\hat{x}) - u_\infty(\hat{x}) \tag{A.25}$$

is of the order of $\delta(x)$, and to the second order of $\delta(x)$

$$\delta u_\infty(\hat{x}) = H_\infty(\delta\varphi + \kappa\varphi\delta\nu) + M_\infty(\delta\nu) \tag{A.26}$$

where the operators $H_\infty : C(\Gamma) \to C(\Gamma)$ and $M_\infty : C^1(\Gamma) \to C(\Omega)$ are defined by the formulae

$$\begin{aligned} H_\infty(w)(\hat{x}) &= \int_{infty} \Psi(\hat{x}, y)w(y)ds(y), \\ M_\infty(w)(\hat{x}) &= \frac{k}{4}\int_\infty [ik\hat{x}\cdot\nu(y)[\hat{x}\cdot\nu(y) + \mu]w(y) + \hat{x}\cdot\tau(y)\frac{dw}{ds}(y)]e^{-ik\hat{x}\cdot y}\varphi(y)ds(y). \end{aligned}$$

Proof

Denote by $\tilde{y} = \eta(y)$ the point on $\tilde{\Gamma}$ corresponding to $y \in \Gamma$. Subtracting A.10 from A.24 and combining the result with 3.9 we get

$$\begin{aligned} \delta u_\infty(\hat{x}) &= \int_\Gamma \Psi(\hat{x}, \eta(y))(1 + \kappa(y)\delta\nu(y))(\varphi(y) + \delta\varphi(y))ds(y) - \\ &\quad \int_\Gamma \Psi(\hat{x}, y)\varphi(y)ds(y) + O(\|\delta\nu\|_\infty^2). \end{aligned} \tag{A.27}$$

By straightforward differentiation with respect to s we obtain that to the second order of $\delta(x)$

$$\int_{\Gamma}[\Psi_{\infty}(\hat{x},\eta(y)) - \Psi(\hat{x},y)]\varphi(y)ds(y) = M_{\infty}(\delta\nu). \tag{A.28}$$

■

The substitution of A.15 into A.26 yields

$$\delta u_{\infty}(\hat{x}) = H_{\infty}((I-H)^{-1}W(\delta\nu) + \kappa\varphi\delta\nu) + M_{\infty}. \tag{A.29}$$

Bibliography

[1] M. Brandfass, A. D. Lanterman, and K. F. Warnick. A comparison of the colton-kirsch inverse scattering methods with linearized tomographic inverse scattering. *Inverse Problems*, 17:1797–1816, 2001.

[2] M. Burguer. A level set method for inverse problems. *Inverse Problems*, 17:1327–1355, 2001.

[3] F. Cakoni and D. Colton. On the mathematical basis of the linear sampling method. *(submitted)*, 2002.

[4] F. Cakoni, D. Colton, and P. Monk. The direct and inverse scattering problems for partially coated obstacles. *Inverse Problems*, 17:1997–2015, 2001.

[5] D. Colton. The inverse scattering problem for time-harmonic acoustic waves. *SIAM Review*, 26(3):323–350, July 1984.

[6] D. Colton, H. W. Engl, A. K. Louis, J. R. McLaughlin, and W. Rundell. *Surveys on Solution Methods for Inverse Problems*. Springer-Verlag, Wien, 2000.

[7] D. Colton and A. Kirsch. A simple method for solving inverse scattering problems in the resonance region. *Inverse Problems*, 12:383–393, 1996.

[8] D. Colton and R. Kress. *Integral Equation Methods in Scattering Theory.* Wiley-Interscience Publications, New York, 1983.

[9] D. Colton and R. Kress. *Inverse Acoustic and Electromagnetic Scattering Theory.* Springer-Verlag, New York, second edition, 1998.

[10] D. Colton and P. Monk. A novel method for solving the inverse scattering problem for time-harmonic acoustic waves in the resonance region. *SIAM Journal of Applied Mathematics*, 45(6):1039–1053, Dec 1985.

[11] D. Colton and P. Monk. A novel method for solving the inverse scattering problem for time-harmonic acoustic waves in the resonance region ii. *SIAM Journal of Applied Mathematics*, 46(3):506–523, Jun 1986.

[12] D. Colton and P. Monk. The numerical solution of the three dimensional inverse scattering problem for time-harmonic acoustic waves. *SIAM J. Sci. Stat. Comp.*, 8:278–291, 1987.

[13] M. Hanke, F. Hettlich, and O. Scherzer. *The Landweber Iteration for an Inverse Scattering Problem.* Proceedings of the 1995 Design Engineering Technical Conferences, Vol. 3, Part C (Wang et al), eds. The American Society of Mechanical Engineers, New York, 1995.

[14] F. Hettlich. *An Iterative Method for the Inverse Scattering Problem from Sound-hard Obstacles.* Proceedings of the ICIAM 95, VOL. II, Applied Analysis (Mahrenholz and Mennicken, eds). Academie Verlag, Berlin, 1996.

[15] F. Hettlich. The landweber iteration applied to inverse conductive scattering problems. *Inverse Problems*, 14:931–947, 1998.

[16] T. Hohage. Logarithmic convergence rates of the iteratively regularized gauss-newton method for an inverse potential and an inverse scattering problem. *Inverse Problems*, 13:1279–1299, 1997.

[17] T. Hohage. Convergence rates of a regularized newton method in sound-hard inverse scattering. *SIAM J. Numer. Anal.*, 36(1):125–142, 1998.

[18] J. Ize. *Cálculo de Variaciones.* Centro de Investigación y de Estudios avanzados, IPN, México D.F., 1987.

[19] Q. N. Jin. The analysis of a discrete scheme of the iteratively regularized gauss-newton method. *Inverse Problems*, 16:1457–1476, 2000.

[20] A. Kirsch. The domain derivative and two applications in inverse scattering. *Inverse Problems*, 9:81–96, 1993.

[21] A. Kirsch. Numerical algorithms in inverse scattering theory. *Ordinary and Partial Differential Equations, Vol. IV*, 289:81–96, 1993.

[22] A. Kirsch. *An Introduction to the Mathematical Theory of Inverse Problems.* Springer-Verlag, New York, 1996.

[23] A. Kirsch and R. Kress. On an integral equation of the first kind in inverse acoustic scattering. *Inverse Problems(Cannon and Hornung, eds). ISNM*, 77:93–102, 1986.

[24] A. Kirsch and R. Kress. A numerical method for an inverse scattering problem. *Inverse Problems*, pages 279–290, 1987.

[25] A. Kirsch and R. Kress. An optimization method method in inverse acoustic scattering. *Boundary Elements IX, Vol 3. Fluid Flow and Potential Applications*, pages 3–18, 1987.

[26] A. Kirsch and S. Ritter. A linear sampling method for inverse scattering from an open arc. *Inverse Problems*, 16:89–105, 2000.

[27] R. Kress. *Linear Integral Equations*. Springer-Verlag, Berlin Heildelberg New York, 1989.

[28] R. Kress. A newton method in inverse obstacle scattering. *Inverse Problems in Engineering Mechanics*, pages 425–432, 1994.

[29] R. Kress. Integral equation methods in inverse obstacle scattering. *Engineering Anal. with Boundary Elements*, 15:171–179, 1995.

[30] R. Kress. Integral equation methods in inverse acoustic and electromagnetic scattering. *Boundary Integral Formulations for Inverse Analysis*, pages 67–92, 1997.

[31] R. Kress and W. Rundell. A quasi-newton method in inverse scattering. *Inverse Problems*, 10:1145–1157, 1994.

[32] R. Kress and W. Rundell. Inverse scattering for shape and impedance. *Inverse Problems*, 17:1075–1085, 2001.

[33] A. Litman, D. Lesselier, and F. Santosa. Reconstruction of a two-dimensional binary obstacle by controlled evolution of a level-set. *Inverse Problems*, 14:685–706, 1998.

[34] L. Mönch. A newton method for solving the inverse scattering problem for a sound-hard obstacle. *Inverse Problems*, 12:309–323, 1996.

[35] L. Mönch. On the inverse acoustic scattering problem by an open arc: the sound-hard case. *Inverse Problems*, 13:1379–1392, 1997.

[36] R. D. Murch, D. G. H. Tan, and D. J. N. Wall. Newton-kantorovich method applied to two-dimensional inverse scattering for an exterior helmholtz problem. *Inverse Problems*, 4:1117–1128, 1988.

[37] B. Noble and J. Daniel. *Algebra Lineal Aplicada.* Prentice-Hall hispanoamericana, Naucalpan de Juárez, 1989.

[38] R. Potthast. On the convergence of a new newton-type method in inverse scattering. *Inverse Problems*, 17:1419–1434, 2001.

[39] A. Roger. Newton-kantorovich algorithm applied to an electromagnetic inverse problem. *IEEE Trans. Ant. Prop.*, AP-29:232–238, 1981.

[40] F. Santosa. A level-set approach approach for inverse problems involving obstacles. *Control, Optimization and Calculus of Variations*, 1:17–33, Jan. 1996.

[41] G. Strang. *Linear Algebra and its Applications.* Harcourt Brace Jovanovich College Publishers, Orlando, third edition, 1988.

[42] A. Tacchino, J. Coyle, and M. Piana. Numerical validation of the linear sampling method. *Inverse Problems*, 18:511–527, 2002.

[43] W. Tobocman. Inverse acoustic wave scatterring in two dimensions from impenetrable targets. *Inverse Problems*, 5:1131–1144, 1989.

[44] S. L. Wang and Y. M. Chen. An efficient numerical method for exterior and interior inverse problems of helmholtz equation. *Wave Motion*, 13:387–399, 1991.